Dipl. –Ing. Taher Abu Ali, BSc

# Fabrication of Multi-Stimuli Responsive Nanorods for Electronic Skin Applications

**DOCTORAL THESIS**

to achieve the university degree of

Doktor der technischen Wissenschaften

submitted to

**Graz University of Technology**

**Supervisor**

Assoc.Prof. Dr. Anna Maria Coclite

Institute of Solid State Physics

Graz, October 2022

## AFFIDAVIT

I declare that I have authored this thesis independently, that I have not used other than the declared sources/resources, and that I have explicitly indicated all material which has been quoted either literally or by content from the sources used. The text document uploaded to TUGRAZonline is identical to the present doctoral thesis.

Date, Signature

## Abstract

The PhD thesis deals with fabrication and characterization of sensors for force, humidity and temperature that can be used for electronic skin (e-skin) concepts. The investigation started with the characterization of piezoelectric zinc oxide (ZnO) thin films. The films were deposited on rigid glass as well as flexible PET substrates, at different substrate temperatures, using plasma-enhanced atomic layer deposition (PEALD). The technique offers sub-nanometer thickness control, due to its self-limiting growth per cycle feature. Additionally, the technique provides highly dense films with excellent electrical properties, specifically, piezoelectricity. We demonstrated that the piezoelectric properties could be tuned by a choice of deposition parameters. Of particular importance is the substrate temperature during deposition. This parameter defines the preferential crystallographic orientation of the grown ZnO and there for, defines the piezoelectric polarization orientation. XRD and PFM investigations revealed polycrystalline films with strong (002) orientation with increasing substrate temperature. The ZnO thin films were combined with a hydrogel in core-shell nanorods, with the hydrogel material of choice being poly(N-vinylcaprolactam) or p(NVCL), which a biocompatible thermoresponsive polymer. Upon exposure to water molecules, the hydrogel swells by incorporating them into its structure. The swelling behavior is dependent on the concentration of water molecules (humidity) and temperature. The hydrogel core was deposited using initiated chemical vapor deposition (iCVD), which is a radical polymerization technique, involving film growth from volatile vapor-phase monomers. Similar to PEALD, iCVD permits fine-tuning of several parameters during growth, which results in different swelling properties. Co-polymerization or cross-linking of the hydrogel resulted in a stable film, where no dissolution or delamination was observed. Furthermore, an e-skin was demonstrated by sandwiching an array of the ZnO-hydrogel core-shell nanorods between two electrodes. The e-skin was able to directly sense force and pressure changes through the piezoelectric shell, while sensitivity to humidity and temperature was attributed to the swelling of the hydrogel core, which applied a mechanical stress on the piezoelectric shell resulting in an electrical output signal. Additionally, thorough characterization of the multi-stimuli responsive behavior was conducted in combination with other electrical characterization techniques. Finally, the e-skin performance and design was compared to FEM simulations for optimization.

# Kurzfassung

Die Dissertation befasst sich mit der Herstellung und Charakterisierung von Sensoren für Kraft, Feuchtigkeit und Temperatur, die für elektronische Hautkonzepte (E-skin) verwendet werden können. Die Untersuchung begann mit der Charakterisierung von piezoelektrischen Zinkoxid (ZnO)-Dünnschichten. Die Schichten wurden mit Hilfe der plasmagestützten Atomlagenabscheidung (PEALD) auf starren Glas- und flexiblen PET-Substraten bei unterschiedlichen Substrattemperaturen abgeschieden. Das Verfahren ermöglicht eine Kontrolle der Schichtdicke im Subnanometerbereich, da das Wachstum pro Zyklus selbstlimitierend ist. Darüber hinaus liefert das Verfahren hochdichte Schichten mit hervorragenden elektrischen Eigenschaften, insbesondere Piezoelektrizität. Wir haben gezeigt, dass die piezoelektrischen Eigenschaften durch die Wahl der Abscheidungsparameter eingestellt werden können. Von besonderer Bedeutung ist die Substrattemperatur während der Abscheidung. Dieser Parameter bestimmt die bevorzugte kristallografische Ausrichtung des gewachsenen ZnO und damit auch die Ausrichtung der piezoelektrischen Polarisation. XRD- und PFM-Untersuchungen ergaben polykristalline Schichten mit starker (002)-Orientierung bei steigender Substrattemperatur. Die ZnO-Dünnschichten wurden mit einem Hydrogel in Kern-Schale-Nanostäbchen kombiniert, wobei als Hydrogelmaterial Poly(N-vinylcaprolactam) oder p(NVCL), ein biokompatibles, thermoresponsives Polymer, gewählt wurde. Bei Kontakt mit Wassermolekülen quillt das Hydrogel auf, indem es diese in seine Struktur einbaut. Das Quellverhalten ist abhängig von der Konzentration der Wassermoleküle (Feuchtigkeit) und der Temperatur. Der Hydrogelkern wurde mit Hilfe der initiierten chemischen Gasphasenabscheidung (iCVD) abgeschieden, einer radikalischen Polymerisationstechnik, bei der der Film aus flüchtigen Monomeren in der Gasphase entsteht. Ähnlich wie PEALD ermöglicht iCVD eine Feinabstimmung verschiedener Parameter während des Wachstums, die zu unterschiedlichen Quelleigenschaften führen. Die Co-Polymerisation oder Vernetzung des Hydrogels führte zu einem stabilen Film, bei dem keine Auflösung oder Delamination zu erwarten war. Darüber hinaus wurde eine E-Skin demonstriert, indem eine Anordnung von ZnO-Hydrogel-Kern-Schale-Nanostäbchen zwischen zwei Elektroden eingefügt wurde. Die E-Skin war in der Lage, Kraft- und Druckänderungen direkt über die piezoelektrische Schale zu erfassen, während die Empfindlichkeit gegenüber Feuchtigkeit und Temperatur auf das Aufquellen des Hydrogelkerns zurückgeführt wurde, der eine mechanische Spannung auf die piezoelektrische Schale ausübte, was zu einem elektrischen Ausgangssignal führte. Darüber hinaus wurde eine gründliche Charakterisierung des auf mehrere Reize reagierenden Verhaltens in Kombination mit anderen elektrischen Charakterisierungstechniken durchgeführt. Schließlich wurden die Leistung und das Design der E-Skin mit FEM-Simulationen zur Optimierung verglichen.

# Acknowledgements

First, I would like to express my sincere thanks to Anna Maria Coclite, my supervisor at Graz University of Technology, as well as Barbara Stadlober, my supervisor at Joanneum Research-Materials, for their support in all aspects of this PhD thesis, including guidance and transfer of knowledge.

I am also thankful to my colleagues from Graz University of Technology, Fabian Muralter, Julian Pilz, Marianne Kräuter, Katrin Unger, Richard Berger and Lisanne Demelius for their scientific and experimental support as well as their company during office hours. Additionally, special thanks go to Philipp Schäffner, Gerburg Schider, Maria Belegratis, as well as other colleagues from my HEP group at Joanneum Research, for their continuous support.

I would like to express my deepest emotions of gratitude to my parents, who helped me achieve my full scientific potential through their support. Since the day I was born, they provided me with countless blessings and prepared me in every important aspect to reach where I am today. To that, I would like to acknowledge my siblings for their emotional support.

Most importantly, I would like to extend my deepest emotions of gratitude to my amazing wife Sara, who shared and still shares every small aspect of this life with me. She gave me the motivation and the will to give my best during the work that lead to this thesis. Finally yet importantly, I would like to dedicate this thesis to my beautiful little baby girl Eva, who was born during its course.

# Table of Content

## Acronyms

| | |
|---|---|
| e-skin | electronic skin |
| NVCL | N-vinylcaprolactam |
| DEGDVE | di(ethylene glycol) divinyl ether |
| iCVD/MOCVD | initiated/metal organic chemical vapor deposition |
| T-ALD/PEALD | thermal/plasma enhanced atomic layer deposition |
| T-NIL/UV-NIL | thermal/ultraviolet nanoimprint lithography |
| FEM/FEA | finite element method/analysis |
| NP | nanoparticles |
| NW | nanowires |
| CNT | carbon nanotubes |
| CB | carbon black |
| PDMS | polydimethylsiloxane |
| PU | polyurethane |
| PVA | polyvinyl acetate |
| PCL | polycaprolactone |
| PLA | polylactic acid |
| PEDOT:PSS | poly(3,4-ethylenedioxythiophene) polystyrene sulfonate |
| PVDF | polyvinylidene difluoride |
| TrFE | tetrafluoroethylene |
| PET | polyethylene terephthalate |
| TENG | triboelectric nanogenerator |
| PTFE | polytetrafluoroethylene |
| AR | aspect ratio |
| Go/rGo | graphene oxide/reduced graphene oxide |
| LCST/UCST | lower/upper critical solution temperature |

| | |
|---|---|
| NIPAAM | N-isopropylacrylamide |
| PLD | pulsed laser depositon |
| DEZ/DMZ | diethylzinc/dimethylzinc |
| GPC | growth per cycle |
| RH | relative humidity |
| GF | gauge factor |
| XRD | x-ray diffraction |
| AFM/PFM | atomic/piezo force microscopy |
| SEM | scanning electron microscopy |
| RVE | representative volume element |
| GEIS | galvanostatic electrochemical impedance spectroscopy |
| ERC | European research council |

# 1
# Introduction

This chapter provides an introductory overview on the topics covered in this thesis. It presents the electronic skin concept as well as an outline for the chapters to come.

## 1.1 Motivation and outline

The skin is the largest organ in humans and it plays a crucial role as the physical interface between the body and the surrounding.[1] Due to its wide sensing range of stimuli, it is composed of complex multisensory systems. Mimicking the behavior and the functionality of the human skin has become a necessity in the fields of robotics, prosthetics and other medical applications and for that reason has been a widely explored challenge in the past 20 years. An efficient electronic skin (e-skin) is sensitive to different modes of mechanical excitation, which include force/pressure, strain and shear force. Additionally, the e-skin must be sensitive to surrounding changes in humidity and temperature. In combination with the desired multi-stimuli responsiveness, the e-skin is required to be flexible and stretchable, as both qualities improve the performance, lifetime as well as the stability.[2-4] However, harsh operating conditions can still lead to damage coupled with deterioration in the performance, there for, an e-skin with self-healing capabilities help address this issue. Finally yet importantly, our growing awareness of the environmental issues that we collectively face, possesses a necessity to explore biocompatible materials fabricated using energy-efficient techniques, as well as the biodegradability of these materials after prolonged use of the e-skin.[5,6]

In this thesis, a new innovative e-skin concept is proposed, as shown in **Figure 1**. The proposed e-skin can detect surrounding changes in force/pressure, humidity and temperature through the combination of two active materials in core-shell nanorod structures embedded in a structured soft polymeric template. Chapter 2 starts by introducing the basic concepts of an e-skin, with focus on the required properties and sensitivities. Section 2.2 introduces the concept of hydrogels, their classes, properties and iCVD as a fabrication technique for such materials. Section 2.3 introduces zinc oxide with a focus on its piezoelectric properties and its nanofabrication using PEALD. Additionally, UV-NIL as well as COMSOL Multiphysics are presented in sections 2.4 and 2.5 respectively. In chapter 3, three peer-reviewed publications are presented. Section 3.1 presents the piezoelectric properties of ZnO thin films prepared by PEALD. Followed by section 3.2, where the e-skin concept is presented and explored. Section 3.3 shows an optimization of the e-skin. The appendices provide additional insight by presenting device optimization with respect to nanorod aspect ratio and pitch using finite element method (FEM) simulations, in addition to initial stability tests. Finally, a list of scientific publications and presentations is listed.

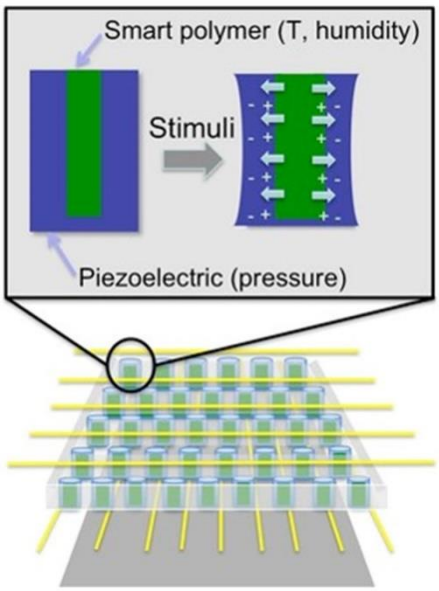


Figure 1. Concept of force/pressure, humidity and temperature responsive nanorods

## 1.2 References

[1] Brohem, C. A., da Silva Cardeal, L. B., Tiago, M., Soengas, M. S., de Moraes Barros, S. B., & Maria-Engler, S. S. (2011). Artificial skin in perspective: Concepts and applications. *Pigment Cell and Melanoma Research, 24(*1), 35–50.

[2] Zhao, J., Zhang, C., Zou, D., Liu, X., Cai, L., Li, X., & Shi, M. (2019). A Structured Design for Highly Stretchable Electronic Skin. *Advanced Materials Technologies*, *4*(10).

[3] Liu, Y., Pharr, M., & Salvatore, G. A. (2017). Lab-on-Skin: A Review of Flexible and Stretchable Electronics for Wearable Health Monitoring. In *ACS Nano, 11*(10), 9614–9635).

[4] Wan, Y., Qiu, Z., Huang, J., Yang, J., Wang, Q., Lu, P., Yang, J., Zhang, J., Huang, S., Wu, Z., & Guo, C. F. (2018). Natural Plant Materials as Dielectric Layer for Highly Sensitive Flexible Electronic Skin. *Small*, *14*(35).

[5] Gong, S., Zhang, B., Zhang, J., Wang, Z. L., & Ren, K. (2020). Biocompatible Poly(lactic acid)-Based Hybrid Piezoelectric and Electret Nanogenerator for Electronic Skin Applications. *Advanced Functional Materials*, *30*(14).

[6] Han, L., Cui, S., Yu, H. Y., Song, M., Zhang, H., Grishkewich, N., Huang, C., Kim, D., & Tam, K. M. C. (2019). Self-Healable Conductive Nanocellulose Nanocomposites for Biocompatible Electronic Skin Sensor Systems. *ACS Applied Materials and Interfaces*, *11*(47), 44642–44651.

# 2
# Fundamentals and Methods

This chapter presents an overview on the fundamentals of electronic skin design and fabrication as well as the materials and methods utilized in this thesis.

## 2.1 Electronic skin

### 2.1.1 Requirements for e-skin

Fabrication of an e-skin as close in function and behavior to the human skin imposes design considerations and requirements, such as self-healing capabilities, stretchability, flexibility, biodegradability and biocompatibility. Additionally, in applications where the e-skin is in direct contact with a human (as a wearable device), a fully transparent architecture is more user friendly and there for, while being a challenge, is an important design consideration.

#### 2.1.1.1 Self-healing

Similar to the human skin, which is capable of self-healing, the repeated long-term use of an e-skin makes it prone to mechanical damage such as scratches, fractures and cracks. Mechanical damage has a direct effect on performance deterioration (electrical damage) as well as reduced life time.[1,2] To mimic the human skin self-healing mechanism in a polymer-based e-skin, two main strategies are used:[1,3]

1. Active materials with healing agents encapsulated
2. Active materials with dynamic reversible bonds

The use of active materials with healing agents is mainly demonstrated for polymer based e-skin materials, where, in response to mechanical damage, the encapsulated healing agents are released.[2,4] Never the less, this technique is only suitable for a limited number of healing cycles, making the use of active materials with dynamic reversible bonds a more favorable approach. This is a two-step process that involves diffusion of polymer chains to the damaged regions and subsequent reformation of the bonds (ex: covalent, hydrogen, ionic or metal-ligand coordination bonds), to restore the original mechanical and electrical properties.[2] Bao et al. investigated self-healing polymer consisting of hydrogen bonds and demonstrated high healing efficiency at room temperature.[5,6] The self-healing properties of a polymer are defined by the term Healing Efficiency, which is calculated from **Equation 1**:[2]

$$Healing\ Efficiency = \frac{Property\ value\ (healed)}{Property\ value\ (prisitne)}\ x\ 100\% \qquad (1)$$

A commonly applied approach for self-healing of conductors is the use of polymer/conductor composites as an e-skin active material, where conductive nanoparticles (NPs),[7,8] nanowires (NWs),[9,10] liquid metals[11] or carbon nanotubes (CNTs)[12,13] are incorporated into a self-healing polymeric matrix. Son et al. demonstrated a concept of a self-healing polymeric matrix

and conductive CNTs.[14] The conductivity of the composite is restored due to the self-healing properties of the polymer, thus forcing the CNTs to rearrange a network in the damaged region. Wang et al. presented a self-healing multimodal e-skin tattoo based on graphene and SF/$Ca^{2+}$ film with the assistance of dynamic hydrogen bonds and coordination bonds. Within the Gr/SF/$Ca^{2+}$ composite, a drop of water enables the tattoos to self-heal with a healing efficiency of ≈100%.[15] Self-healing in semiconductor-based e-skin is still not widely investigated. Nevertheless, Bao et al. reported a self-healing organic semiconductor with exposure to temperature and vapor.[16]

#### 2.1.1.2 Stretchability and Flexibility

As previously stated, e-skin is prone to mechanical damage, which greatly reduces its ability to function properly. Mechanical strains are a main source of e-skin damage, thus a material that can maintain its performance under various strains is of high relevance. As an example, the human skin is able to stretch by 10% while still maintaining its performance.[17] Two strategies are employed to improve the stretchability of materials used in e-skin:[1]

1. Intrinsically stretchable materials
2. Geometrical arrangement of brittle materials

Some organic materials possess intrinsic stretchability, which improves robustness as well as durability but exhibit poor electrical performance. Examples of such organic materials include polydimethylsiloxane (PDMS) and polyurethane (PU), which are classified as low dielectric materials ($k < 3$).[18,19] Improvement of the electrical and dielectric properties of such stretchable organic materials is realized by composites. However, high filler concentrations will reduce the stretchability, while high concentrations of conductive filler (metal NPs or NWs) in the polymer matrix can increase the leakage current.[20] Stretchable conductors can also be realized by placing them on stretchable polymeric substrates.[2] Liquid metals such as the eutectic gallium–indium alloy are conductors with intrinsic stretchability and high conductivity, making them applicable as stretchable electrodes and interconnects.[18] Finally, Poly(3,4-ethylenedioxythiophene):polystyrene sulfonate (PEDOT:PSS) exhibits intrinsic stretchability and is widely used as a conductor because of its high conductivity.[21] The stretchability can be further improved by adding nonvolatile plasticizers, making the polymer more viscoelastic and more stretchable.[2]

The stretchability of brittle materials can be improved by geometrical designs and patterns. Geometries such as Kirigami, serpentine and horseshoe (resulting in 2D spring design) allow brittle materials to be more stretchable, as it reduces the actual applied stress.[22-24] Such geometries are curved (defined by a radius of curvature), thus offering better strain distribution.[23] Other approaches include:

1. Cracking: Using discontinuous structures/films, elasticity is achieved using discontinuous structures that can deform without loss in conductivity. Discontinuous films on elastomeric substrates can be created by cracking a thin film while maintaining a percolating pathway,[25] e.g. cracked Au films deposited an elastic substrate, which could be stretched up to 100% with high reproducibility.[26]
2. The stretchability of conductors can be improved by substrate surface roughening to promote the propagation of cracks through the conductive layer and to maintain the conductive paths.[27]
3. Deposition of a 1D-conductor network, such as silver (Ag) nanowires. 1D conductors limit accumulation of stress in the network during stretching.[28]
4. Buckling: high-modulus thin films are deposited onto a prestrained elastic substrate, when the strain is released, wrinkled (buckled) films are formed.[29] With buckles present, a device can be stretched to the value of the prestrain without inducing considerable strain in the active components. With buckling, it has been reported that porous copper (Cu) or silver (Ag) NWs can sustain strains up to 460%,[30,31] while very brittle materials such as Si nanoribbons can withstand ≈20%.[32]
5. Deposition on rigid islands: which are embedded in a softer elastomeric substrate. In this approach, devices are connected by either geometrically engineered or intrinsically stretchable interconnects. Because of the large difference in the modulus of the rigid islands and the substrate, stress is mostly applied on the interconnects, which prevents the active components from being mechanically damaged.[33]

In addition to improving the stretchability, the above-mentioned techniques improve the flexibility of materials used in e-skin. Further techniques can be implemented, which include:[1,2]

1. Depositing or embedding thin films on a low modulus soft substrate to improve bending.
2. The using of materials with high fracture strength, such as graphene or CNTs.

#### 2.1.1.3 Biocompatibility and biodegradability

In several applications, the e-skin is in close contact with biological interfaces. There for, biocompatible and biodegradable materials are essential components of an e-skin. It has been demonstrated that certain polymers such as polyvinyl acetate (PVA),[34] polycaprolactone (PCL),[35] polylactic acid (PLA)[36] and hydrogels[37] exhibit a highly biocompatible behavior. Additionally, silk fiber shows high biocompatibility coupled with diverse mechanical properties, good thermal conductivity and good electrical insulation. Moreover, It has been demonstrated in a pressure and temperature responsive e-skin.[37,38] Cellulose, another natural fiber, demonstrates biocompatible behavior and has been presented by Kharaziha et al. in a triboelectric nanogenerator (TENG) based on polycaprolactone (PCL) and cellulose paper.[39] Additionally, conventional semiconductors, such as Si, have high biocompatibility and can be

used for health monitoring and biomedical implants.[40] However, CNTs have been found to show asbestos-like behavior due to their small size and needle-like geometry.[41]

### 2.1.2 E-skin sensing modes

An efficient and effective e-skin is able to mimic and replicate the sensing capabilities of the human skin. The human skin is capable of detecting a variety of external stimuli, which helps regulate and protect the human body. Such stimuli include pressure, strain, vibrations, shear force, humidity and temperature.

#### 2.1.2.1 Tactile (Pressure and strain)

The detection of pressure and strain utilizes different transduction mechanisms, with capacitive, piezoresistive, piezoelectric, triboelectric and optical sensing mechanisms employed. However, piezoresistive and capacitive are more commonly used due to the relatively simple sensor architecture and the capability to detect static and dynamic responses.[42] **Figure 2** depicts the operational concept of pressure and strain sensors relying on piezoresistivity, capacitance and piezoelectricity.

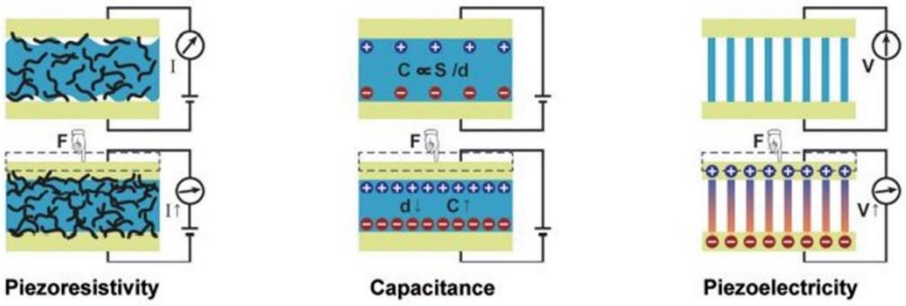


Figure 2. Schematics depicting the most common transduction mechanisms used in pressure and strain detection. Figure reproduced with permission from ref. [43]

Pressure and strain detection using a piezoresistive sensor usually relies on two mechanisms:[44]

1. Change in intrinsic resistance of the piezoresistive material, due to change in the bandgap structure.
2. Change in contact resistance $R_c$ between the piezoresistive material and the electrodes.

Therefore, the piezoresistive effect is pressure/strain induced changes in the inter-atomic spacing of a conducting or a semiconducting material, which affects the bandgap and therefore the piezoresistive coefficient $\rho_c$ as given in **Equation 2**:[44]

$$\rho_c = \frac{(\frac{\partial \rho}{\rho})}{\varepsilon} \quad (2)$$

Where, $\partial\rho$ is the change in resistivity, $\rho$ is the original resistivity and $\varepsilon$ is the strain. The Resistance *R* is related to $\rho$ through **Equation 3**:

$$R = \rho \frac{L}{A} \quad (3)$$

Where, $L$ is the conductor length and $A$ is the cross-sectional area. The Gauge Factor *GF*, which is used to describe the sensitivity *S* of a piezoresistive sensor is given in **Equation 4**:

$$GF = \frac{\frac{\Delta R}{R}}{\varepsilon} = 1 + 2v + \frac{(\frac{\partial \rho}{\rho})}{\varepsilon} \quad (4)$$

Where, $\Delta R$ is the change in resistance and $v$ is the Poisson's ratio. Piezoresistivity arising from a change in the bandgap structure is observed in several materials, such as Si, carbon nanotubes (CNTs) and graphene.[45-47] The influence of geometry on the piezoresistivity is dominant when the resistivity is constant, with a *GF* of two being ideal for sensors based a geometrical changes.[44] Utilizing both mechanisms, improves the detection range of such sensors, as $R_c$ is proportional to the square route of the force *F* (as shown in **Equation 5**), facilitating detection of low-pressure/strain (ex: detection of gas vibrations).

$$R_c \propto F^{-\frac{1}{2}} \quad (5)$$

The choice of the sensor active material takes into consideration the transduction mechanism among other factors. Skin-like flexible piezoresistive sensors are commonly fabricated from metal-based materials, such as liquid metal,[48] metal nanoparticles and nanowires.[49] Carbon-based materials such as carbon black (CB), carbon nanotubes (CNTs) and graphene are another class of materials commonly used. Due to their desirable mechanical properties

coupled with excellent electrical conductivity, conductive polymers such as PEDOT:PSS are a suitable material choice.[50]

A capacitive sensor is composed of a dielectric material sandwiched between two electrodes, with parallel-plate configuration commonly employed. Applied pressure/strain induces a change in the capacitance *C* due to geometrical deformations such as a change in the thickness *d* or the active area *A* of a dielectric, following **Equation 6**:[43]

$$C = \varepsilon_0 \varepsilon \frac{A}{d} \qquad (6)$$

Where $\varepsilon_0$ is the vacuum permittivity and $\varepsilon$ is the relative permittivity. A major advantage of capacitive sensors is the high static pressure/strain sensitivity, as well as the low power consumption.[44] Additionally, dielectrics with a wide range of dielectric constants $\varepsilon$ help expand the sensitivity as well as the detection range.[51] Recently, sensors with variable effective $\varepsilon$ are being utilized. Another concept presented by Bao and her team, relies on flexible field-effect transistors with microstructured gate dielectric as shown in **Figure 3**, to improve the sensitivity by an order of magnitude.[52]

Capacitive based pressure/strain utilize different classes of dielectric materials, based on their dielectric properties (high DK materials) and mechanical properties (active dielectric with high compressibility, nanostructured dielectrics or use of porous dielectrics).[43,44] Materials utilized in capacitive e-skin include carbon based materials (CNTs and graphene), polymers (PVDF-TrFE, PDMS and hydrogels) or composites such as Ag NW/flower/Ag NW and microstructured PVDF/NMP.[53-56]

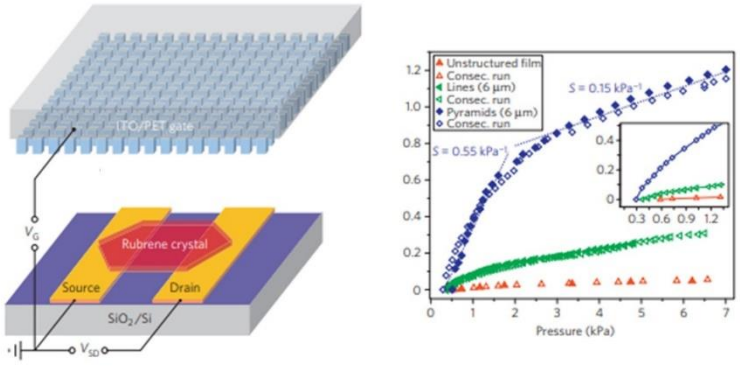


Figure 3. Flexible field-effect transistor based on microstrucutred PDMS gate dielectric for improved pressure sensitivity. Figure adapted with permission from ref. [52]

Piezoelectric pressure/strain sensors rely on the direct piezoelectric effect, where mechanical deformations induce dipole moments (due to oriented non-centrosymmetric crystals with net dipole moment ≠ 0),[43] which results in generated charge *Q* within the active piezoelectric material. The piezoelectric coefficient $d_{ij}$, calculated from **Equation 7**, is a standard parameter to consider in the design of piezoelectric sensors, where similar to the above-discussed pressure/strain sensing mechanisms, high sensitivity with a wide detection range is preferred. Inorganic piezoelectric materials exhibit high $d_{33}$ and $d_{31}$ values but are brittle ($d_{33\text{-}PZT}$ ≈ 570−650 pC $N^{-1}$ values),[57] while the opposite is observed for organic piezoelectric materials ($d_{33\text{-}PVDF\text{-}TrFE}$ = −32 pC $N^{-1}$).[58] However, different approaches are used to provide flexible high $d_{33}$ and $d_{31}$ coefficient piezoelectric materials such as:

1. Deposition of thin inorganic materials with high piezoelectric coefficients on flexible substrates such as barium titinate thin films on PTFE or ZnO NWs on PET[59,60]
2. Polymer/inorganic composites, such as P(VDF-TrFE)/BT, BTO-PVDF/GO[20]
3. Steady piezoelectrets (porous structures with electric charge internal cavities)[61]

$$d_{nij} = \frac{\partial D_n}{\partial T_{ij}} = \frac{\partial S_{ij}}{\partial E_n} \tag{7}$$

Where *d* is the piezoelectric coefficient, *D* is the electric displacement, *T* is the stress, *S* is the strain and *E* is the electric field. Triboelectric nanogenerators (TENGs) have demonstrated excellent performance in energy harvesting as well as pressure/strain sensing.[44] The triboelectric effect is based on the ability of materials to become electrically charged (surface charges) when in contact with another surface and is expressed through an equivalent capacitance following **Equation 8**:[62]

$$C = \frac{\varepsilon S}{4\pi k \lambda} \tag{8}$$

Where, *C* is the capacitance, $\varepsilon$ is the relative permitivitty, *k* is the electrostatic constant and $\lambda$ is the charge penetration depth. While the output voltage *V* is expressed in relation to the surface charge density following **Equation 9**:

$$V = f(Q) \cong \left(A_{eff} \cdot \sigma\right) \tag{9}$$

Where, *Q* is the charge, $\sigma$ is the surface charge density with an effective area $A_{eff}$. Material combinations utilized in TENGs include Wrinkled PEDOT:PSS, ion-conducting elastomers, Ag NWs-MoS2/PDMS and PDMS Films/P(VDF-TrFE).[63-65]

Optical-based pressure/force sensors convert the mechanical input into an electrical output through an intermediate light source. The conversion mechanism requires a sensor equipped with a light source, transmission medium and a detector. Such concepts rely on the modulation of light intensity by using flexible fiber optics or force-sensitive waveguides. Fiber optics exhibit a linear response coupled with low drift but are poorly stretchable. They can be replaced by elastomer based waveguides such as PDMS, as shown in **Figure 4**.[1] Another concept of strain sensors rely on a wireless antenna fixed on an elastic substrate, where applied strain causes a shift in the resonance frequency of the sensor.[66,67]

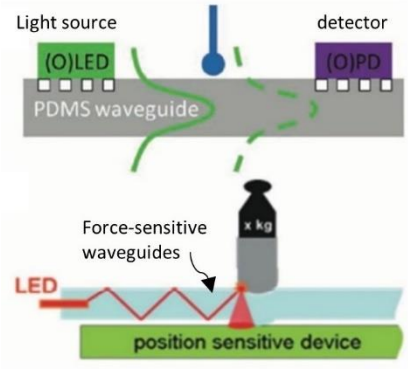


Figure 4. Schematics of optical-based pressure/force sensor. Figure adapted with permission from ref. [1]

Shear force is another type of force, which is sensed by the human skin. In e-skin applications, several concepts, such as nanohairs have been proposed to sense shear forces.[68-70] One concept proposed by Pang et al., in which the team fabricated a wearable shear force sensor composed of two interlocked arrays of high aspect ratio (AR) platinum-coated polymer nanofibers on PDMS thin film.[68] Sensitivity to shear force is transmitted to a change in the electrical resistance. Another concept relies on two flexible layers with interlocked microdome arrays, with high sensitivity to shear forces. Additionally, capacitive-type sensors, with sensitivity to pressure and shear forces have been realized.[70]

#### 2.1.2.2 Humidity

Sensitivity to surrounding humidity changes is an essential requirement for an e-skin. Such sensors can be used in medical applications such as monitoring of human respiration and sweat release.[71,72] Similar to pressure and strain sensors, different transduction mechanisms are employed, such as, resistance, capacitance, piezoelectricity and optical.[3] According to literature, resistive-type humidity sensors are commonly employed in e-skin, which usually consists of an inorganic conductor and a hydrophilic polymer. The hydrophilic polymer facilitates water molecules adsorption and absorption resulting in a change in the conductance/resistance of the conductor. Following such concept, a wide variety of material combinations have been reported.[73-77] Such as, combining flexible conductive rubber with citric acid and Ag nanoparticles or flexible cellulose nanofibers and CNT.[72] Another approach to fabricate flexible humidity sensors for e-skin is ions embedded in a hydrophilic polymer: PVA/KOH porous ionic membranes, which are characterized by a drop in the resistance with increased humidity (K+ and OH- ions interact with water molecules forming an electrolyte solution).[78]

#### 2.1.2.3 Temperature

Through thermoreceptors, the human skin is able to detect surrounding changes in temperature, making temperature sensitivity a prerequisite for an e-skin. Commonly used temperature sensors are composed of pure metals or ceramic semiconductors, which are used for their thermoresistive effect (change in charge carrier density and/or charge carrier mobility as a function of temperature).[3] The thermoresistive effect represented by the temperature coefficient of resistance or *α* is calculated following **Equation 10**: [79]

$$\alpha = \frac{R - R_0}{T * T_0} \qquad (10)$$

Where, *R* is the resistance at a specific temperature, $R_0$ is the initial resistance, *T* and $T_0$ are the equivalent temperatures. Due to their poor mechanical properties, namely flexibility, ceramics and metals are not suitable for e-skin devices, unless structurally modified, e.g. metal/Si nanoribbons with enhanced strechability.[80] Graphene, CNT and nanoparticles are promising materials for thermoresistive temperature sensors.[81-85] Two main classes of thermoresistive sensors are present: 1) metal-based temperature sensors, which exhibit an increase in the resistivity with increasing temperature, due to a decrease in the charge mobility. 2) semiconductor-based temperature sensors, which exhibit a decrease in resistivity, due to an increase in the charge carrier density.[86]

In addition to the thermoresisitive effect, the thermoelectric and pyroelectric effects are commonly used in temperature sensors. A main advantage of sensors relying on both effects is that they do not require to be powered externally (active sensors).[86] A thermoelectric temperature sensor generates electricity due to the Seebeck effect, calculated following **Equation 11** and **12**.

$$J = -\sigma \Delta V - \sigma S \Delta T \qquad (11)$$

And

$$S = -\frac{\Delta V}{\Delta T} \qquad (12)$$

Where, *J* is the current density, $\sigma$ is the electrical conductivity, *S* is the Seebeck coefficient, $\Delta V$ is the voltage and $\Delta T$ is the change in temperature. Zhu et al. fabricated a thermoelectric temperature sensor based on porous PU and PEDOT:PSS.[87] A pyroelectric temperature sensor generates an electrical output due to the electrical polarization and is represented by the pyroelectric coefficient *p*, calculated from **Equation 13**. Ko et al. fabricated such sensors based on reduced Graphene oxide/ PVDF composites.[88]

$$p_i = \frac{\partial P}{\partial T} \qquad (13)$$

Where *P* is the electric polarization and *T* is the temperature. Independent of the effect used in the e-skin compatible temperature sensor, high sensitivity, wide sensing range, high linearity and low hysteresis are of high importance. Generally, temperature sensors are demonstrated to exhibit large response and recovery time, which is attributed to the long thermal diffusion time.[3] However, it has been demonstrated by Cho et al. that a reduced substrate thickness reduces the thermal diffusion time, leading to faster response (100 ms).[89]

#### 2.1.2.4 Multi-stimuli

As previously discussed, an efficient e-skin is capable of multi-stimuli sensing, as single-stimulus sensors do not provide sufficient information. Different multi-stimuli responsive e-skins are investigated to mimic the behavior of a human skin, which is sensitive to stimuli such as pressure, strain, humidity, temperature and gases:[4]

1. Pressure/strain-temperature
2. Pressure/strain-humidity
3. Pressure/strain-gas
4. Pressure/strain-temperature-humidity
5. Pressure/strain-temperature-gas-light

An example of pressure-temperature multimodal sensing is demonstrated by Chen et al., where a rGO-paper composite material was utilized.[90] The composite utilizes its piezoelectric and thermoresistive properties and demonstrates a *GF* value of 18.96 for compressive strain and $\Delta R$ of -11.3% for a temperature range between 27 and 65°C. Additionally, a combination of GO and rGO with graphene electrodes on PDMS substrate is demonstrated by Cho and coworkers to deliver pressure/strain-temperature-humidity multimodal sensitivity.[91] Another concept presented relies on capacitive sensing, with a sensor composed of an ionic liquid (serves as an electrode), a microfluidic channel and CNT/PDMS dielectric layer.[92] The sensor is sensitive to vertical and lateral pressure, through changes in the conductivity, as well as temperature through changes in the capacitance (associated with the formation of an electric double layer within the ionic liquid-CNT/PDMS composite interface). Zhang et al. presented a pressure-humidity multimodal sensor, which is composed of screen-printed silk-fibroin triboelectric nanogenerator.[93] Humidity is detected through change in the capacitance, while pressure is detected through change in the output voltage. Another pressure-humidity multimodal sensor composed of paper, porous polyamide PI prepared by direct laser writing method is presented by Liu et al.[94] Carbon-based materials are proven to be the most suitable candidate for pressure/strain-gas multimodal sensors.[4] This is due to availability, very good electrical properties and gas detection functionalities. Gao et al. fabricated such sensors using a nanofiber composite film composed of hydrolyzed methyltrichlorosilane on the surface of acid modified CNTs on PU/polystyrene-block-poly(ethylene-co-butylene)-block polystyrene nanofibers.[95] A concept of multimodal sensing of pressure/strain-temperature-roughness is presented by Park et al., where a PVDF-rGO ferroelectric composite is used to detect changes in pressure, temperature, humidity and high-frequency dynamic soundwaves.[88] Huang and coworkers presented a sensor composed of CB and rGO sprayed onto a paper substrate, with sensitivity to pressure, strain, temperature and humidity. However, high cross-talk is observed due to measuring only current, while other designs can use two or more signals.[96]

### 2.1.3 References


[1] Hammock, M. L., Chortos, A., Tee, B. C. K., Tok, J. B. H., & Bao, Z. (2013). 25th anniversary article: The evolution of electronic skin (E-Skin): A brief history, design considerations, and recent progress. *Advanced Materials*, *25*(42), 5997–6038.

[2] Yang, J. C., Mun, J., Kwon, S. Y., Park, S., Bao, Z., & Park, S. (2019). Electronic Skin: Recent Progress and Future Prospects for Skin-Attachable Devices for Health Monitoring, Robotics, and Prosthetics. *Advanced Materials, 31*(48).

[3] Chen, J., Zhu, Y., Chang, X., Pan, D., Song, G., Guo, Z., & Naik, N. (2021). Recent Progress in Essential Functions of Soft Electronic Skin. In *Advanced Functional Materials, 31*(42).

[4] Guo, Y., Wei, X., Gao, S., Yue, W., Li, Y., & Shen, G. (2021). Recent Advances in Carbon Material-Based Multifunctional Sensors and Their Applications in Electronic Skin Systems. In *Advanced Functional Materials, 31*(40).

[5] Kang, J., Son, D., Wang, G. J. N., Liu, Y., Lopez, J., Kim, Y., Oh, J. Y., Katsumata, T., Mun, J., Lee, Y., Jin, L., Tok, J. B. H., & Bao, Z. (2018). Tough and Water-Insensitive Self-Healing Elastomer for Robust Electronic Skin. *Advanced Materials*, *30*(13).

[6] Kim, S. H., Seo, H., Kang, J., Hong, J., Seong, D., Kim, H. J., Kim, J., Mun, J., Youn, I., Kim, J., Kim, Y. C., Seok, H. K., Lee, C., Tok, J. B. H., Bao, Z., & Son, D. (2019). An Ultrastretchable and Self-Healable Nanocomposite Conductor Enabled by Autonomously Percolative Electrical Pathways. *ACS Nano*, *13*(6), 6531–6539.

[7] Tee, B. C. K., Wang, C., Allen, R., & Bao, Z. (2012). An electrically and mechanically self-healing composite with pressure- and flexion-sensitive properties for electronic skin applications. *Nature Nanotechnology*, *7*(12), 825–832.

[8] Zhang, Q., Niu, S., Wang, L., Lopez, J., Chen, S., Cai, Y., Du, R., Liu, Y., Lai, J. C., Liu, L., Li, C. H., Yan, X., Liu, C., Tok, J. B. H., Jia, X., & Bao, Z. (2018). An Elastic Autonomous Self-Healing Capacitive Sensor Based on a Dynamic Dual Crosslinked Chemical System. *Advanced Materials*, *30*(33).

[9] Li, J., Liang, J., Li, L., Ren, F., Hu, W., Li, J., Qi, S., & Pei, Q. (2014). Healable capacitive touch screen sensors based on transparent composite electrodes comprising silver nanowires and a furan/maleimide diels-Alder cycloaddition polymer. *ACS Nano*, *8*(12).

[10] Gong, C., Liang, J., Hu, W., Niu, X., Ma, S., Hahn, H. T., & Pei, Q. (2013). A healable, semitransparent silver nanowire-polymer composite conductor. *Advanced Materials*, *25*(30), 4186–4191.

[11] Palleau, E., Reece, S., Desai, S. C., Smith, M. E., & Dickey, M. D. (2013). Self-healing stretchable wires for reconfigurable circuit wiring and 3D microfluidics. *Advanced Materials*, *25*(11), 1589–1592.

[12] Sun, H., You, X., Jiang, Y., Guan, G., Fang, X., Deng, J., Chen, P., Luo, Y., & Peng, H. (2014). Self-Healable Electrically Conducting Wires for Wearable Microelectronics. *Angewandte Chemie*, *126*(36), 9680–9685.

[13] Guo, K., Zhang, D.-L., Zhang, X.-M., Zhang, J., Ding, L.-S., Li, B.-J., & Zhang, S. (2015). Conductive Elastomers with Autonomic Self-Healing Properties. *Angewandte Chemie*, *127*(41), 12295–12301.

[14] Son, D., Kang, J., Vardoulis, O., Kim, Y., Matsuhisa, N., Oh, J. Y., To, J. W., Mun, J., Katsumata, T., Liu, Y., McGuire, A. F., Krason, M., Molina-Lopez, F., Ham, J., Kraft, U., Lee, Y., Yun, Y., Tok, J. B. H., & Bao, Z. (2018). An integrated self-healable electronic skin system fabricated via dynamic reconstruction of a nanostructured conducting network. *Nature Nanotechnology*, *13*(11), 1057–1065.

[15] Wang, Q., Ling, S., Liang, X., Wang, H., Lu, H., & Zhang, Y. (2019). Self-Healable Multifunctional Electronic Tattoos Based on Silk and Graphene. *Advanced Functional Materials*, *29*(16).

[16] Oh, J. Y., Rondeau-Gagné, S., Chiu, Y. C., Chortos, A., Lissel, F., Wang, G. J. N., Schroeder, B. C., Kurosawa, T., Lopez, J., Katsumata, T., Xu, J., Zhu, C., Gu, X., Bae, W. G., Kim, Y., Jin, L., Chung, J. W., Tok, J. B. H., & Bao, Z. (2016). Intrinsically stretchable and healable semiconducting polymer for organic transistors. *Nature*, *539*(7629), 411–415.

[17] Chortos, A., Liu, J., & Bao, Z. (2016). Pursuing prosthetic electronic skin. In *Nature Materials, 15*(9), 937–950.

[18] Chortos, A., Lim, J., To, J. W. F., Vosgueritchian, M., Dusseault, T. J., Kim, T. H., Hwang, S., & Bao, Z. (2014). Highly stretchable transistors using a microcracked organic semiconductor. *Advanced Materials*, *26*(25), 4253–4259.

[19] Xu, J., Wang, S., Nathan Wang, G.-J., Zhu, C., Luo, S., Jin, L., Gu, X., Chen, S., Feig, V. R., F To, J. W., Rondeau-Gagné, S., Park, J., Schroeder, B. C., Lu, C., Young Oh, J., Wang, Y., Kim, Y.-H., Yan, H., Sinclair, R., … Bao, Z. (n.d.). *Highly stretchable polymer semiconductor films through the nanoconfinement effect*.

[20] Ali, T. A., Groten, J., Clade, J., Collin, D., Schaffner, P., Zirkl, M., Coclite, A. M., Domann, G., & Stadlober, B. (2020). Screen-Printed Ferroelectric P(VDF-TrFE)-co-PbTiO3and P(VDF-TrFE)- co-NaBiTi2O6Nanocomposites for Selective Temperature and Pressure Sensing. *ACS Applied Materials and Interfaces*, *12*(34), 38614–38625.

[21] Wang, Y., Zhu, C., Pfattner, R., Yan, H., Jin, L., Chen, S., Molina-Lopez, F., Lissel, F., Liu, J., Rabiah, N. I., Chen, Z., Chung, J. W., Linder, C., Toney, M. F., Murmann, B., & Bao, Z. (n.d.). *A P P L I E D S C I E N C E S A N D E N G I N E E R I N G A highly stretchable, transparent, and conductive polymer*.

[22] Vanfleteren, J., Gonzalez, M., Bossuyt, F., Hsu, Y., Vervust, T., De Wolf, I., & Jablonski, M. (2012). Printed circuit board technology inspired stretchable circuits. MRS Bulletin, 37(3), 254-260.

[23] Gonzalez, M., Axisa, F., Bulcke, M. vanden, Brosteaux, D., Vandevelde, B., & Vanfleteren, J. (2008). Design of metal interconnects for stretchable electronic circuits. *Microelectronics Reliability*, *48*(6), 825–832.

[24] Xu, S., Zhang, Y., Cho, J., Lee, J., Huang, X., Jia, L., Fan, J. A., Su, Y., Su, J., Zhang, H., Cheng, H., Lu, B., Yu, C., Chuang, C., Kim, T. il, Song, T., Shigeta, K., Kang, S., Dagdeviren, C., … Rogers, J. A. (2013). Stretchable batteries with self-similar serpentine interconnects and integrated wireless recharging systems. *Nature Communications*, *4*.

[25] Lu, N., Wang, X., Suo, Z., & Vlassak, J. (2007). Metal films on polymer substrates stretched beyond 50%. *Applied Physics Letters*, *91*(22).

[26] Graudejus, O., Görrn, P., & Wagner, S. (2010). Controlling the morphology of gold films on poly(dimethylsiloxane). *ACS Applied Materials and Interfaces*, *2*(7), 1927–1933.

[27] Jeong, J., Kim, S., Cho, J., & Hong, Y. (2009). Stable stretchable silver electrode directly deposited on wavy elastomeric substrate. *IEEE Electron Device Letters*, *30*(12), 1284–1286.

[28] Hu, W., Niu, X., Li, L., Yun, S., Yu, Z., & Pei, Q. (2012). Intrinsically stretchable transparent electrodes based on silver-nanowire-crosslinked-polyacrylate composites. *Nanotechnology*, *23*(34).

[29] Watanabe, M., Shirai, H., & Hirai, T. (2002). Wrinkled polypyrrole electrode for electroactive polymer actuators. *Journal of Applied Physics*, *92*(8), 4631–4637.

[30] Wang, X., Hu, H., Shen, Y., Zhou, X., & Zheng, Z. (2011). Stretchable conductors with ultrahigh tensile strain and stable metallic conductance enabled by prestrained polyelectrolyte nanoplatforms. *Advanced Materials*, *23*(27), 3090–3094.

[31] Lee, P., Lee, J., Lee, H., Yeo, J., Hong, S., Nam, K. H., Lee, D., Lee, S. S., & Ko, S. H. (2012). Highly stretchable and highly conductive metal electrode by very long metal nanowire percolation network. *Advanced Materials*, *24*(25), 3326–3332.

[32] Rogers, J. A., Someya, T., & Huang, Y. (n.d.). *Materials and Mechanics for Stretchable Electronics*.

[33] Lee, J., Wu, J., Shi, M., Yoon, J., Park, S. il, Li, M., Liu, Z., Huang, Y., & Rogers, J. A. (2011). Stretchable GaAs photovoltaics with designs that enable high areal coverage. *Advanced Materials*, *23*(8), 986–991.

[34] Teng, L., Ye, S., Handschuh-Wang, S., Zhou, X., Gan, T., & Zhou, X. (2019). Liquid Metal-Based Transient Circuits for Flexible and Recyclable Electronics. *Advanced Functional Materials*, *29*(11).

[35] Cui, T., Yu, J., Li, Q., Wang, C. F., Chen, S., Li, W., & Wang, G. (2020). Large-Scale Fabrication of Robust Artificial Skins from a Biodegradable Sealant-Loaded Nanofiber Scaffold to Skin Tissue via Microfluidic Blow-Spinning. *Advanced Materials*, *32*(32).

[36] Guo, Y., Zhong, M., Fang, Z., Wan, P., & Yu, G. (2019). A Wearable Transient Pressure Sensor Made with MXene Nanosheets for Sensitive Broad-Range Human-Machine Interfacing. *Nano Letters*, *19*(2), 1143–1150.

[37] Guo, Y., Wei, X., Gao, S., Yue, W., Li, Y., & Shen, G. (2021). Recent Advances in Carbon Material-Based Multifunctional Sensors and Their Applications in Electronic Skin Systems. *Advanced Functional Materials, 31*(40).

[38] Wu, R., Ma, L., Hou, C., Meng, Z., Guo, W., Yu, W., Yu, R., Hu, F., & Liu, X. Y. (2019). Silk Composite Electronic Textile Sensor for High Space Precision 2D Combo Temperature–Pressure Sensing. *Small*, *15*(31).

[39] Parandeh, S., Kharaziha, M., & Karimzadeh, F. (2019). An eco-friendly triboelectric hybrid nanogenerators based on graphene oxide incorporated polycaprolactone fibers and cellulose paper. *Nano Energy*, *59*, 412–421.

[40] Kang, S. K., Murphy, R. K. J., Hwang, S. W., Lee, S. M., Harburg, D. v., Krueger, N. A., Shin, J., Gamble, P., Cheng, H., Yu, S., Liu, Z., McCall, J. G., Stephen, M., Ying, H., Kim, J., Park, G., Webb, R. C., Lee, C. H., Chung, S., … Rogers, J. A. (2016). Bioresorbable silicon electronic sensors for the brain. *Nature*, *530*(7588), 71–76.

[41] Poland, C. A., Duffin, R., Kinloch, I., Maynard, A., Wallace, W. A. H., Seaton, A., Stone, V., Brown, S., MacNee, W., & Donaldson, K. (2008). Carbon nanotubes introduced into the abdominal cavity of mice show asbestos-like pathogenicity in a pilot study. *Nature Nanotechnology*, *3*(7), 423–428.

[42] Ha, M., Lim, S., & Ko, H. (2018). Wearable and flexible sensors for user-interactive health-monitoring devices. In *Journal of Materials Chemistry B, 6(24)*, 4043–4064.

[43] Wang, X., Dong, L., Zhang, H., Yu, R., Pan, C., & Wang, Z. L. (2015). Recent Progress in Electronic Skin. In *Advanced Science, 2*(10).

[44] Pierre Claver, U., & Zhao, G. (2021). Recent Progress in Flexible Pressure Sensors Based Electronic Skin. In *Advanced Engineering Materials, 23*(5).

[45] Kumar, S. S., & Pant, B. D. (2014). Design principles and considerations for the “ideal” silicon piezoresistive pressure sensor: A focused review. *Microsystem Technologies*, *20*(7), 1213–1247.

[46] Zhao, X. F., Hang, C. Z., Wen, X. H., Liu, M. Y., Zhang, H., Yang, F., Ma, R. G., Wang, J. C., Zhang, D. W., & Lu, H. L. (2020). Ultrahigh-Sensitive Finlike Double-Sided E-Skin for Force Direction Detection. *ACS Applied Materials and Interfaces*, *12*(12), 14136–14144.

[47] Luo, Y., Wu, D., Zhao, Y., Chen, Q., Xie, Y., Wang, M., Lin, L., Wang, L., & Sun, D. (2019). Direct write of a flexible high-sensitivity pressure sensor with fast response for electronic skins. *Organic Electronics*, *67*, 10–18.

[48] Yun, G., Tang, S. Y., Sun, S., Yuan, D., Zhao, Q., Deng, L., Yan, S., Du, H., Dickey, M. D., & Li, W. (2019). Liquid metal-filled magnetorheological elastomer with positive piezoconductivity. *Nature Communications*, *10*(1).

[49] Fan, Y. J., Li, X., Kuang, S. Y., Zhang, L., Chen, Y. H., Liu, L., Zhang, K., Ma, S. W., Liang, F., Wu, T., Wang, Z. L., & Zhu, G. (2018). Highly Robust, Transparent, and Breathable Epidermal Electrode. *ACS Nano*, *12*(9), 9326–9332.

[50] Ding, Y., Yang, J., Tolle, C. R., & Zhu, Z. (2018). Flexible and Compressible PEDOT:PSS@Melamine Conductive Sponge Prepared via One-Step Dip Coating as Piezoresistive Pressure Sensor for Human Motion Detection. *ACS Applied Materials and Interfaces*, *10*(18), 16077–16086.

[51] Zang, Y., Zhang, F., Huang, D., Gao, X., Di, C. A., & Zhu, D. (2015). Flexible suspended gate organic thin-film transistors for ultra-sensitive pressure detection. *Nature Communications*, *6*.

[52] Mannsfeld, S. C. B., Tee, B. C. K., Stoltenberg, R. M., Chen, C. V. H. H., Barman, S., Muir, B. V. O., Sokolov, A. N., Reese, C., & Bao, Z. (2010). Highly sensitive flexible pressure sensors with microstructured rubber dielectric layers. *Nature Materials*, *9*(10), 859–864.

[53] Yang, X., Wang, Y., & Qing, X. (2019). A flexible capacitive sensor based on the electrospun PVDF nanofiber membrane with carbon nanotubes. *Sensors and Actuators, A: Physical*, *299*.

[54] You, X., He, J., Nan, N., Sun, X., Qi, K., Zhou, Y., Shao, W., Liu, F., & Cui, S. (2018). Stretchable capacitive fabric electronic skin woven by electrospun nanofiber coated yarns for detecting tactile and multimodal mechanical stimuli. *Journal of Materials Chemistry C*, *6*(47), 12981–12991.

[55] Liu, Y. Q., Zhang, J. R., Han, D. D., Zhang, Y. L., & Sun, H. B. (2019). Versatile Electronic Skins with Biomimetic Micronanostructures Fabricated Using Natural Reed Leaves as Templates. *ACS Applied Materials and Interfaces*, *11*(41), 38084–38091.

[56] Qiu, J., Guo, X., Chu, R., Wang, S., Zeng, W., Qu, L., Zhao, Y., Yan, F., & Xing, G. (2019). Rapid-Response, Low Detection Limit, and High-Sensitivity Capacitive Flexible Tactile Sensor Based on Three-Dimensional Porous Dielectric Layer for Wearable Electronic Skin. *ACS Applied Materials and Interfaces*, *11*(43), 40716–40725.

[57] Tichý, J., Erhart, J., Kittinger, E., & Prívratská, J. (2010). *Fundamentals of piezoelectric sensorics: mechanical, dielectric, and thermodynamical properties of piezoelectric materials*. Springer Science & Business Media.

[58] Zirkl, M., Sawatdee, A., Helbig, U., Krause, M., Scheipl, G., Kraker, E., ... & Stadlober, B. (2011). An all-printed ferroelectric active matrix sensor network based on only five functional materials forming a touchless control interface. *Advanced Materials*, *23*(18), 2069-2074.

[59] Park, K. I., Xu, S., Liu, Y., Hwang, G. T., Kang, S. J. L., Wang, Z. L., & Lee, K. J. (2010). Piezoelectric BaTiO3 thin film nanogenerator on plastic substrates. *Nano letters*, *10*(12), 4939-4943.

[60] Panth, M., Cook, B., Zhang, Y., Ewing, D., Tramble, A., Wilson, A., & Wu, J. (2020). High-performance strain sensors based on vertically aligned piezoelectric zinc oxide nanowire array/graphene nanohybrids. *ACS Applied Nano Materials*, *3*(7), 6711-6718.

[61] Martínez-Ayuso, G., Friswell, M. I., Adhikari, S., Khodaparast, H. H., & Berger, H. (2017). Homogenization of porous piezoelectric materials. *International Journal of solids and Structures*, *113*, 218-229.

[62] Pan, S., & Zhang, Z. (2019). Fundamental theories and basic principles of triboelectric effect: A review. *Friction, 7*(1), 2-17.

[63] Wen, Z., Yang, Y., Sun, N., Li, G., Liu, Y., Chen, C. & Sun, X. (2018). A wrinkled PEDOT: PSS film based stretchable and transparent triboelectric nanogenerator for wearable energy harvesters and active motion sensors. *Advanced Functional Materials*, *28*(37), 1803684.

[64] Lan, L., Yin, T., Jiang, C., Li, X., Yao, Y., Wang, Z. & Ying, Y. (2019). Highly conductive 1D-2D composite film for skin-mountable strain sensor and stretchable triboelectric nanogenerator. *Nano Energy*, *62*, 319-328.

[65] Liu, T., Liu, M., Dou, S., Sun, J., Cong, Z., Jiang, C. & Wang, Z. L. (2018). Triboelectric-nanogenerator-based soft energy-harvesting skin enabled by toughly bonded elastomer/hydrogel hybrids. *ACS nano*, *12*(3), 2818-2826.

[66] So, J. H., Thelen, J., Qusba, A., Hayes, G. J., Lazzi, G., & Dickey, M. D. (2009). Reversibly deformable and mechanically tunable fluidic antennas. *Advanced Functional Materials*, *19*(22), 3632-3637.

[67] Mazlouman, S. J., Jiang, X. J., Mahanfar, A. N., Menon, C., & Vaughan, R. G. (2011). A reconfigurable patch antenna using liquid metal embedded in a silicone substrate. *IEEE Transactions on Antennas and Propagation*, *59*(12), 4406-4412.

[68] Pang, C., Lee, G. Y., Kim, T. I., Kim, S. M., Kim, H. N., Ahn, S. H., & Suh, K. Y. (2012). A flexible and highly sensitive strain-gauge sensor using reversible interlocking of nanofibres. *Nature materials*, *11*(9), 795-801.

[69] Chun, S., Son, W., Choi, C., Min, H., Kim, J., Lee, H. J. & Pang, C. (2019). Bioinspired hairy skin electronics for detecting the direction and incident angle of airflow. *ACS applied materials & interfaces*, *11*(14), 13608-13615.

[70] Park, J., Lee, Y., Hong, J., Lee, Y., Ha, M., Jung, Y. & Ko, H. (2014). Tactile-direction-sensitive and stretchable electronic skins based on human-skin-inspired interlocked microstructures. *ACS nano*, *8*(12), 12020-12029.

[71] Jiang, B., Bi, Z., Hao, Z., Yuan, Q., Feng, D., Zhou, K. & Zhao, J. (2019). Graphene oxide-deposited tilted fiber grating for ultrafast humidity sensing and human breath monitoring. *Sensors and Actuators B: Chemical*, *293*, 336-341.

[72] Xu, C., Zheng, Z., Lin, M., Shen, Q., Wang, X., Lin, B., & Fu, L. (2020). Strengthened, antibacterial, and conductive flexible film for humidity and strain sensors. *ACS applied materials & interfaces*, *12*(31), 35482-35492.

[73] Zhu, P., Liu, Y., Fang, Z., Kuang, Y., Zhang, Y., Peng, C., & Chen, G. (2019). Flexible and highly sensitive humidity sensor based on cellulose nanofibers and carbon nanotube composite film. *Langmuir*, *35*(14), 4834-4842.

[74] Wang, D., Huang, Y., Ma, Y., Liu, P., Liu, C., & Zhang, Y. (2014). Research on highly sensitive humidity sensor based on Tr-MWCNT/HEC composite films. *Journal of Materials Research*, *29*(23), 2845-2853.

[75] Yoo, K. P., Lim, L. T., Min, N. K., Lee, M. J., Lee, C. J., & Park, C. W. (2010). Novel resistive-type humidity sensor based on multiwall carbon nanotube/polyimide composite films. *Sensors and Actuators B: Chemical*, *145*(1), 120-125.

[76] Fei, T., Jiang, K., Jiang, F., Mu, R., & Zhang, T. (2014). Humidity switching properties of sensors based on multiwalled carbon nanotubes/polyvinyl alcohol composite films. *Journal of Applied Polymer Science*, *131*(1).

[77] Zhou, G., Byun, J. H., Oh, Y., Jung, B. M., Cha, H. J., Seong, D. G., ... & Chou, T. W. (2017). Highly sensitive wearable textile-based humidity sensor made of high-strength, single-walled carbon nanotube/poly (vinyl alcohol) filaments. *ACS applied materials & interfaces*, *9*(5), 4788-4797.

[78] Li, T., Li, L., Sun, H., Xu, Y., Wang, X., Luo, H., ... & Zhang, T. (2017). Porous ionic membrane based flexible humidity sensor and its multifunctional applications. *Advanced science*, *4*(5), 1600404.

[79] Cui, Z., Poblete, F. R., & Zhu, Y. (2019). Tailoring the temperature coefficient of resistance of silver nanowire nanocomposites and their application as stretchable temperature sensors. *ACS applied materials & interfaces*, *11*(19), 17836-17842.

[80] Yang, T., Xie, D., Li, Z., & Zhu, H. (2017). Recent advances in wearable tactile sensors: Materials, sensing mechanisms, and device performance. *Materials Science and Engineering: R: Reports*, *115*, 1-37.

[81] Webb, R. C., Bonifas, A. P., Behnaz, A., Zhang, Y., Yu, K. J., Cheng, H., ... & Rogers, J. A. (2013). Ultrathin conformal devices for precise and continuous thermal characterization of human skin. *Nature materials*, *12*(10), 938-944.

[82] Yang, J., Wei, D., Tang, L., Song, X., Luo, W., Chu, J., ... & Du, C. (2015). Wearable temperature sensor based on graphene nanowalls. *Rsc Advances*, *5*(32), 25609-25615.

[83] Harada, S., Honda, W., Arie, T., Akita, S., & Takei, K. (2014). Fully printed, highly sensitive multifunctional artificial electronic whisker arrays integrated with strain and temperature sensors. *ACS nano*, *8*(4), 3921-3927.

[84] Joh, H., Lee, S. W., Seong, M., Lee, W. S., & Oh, S. J. (2017). Engineering the Charge Transport of Ag Nanocrystals for Highly Accurate, Wearable Temperature Sensors through All-Solution Processes. *Small*, *13*(24), 1700247.

[85] Yan, C., Wang, J., & Lee, P. S. (2015). Stretchable graphene thermistor with tunable thermal index. *ACS nano*, *9*(2), 2130-2137.

[86] Yang, J. C., Mun, J., Kwon, S. Y., Park, S., Bao, Z., & Park, S. (2019). Electronic Skin: Recent Progress and Future Prospects for Skin-Attachable Devices for Health Monitoring, Robotics, and Prosthetics. *Advanced Materials, 31*(48).

[87] Zhang, F., Zang, Y., Huang, D., Di, C. A., & Zhu, D. (2015). Flexible and self-powered temperature–pressure dual-parameter sensors using microstructure-frame-supported organic thermoelectric materials. *Nature communications*, *6*(1), 1-10.

[88] Park, J., Kim, M., Lee, Y., Lee, H. S., & Ko, H. (2015). Fingertip skin–inspired microstructured ferroelectric skins discriminate static/dynamic pressure and temperature stimuli. *Science advances*, *1*(9), e1500661.

[89] Bae, G. Y., Han, J. T., Lee, G., Lee, S., Kim, S. W., Park, S., ... & Cho, K. (2018). Pressure/temperature sensing bimodal electronic skin with stimulus discriminability and linear sensitivity. *Advanced Materials*, *30*(43), 1803388.

[90] Chen, L., Weng, M., Zhou, P., Huang, F., Liu, C., Fan, S., & Zhang, W. (2019). Graphene-Based Actuator with Integrated-Sensing Function. *Advanced Functional Materials*, *29*(5), 1806057.

[91] Ho, D. H., Sun, Q., Kim, S. Y., Han, J. T., Kim, D. H., & Cho, J. H. (2016). Stretchable and multimodal all graphene electronic skin. *Advanced Materials*, *28*(13), 2601-2608.

[92] Yoon, S. G., & Chang, S. T. (2017). Microfluidic capacitive sensors with ionic liquid electrodes and CNT/PDMS nanocomposites for simultaneous sensing of pressure and temperature. *Journal of Materials Chemistry C*, *5*(8), 1910-1919.

[93] Wen, D. L., Liu, X., Deng, H. T., Sun, D. H., Qian, H. Y., Brugger, J., & Zhang, X. S. (2019). Printed silk-fibroin-based triboelectric nanogenerators for multi-functional wearable sensing. *Nano Energy*, *66*, 104123.

[94] Luo, J., Yao, Y., Duan, X., & Liu, T. (2018). Force and humidity dual sensors fabricated by laser writing on polyimide/paper bilayer structure for pulse and respiration monitoring. *Journal of Materials Chemistry C*, *6*(17), 4727-4736.

[95] Gao, J., Wang, L., Guo, Z., Li, B., Wang, H., Luo, J., ... & Xue, H. (2020). Flexible, superhydrophobic, and electrically conductive polymer nanofiber composite for multifunctional sensing applications. *Chemical Engineering Journal*, *381*, 122778.

[96] Liu, H., Xiang, H., Wang, Y., Li, Z., Qian, L., Li, P., ... & Huang, W. (2019). A flexible multimodal sensor that detects strain, humidity, temperature, and pressure with carbon black and reduced graphene oxide hierarchical composite on paper. *ACS applied materials & interfaces*, *11*(43), 40613-40619.

## 2.2 Hydrogels

Hydrogels are defined as a 3D network of chemically or physically cross-linked polymers (occasionally, composed of an amphiphilic molecule) and an entrapped solvent (e.g. water) with high degree of flexibility due to large solvent content inside their polymeric mesh, which results in a macroscopic viscoelastic behavior. Hydrogels can retain large quantities of water or biological fluids. As for the mechanical properties, hydrogels are characterized by a soft rubbery texture similar to living tissues, making them an ideal substance for a variety of applications. Hydrogels with characteristic properties such as desired functionality, reversibility and biocompatibility can be tailored to suite a large variety of applications.[1] Limitations of hydrogel properties include low solubility, high crystallinity, non-biodegradability, undesired mechanical and thermal properties, unreacted monomers and the use of toxic cross-linkers for stability in water-saturated media. Therefore, it is of high importance to tailor these properties by copolymerization of a wide range of monomers with predefined properties like biodegradation, solubility, crystallinity and biological activities.[1]

### 2.2.1 Swelling behavior

Swelling, as in water retention inside the polymeric mesh, of hydrogels is a complex process consisting of a number of steps:[2]

1. The polar hydrophilic groups of the hydrogel interact with water, referred to as primary bound water.
2. The exposed hydrophobic groups also interact with water molecules, referred to as secondary bound water.
3. The osmotic force of the system, which leads to dilution is resisted by the physical or chemical crosslinks, so additional water is absorbed. Referred to as bulk water or free water, it fills the voids between the hydrogel chains.

The swelling magnitude of a hydrogel depends on the temperature and the interaction between water molecules and polymer chains, as explained by the Flory–Huggins theory.[3]

### 2.2.2 Classification

The classification of hydrogels depends on their physical properties, nature of swelling, method of preparation, origin, ionic charges, sources, rate of biodegradation and observed nature of crosslinking.[4] This results in a wide variety of hydrogel classes suitable for different applications. An overview of the classification criteria is depicted in **Figure 5**.

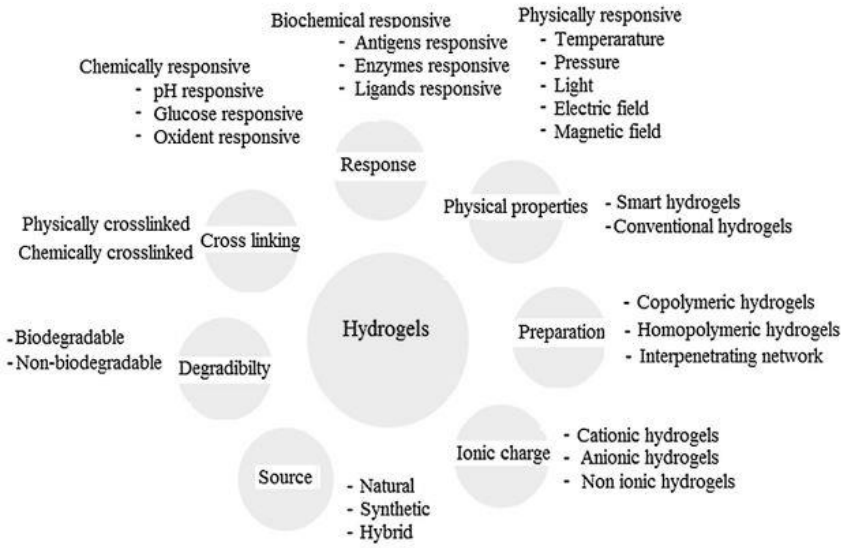


Figure 5. Different classes of hydrogels. Figure reproduced with permission from ref. [4]

### 2.2.3 Cross-linking

The cross-linking of a hydrogel limits its solubility in water, making it more stable. Here, hydrogels are classified as either physically or chemically cross-linked, both cross-linking types are depicted in **Figure 6**. Physically cross-linked hydrogels are obtained by hydrophobic association, chain aggregation, crystallization, polymer chain complexion and hydrogen bonding. Such hydrogels are reversible due to the conformational changes. Chemically cross-linked hydrogels are obtained by covalent bonding, which can be carried out during or post polymerization. Chemically cross-linked hydrogels are permanent and irreversible because of configurational changes. In physically cross-linked hydrogels, the presence of physical domain junctions, hydrogen bonding, hydrophobic interaction, ionic complexations allow ease of fabrication, reshaping, biodegradation and non-toxicity. Such advantages are not obtained

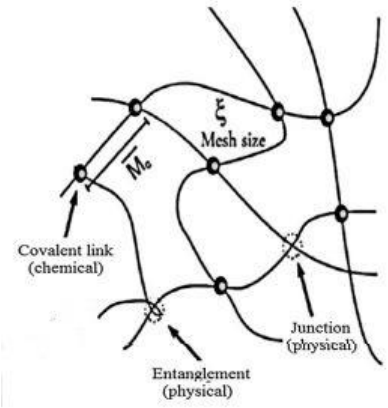


Figure 6. Concept of chemical and physical cross-linking within a hydrogel mesh. Figure adapted with permission from ref. [4]

from chemically cross-linked hydrogels. A combination of both cross-linking methods results in dual-network hydrogels.[1]

Several methods are employed to synthesize physically and chemically cross-linked hydrogels, such as:

1. Ionic interactions: Alginate is an example of a hydrogel that is cross-linked by ionic interactions. Alginate is a polysaccharide with mannuronic and glucuronic acid residues cross-linked by calcium ions.
2. Crystallization: aqueous solutions of Poly(vinyl alcohol) or PVA stored at room temperature form a hydrogel with weak mechanical performance. If the aqueous solution of PVA undergoes freezing cycles, highly elastic hydrogel is formed, with properties depending on the PVA molecular weight, the PVA concentration in water, the temperature and the time of freezing and the number of freezing cycles.
3. Physically cross-linked hydrogels are generally obtained from multi-block copolymers or graft copolymers.
4. Chemical reaction: hydrogels exhibit solubility due to the presence of functional groups such as OH, COOH and $NH_2$. Cross-linking by covalent bonds is achieved by the reactivity of such functional groups.
5. Radical polymerization: chemically cross-linked hydrogels can be obtained by the radical polymerization of hydrogels with polymerizable groups. Di(ethylene glycol) divinyl ether (DEGDVE) has been reported as a suitable cross-linker for p(NVCL).[5,6] The monomer has vinyl-groups on both ends, with bonds easily activated by free radicals. The outcome of the copolymerization process is a stable thermoresponsive polymer. The chemical structure of DEGDVE is shown in **Figure 7**.

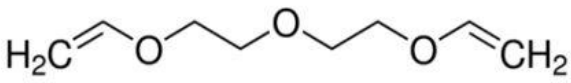


Figure 7. Chemical structure of DEGDVE monomer

### 2.2.4 Thermoresponsive hydrogels

Thermoresponsive hydrogels are defined by their ability to swell and deswell as a function of temperature fluctuations in the surrounding fluid. Such hydrogels can be classified as positive or negative temperature responsive.[1]

Positive temperature hydrogels are characterized by the upper critical solution temperature (UCST). Below the UCST, the hydrogel deswells and as a result releases water from its mesh,forming hydrogen bonds within the polymer network . Above the UCST, swelling occurs,

due to the breakdown of intramolecular hydrogen bonds and the formation of hydrogen bonds with water molecules. As a result, the hydrogel will rapidly swell above the UCST.[7]

Another class is referred to as negative temperature hydrogels, which is characterized by the low critical solution temperature (LCST). As a result, the hydrogel transitions from a swollen state (below LCST) to a deswollen state (above LCST). Therefore, the LCST is the most important parameter for negative temperature hydrogels that can be tailored using several approaches, such as mixing a small amount of ionic copolymer or changing the solvent composition. Additionally, the LCST of a hydrogel with more hydrophobic content drops. Below the LCST, water interacts with the hydrophilic part by forming hydrogen bonds. As the temperature increases above the LCST, the hydrophobic interactions within the hydrogel become stronger and the hydrogen bonds become weaker.[8,9] Poly(N-isopropylacrylamide) or p(NIPAAm) is one of the most studied and investigated thermoresponsive polymer, with a reported LCST of around 32°C, which lays between room temperature and body temperature.[10] Never the less, its acrylamide functional group is prone to hydrolysis in acidic conditions, which results in the release of toxic amide molecules.[11]

### 2.2.5 poly(N-vinylcaprolactam)

In the recent years, p(NVCL) has been reported as a biocompatible alternative to p(NIPAAm). P(NVCL) is an amphiphilic water-soluble thermoresponsive polymer with an LCST ranging from 31 to 34°C.[11] The LCST of p(NVCL) can be tailored, by increasing the polymer chain length, which lowers the LCST. This behavior is explained by its classical Flory-Huggins miscibility behavior.[5,12] By varying the polymer chain length, an LCST in the range of 16 to 40°C can be achieved. The LCST increases with the addition of hydrophilic monomers, and it decreases with hydrophobic monomers.[5,11,12]

The functionality of p(NVCL) is a result of the hydrophilic amide group and the hydrophobic aliphatic hydrocarbon chain. The cyclic structure of the caprolactam ring ensures the amphiphilic nature of p(NVCL) and its hydrolysis only results in the dissociation of the caprolactam ring with nontoxic volatile by-products.[12] The chemical structure of NVCL, p(NVCL) and p(NVCL-co-DEGDVE) is shown in **Figure 8**.

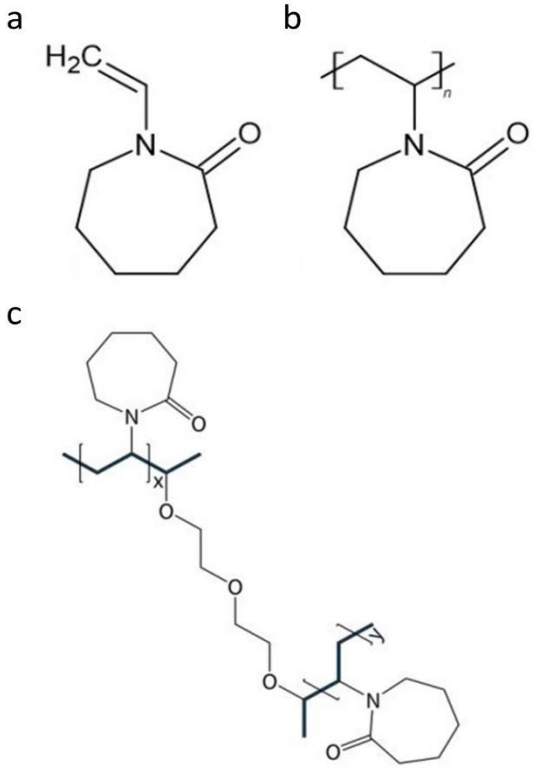


Figure 8. Chemical structure of a) NVCL monomer b) NVCL polymer c) NVCL-co-DEGDVE copolymer

## 2.2.6 Initiated Chemical vapor deposition (iCVD)

### 2.2.6.1 Fundamentals of iCVD

Initiated chemical vapor deposition (iCVD) is a vacuum-based thin film deposition technique, which involves chemical species (monomers and initiator) being delivered in the gas-phase. The initiator is subjected to elevated filament temperatures and as result decomposes to form radicals. The radicals adsorb onto the substrate surface to react with the monomer molecules, initiating film growth, as depicted in **Figure 9**. The reactor design promotes laminar flow of vapor-phase monomer/initiator molecules. A crucial parameter to monitor within iCVD process is the ratio of monomer's partial pressure $p_m$ to its saturation pressure $p_{sat}$. In general, $\frac{pm}{psat} <$ 0.7 is required to avoid condensation of the gases on different surfaces inside the iCVD deposition chamber.[13-15] Typical monomer materials include acrylates, styrenes, methacrylates and acrylamides (vinyl monomers). As for the initiator, peroxides (eg; tert-butyl peroxide or TBPO), dissociate at energies in the range of 100-170 kJ $mol^{-1}$, which translates to a filament temperature between 150 and 200°C.[16]

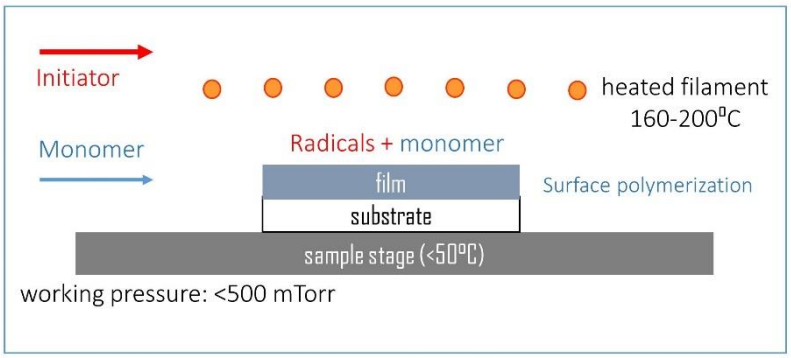


Figure 9. Description of film growth by iCVD

As described above, iCVD is a chain polymerization technique, where an initiator is used to provide active species to start the polymerization process. The reaction involves multiple steps:[16]

1. Initiation: which consists of two reactions, starting with initiator decomposition to form radicals.

   $I \rightarrow 2R\cdot$

   Followed by a reaction to produce chain-initiating radicals

   $R\cdot + M \rightarrow C_n\cdot$

2. Propagation: where growth by the repetitive addition of several monomer molecules to the chain-initiating radical molecule:

   $C_n\cdot + M \rightarrow C_{n+1}\cdot$

3. Termination: in this step, the radical is eradicated by another radical terminating polymer chain growth, with the two radicals Cn• and Cm• joining to form a macromolecular chain.

   $C_n\cdot + C_m\cdot \rightarrow P$

#### 2.2.6.2 Uniformity and conformality

In iCVD, due to the flow kinetics in the gas phase, monomers are able to diffuse into very small and complex geometries such as pores and trenches. It has been demonstrated that the sticking probability of radicals, defined by the sticking coefficient, is inversely proportional to the concentration of adsorbed monomer molecules.[17] Therefore, improved step coverage (uniformity and conformality) is obtained with low monomer $\frac{pm}{psat}$ , typically between 0.1 and 0.3. The step coverage *SC* is calculated from the sticking coefficient following **Equation 14**:

$$ln(SC) = -0.18 * \gamma * \left(\frac{H}{W}\right)^2 \qquad (14)$$

Where, $\gamma$ is the sticking coefficient, *H* is the trench height, *W* is the width of the trench initial opening.

### 2.2.7 References


[1] Ullah, F., Othman, M. B. H., Javed, F., Ahmad, Z., & Akil, H. M. (2015). Classification, processing and application of hydrogels: A review. In *Materials Science and Engineering C*, *57*, 414–433.

[2] Park, M. J., Hur, S. M., & Rhee, H. K. (2002). Online estimation and control of polymer quality in a copolymerization reactor. *AIChE journal*, *48*(5), 1013-1021.

[3] Flory, P. J., & Rehner Jr, J. (1943). Statistical mechanics of cross-linked polymer networks I. Rubberlike elasticity. *The journal of chemical physics*, *11*(11), 512-520.

[4] Qiu, Y., & Park, K. (2001). Environment-sensitive hydrogels for drug delivery. *Advanced drug delivery reviews*, *53*(3), 321-339.

[5] Muralter, F., Perrotta, A., Werzer, O., & Coclite, A. M. (2019). Interlink between tunable material properties and thermoresponsiveness of cross-linked poly (N-vinylcaprolactam) thin films deposited by initiated chemical vapor deposition. *Macromolecules*, *52*(18), 6817-6824.

[6] Muralter, F., Greco, F., & Coclite, A. M. (2019). Applicability of vapor-deposited thermoresponsive hydrogel thin films in ultrafast humidity sensors/actuators. *ACS applied polymer materials*, *2*(3), 1160-1168.

[7] Serra, L., Doménech, J., & Peppas, N. A. (2006). Drug transport mechanisms and release kinetics from molecularly designed poly (acrylic acid-g-ethylene glycol) hydrogels. *Biomaterials*, *27*(31), 5440-5451.

[8] Klouda, L. (2015). Thermoresponsive hydrogels in biomedical applications: A seven-year update. *European Journal of Pharmaceutics and Biopharmaceutics*, *97*, 338-349.

[9] Qiao, M., Chen, D., Ma, X., & Hu, H. (2006). Sustained release of bee venom peptide from biodegradable thermosensitive PLGA-PEG-PLGA triblock copolymer-based hydrogels in vitro. *Die Pharmazie-An International Journal of Pharmaceutical Sciences*, *61*(3), 199-202.

[10] Muralter, F., Perrotta, A., & Coclite, A. M. (2018). Thickness-dependent swelling behavior of vapor-deposited smart polymer thin films. *Macromolecules*, *51*(23), 9692-9699.

[11] Lee, B., Jiao, A., Yu, S., You, J. B., Kim, D. H., & Im, S. G. (2013). Initiated chemical vapor deposition of thermoresponsive poly (N-vinylcaprolactam) thin films for cell sheet engineering. *Acta biomaterialia*, *9*(8), 7691-7698.

[12] Kozanoğlu, S., Özdemir, T., & Usanmaz, A. (2011). Polymerization of N-vinylcaprolactam and characterization of poly (N-vinylcaprolactam). *Journal of Macromolecular Science, Part A*, *48*(6), 467-477.

[13] Baxamusa, S. H., Im, S. G., & Gleason, K. K. (2009). Initiated and oxidative chemical vapor deposition: a scalable method for conformal and functional polymer films on real substrates. *Physical Chemistry Chemical Physics*, *11*(26), 5227-5240.

[14] Coclite, A. M., Howden, R. M., Borrelli, D. C., Petruczok, C. D., Yang, R., Yagüe, J. L. & Gleason, K. K. (2013). 25th Anniversary article: CVD polymers: a new paradigm for surface modification and device fabrication. *Advanced Materials*, *25*(38), 5392-5423.

[15] Tenhaeff, W. E. & Gleason, K. K. (2008). Initiated and oxidative chemical vapor deposition of polymeric thin films: ICVD and oCVD. *Adv. Funct. Mater.* 18, 979–992.

[16] Odian, G. (2004). *Principles of polymerization*. John Wiley & Sons.

[17] Ozaydin-Ince, G., & Gleason, K. K. (2010). Tunable conformality of polymer coatings on high aspect ratio features. *Chemical Vapor Deposition*, *16*(1-3), 100-105.

## 2.3 Piezoelectric Zinc oxide

### 2.3.1 Optical and electrical properties

Zinc oxide (ZnO) has attracted attention due to its properties as well as synthesis routes. It is classified as an inorganic material and a direct bandgap semiconductor, with an energy band of 3.37 eV at 300 K. The optoelectronic properties of ZnO makes it suitable in green, blue-ultraviolet and white light-emitting devices. ZnO possess a large exciton binding energy of 60 meV, making it suitable for near-band-edge excitonic emissions.[1] Additionally, its electrical properties are of particular interest in the field of electronics. It is compliant to wet chemical etching, which eases its fabrication in electronics. Due to its transparency, it is applicable in fabrication of transparent thin-film transistors, with light insensitivity. The electrical properties of ZnO (commonly, an n-type semiconductor, doping with Al, Ga or In) are controlled by doping. Conductive doped-ZnO is used as transparent electrode material for displays and solar cells.[2]

As with most semiconductors in II-VI group, ZnO crystallizes into rocksalt, cubic zinc blende or hexagonal wurtzite structure, with the latter being the most thermodynamically stable at ambient conditions. ZnO with rocksalt structure is obtainable at high pressures, while zinc blende structure is a product of growth on cubic substrates.[2] **Figure 10** depicts the three crystal structures.

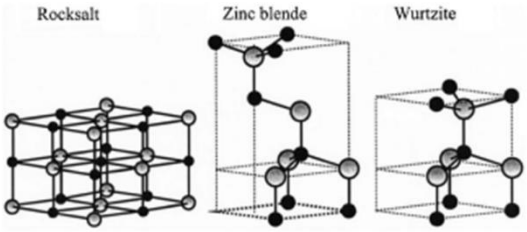


Figure 10. Different crystals of zinc oxide. Figure adapted with permission from ref. [2]

### 2.3.2 Mechanical properties

The mechanical properties of ZnO, as any other material, are conceptualized in the hardness *H*, elastic constants *C*, Young's *E*, shear *G* and bulk *B* moduli. For the ZnO wurtzite crystal structure, four out of five elastic constants are used to calculate the bulk modulus *B* using **Equation 14**:

$$B = \frac{(C_{11} + C_{12})C_{33} - 2C_{13}^2}{C_{11} + C_{12} + 2C_{33} + 4C_{13}} \qquad (14)$$

A wide range for the elastic constants for Wurtzite ZnO has been reported in literature, with $C_{11}$ = 157 – 246 GPa, $C_{12}$ = 82 – 127 GPA, $C_{13}$ = 64 – 118 GPa, $C_{33}$ = 83 – 270 GPa and $B$ = 134 – 183 GPa.[2] $E$ and $G$ are evaluated using **Equation 15** and **16**, respectively:

$$E = 3B(1 - 2v) \qquad (15)$$

And

$$G = \frac{E}{2(1 + v)} \qquad (16)$$

With the Poisson's ratio $v$ calculated from **Equation 17**:

$$v = \frac{C_{13}}{(C_{11} + C_{12})} \qquad (17)$$

For single crystalline ZnO investigated with nanoindentation technique, the reported $E$ = 111.2 ± 4.7 GPa and hardness $H$ = 5.0 ± 0.1 GPa. While for polycrystalline ZnO a wide range has been reported, with $E$ = 40 - 120 GPa and $H$ = 1.5 – 12 GPa.[2]

### 2.3.3 Piezoelectric properties

The piezoelectric polarization in ZnO crystals can be expressed following **Equation18**:

$$P_i = e_{ijk}\varepsilon_{jk} = d_{ijk}\sigma_{jk} \qquad (18)$$

Where $P_i$ is the electrical polarization, $e_{ijk}$ and $d_{ijk}$ are the piezoelectric strain and stress coefficients, respectively. While, $\varepsilon_{jk}$ and $\sigma_{jk}$ are the equivalent strain and stress. This relation defines the polarization related to the direct piezoelectric effect, while the indirect piezoelectric effect (strain because of applied electric field) is given in **Equation 19**:

$$\varepsilon_{ij} = d_{ijk}E_k \qquad (19)$$

With $E_k$ being the electric field. In the hexagonal wurtzite structure, the piezoelectric tensor has three coefficients, namely $d_{33}$, $d_{31}$ and $d_{15}$. The anisotropic piezoelectric polarization can be expressed following **Equation 20** or **21**:

$$\begin{pmatrix} P_{xx} \\ P_{yy} \\ P_{zz} \end{pmatrix} = \begin{pmatrix} 0 & 0 & 0 & 0 & e_{15} & 0 \\ 0 & 0 & 0 & e_{15} & 0 & 0 \\ e_{31} & e_{31} & e_{33} & 0 & 0 & 0 \end{pmatrix} \begin{pmatrix} \varepsilon_{xx} \\ \varepsilon_{yy} \\ \varepsilon_{zz} \\ \varepsilon_{xy} \\ \varepsilon_{yz} \\ \varepsilon_{zx} \end{pmatrix} \qquad (20)$$

Or

$$\begin{pmatrix} P_{xx} \\ P_{yy} \\ P_{zz} \end{pmatrix} = \begin{pmatrix} 0 & 0 & 0 & 0 & d_{15} & 0 \\ 0 & 0 & 0 & d_{15} & 0 & 0 \\ d_{31} & d_{31} & d_{33} & 0 & 0 & 0 \end{pmatrix} \begin{pmatrix} \sigma_{xx} \\ \sigma_{yy} \\ \sigma_{zz} \\ \sigma_{xy} \\ \sigma_{yz} \\ \sigma_{zx} \end{pmatrix} \qquad (21)$$

### 2.3.4 Bulk and thin film growth

Bulk growth of single crystalline ZnO is required in several optical applications. ZnO large single crystals tend to grow with (0001) preferential orientation on different substrates. However, a proper choice of the substrate will facilitate epitaxial growth, reducing in-plane and out-of-plane lattice mismatch. Homo-epitaxial growth on ZnO substrate eliminates thermal induced strain, lowers defect density and provides control over material polarity. High quality large single crystalline ZnO is grown using three main methods:[2]

1. Hydrothermal
2. Vapor phase
3. Melt growth

Due to the high vapor pressure of ZnO, vapor phase growth is hard to control, while melt growth is not easily achievable. Thus, hydrothermal growth is favorable.

ZnO thin films have been deposited with different techniques namely, sputtering and CVD processes. Poly crystalline or amorphous ZnO films are grown by sputtering from a high-purity ZnO target. With RF-magnetron sputtering, ZnO films have been deposited on different substrates such as, diamond, glass and Si. The deposition temperature ranged from room temperature up to 400°C and the ZnO thin films exhibited (001) preferential orientation. Single crystalline ZnO films were grown with RF-magnetron sputtering as demonstrated by Kim et al.

However, this was demonstrated on sapphire substrates with depositions carried out at elevated substrate temperature.[3]

Another technique employed for deposition of ZnO films is pulsed laser deposition (PLD, in which a stream of high-power laser pulses is used to evaporate material from targets, with the stoichiometry of the depositing material preserved. The process illustrated in **Figure 11**. In PLD, high-energy source particles are generated, allowing high quality film growth at low substrate temperature, ranging from 200 to 800°C. The properties of the grown ZnO films depend mainly on the substrate temperature, ambient oxygen pressure, and laser intensity. Sputter targets include cylindrical ZnO tablets made from pressed ZnO powder or single crystalline ZnO. A pure Zn metal source is less common.

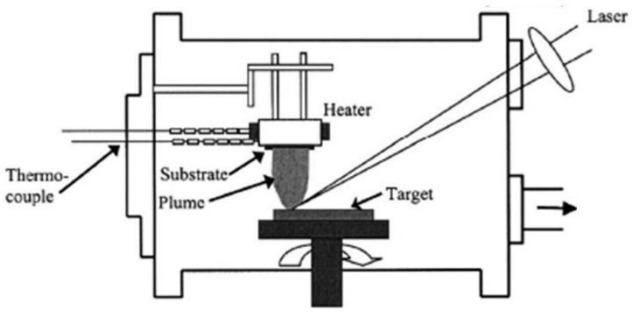


Figure 11. Description of PLD technique. Figure reproduced with permission from ref. [2]

Another technique of interest, to deposit ZnO films, is chemical vapor deposition (CVD). Here different modifications exist depending on the used precursor. In case of metal-organic precursors, the technique is called MOCVD. In the case of hydride or halide precursors, the technique is named hydride or halide CVD. In CVD, ZnO is deposited from vapor-phase precursors, which are transported by a carrier gas. The ZnO films deposited using this technique exhibit high crystalline, electrical, and luminescence properties. In MOCVD, metal alkyls are used, usually dimethyl zinc (DMZ) $Zn(CH_3)_2$ or diethyl zinc (DEZ) $Zn(C_2H_5)_2$ in combination with a separate source of oxygen and argon or nitrogen as a carrier gas.[2]

#### 2.3.4.1 Atomic layer deposition (ALD)

Atomic layer deposition (ALD) is a chemical vapor deposition method based on self-limiting, saturated surface reactions that produce highly conformal und uniform thin films with Angstrom level thickness control (defined by a parameter commonly named as growth per cycle or GPC). GPC is the thickness increase of the deposited film after one ALD cycle. Typically, the GPC is less than one monolayer due to effects such as steric hindrance, e.g. adsorbates block active

groups on the surface. Typically, one ALD cycle involves four steps as depicted in **Figure 12**, which are:[4]

1. Precursor adsorption
2. Purging step
3. Co-reactant exposure
4. Purging step

Self-limitation is another key parameter in ALD. Short precursor or reactant doses result in a decreased GPC as not enough reactant molecules are available to bind to all active surface groups. Contrarily, short purging times result in an increased GPC due to gas phase reactions. For a self-limiting ALD process, all four steps have to be in saturated regimes. The GPC varies with temperature due to effects resulting in CVD growth or effects leading to variation in the GPC while maintaining the self-limiting nature. At low temperatures, the precursor can condense on the surface. Additionally, low temperatures do not provide enough thermal energy to start the surface reactions. On the other hand, at high temperatures, the precursor can decompose and react without the co-reactant. These effects lead to a non-self-limiting ALD growth. At an intermediate temperature range, referred to as the ALD window, self-limiting ALD growth is obtained, however the GPC can still vary.[5]

Due to a change in the number of available reactive sites, the GPC is influenced by the number of growth cycles. In the first few cycles, deposition only occurs on the substrate surface. After a few cycles, both the surface of the substrate and the deposited film are available for adsorption. After full coverage of the substrate, the surface consists only of the deposited film. Due to these surface changes, the GPC changes in the initial stages and reaches a constant value after a number of cycles, which is referred to as the steady regime.[6]

The first precursors used for ALD growth of ZnO were zinc acetate (ZnAc) and $H_2O$, where the chemical reaction is:[7]

$$Zn(CH_3COO)_2 + H_2O \rightarrow ZnO + 2CH_3COOH$$

However, ZnAc requires a relatively high temperature to react with $H_2O$. There for, precursors that are more reactive have been developed for ALD of ZnO. Currently, the most common Zn precursor used in ALD is diethyl zinc (DEZ) which reacts readily with $H_2O$, where the chemical reaction is:

$$Zn(C_2H_5)_2 + H_2O \rightarrow ZnO + 2C_2H_6$$

The exothermic reaction of DEZ with $H_2O$ can be used to deposit ZnO thin films at temperatures much lower (100–200°C) than those needed for ZnAc. DMZ is also used as precursor with a reaction mechanism very similar to DEZ:

$Zn(CH_3)_2 + H_2O \rightarrow ZnO + 2CH_4$

DMZ can be used in the same deposition temperature range, however the limits of the ALD window, are reported to be slightly lower for DMZ.

In addition to $H_2O$, several other oxygen sources, such as $O_2$, $O_3$ and $N_2O$, have been used in ZnO depositions with DEZ or DMZ in conventional ALD processes, with similar growth rates compared to $H_2O$, however higher deposition temperatures are required. $O_2$ is commonly used in plasma-enhanced ALD (PEALD), which is employed to deposit films with a higher degree of stoichiometry at lower temperatures due to the higher reactivity of plasma.[7]

Similar to bulk ZnO, ALD ZnO crystallizes into a hexagonal wurtzite structure with high degree of crystallinity even at relatively low deposition temperatures. As previously stated, the structure of the films can be controlled by the deposition temperature. At deposition temperatures below 70°C, the films exhibit a strongly preferred (002) orientation. However, above 70°C, the (100) orientation dominates up to 160–200°C. At deposition temperatures above 220°C, the preferential orientation changes back to (002). Additionally, the deposition temperature affects the stoichiometry of the ZnO films, which in turn influences the electrical properties.[8] The n-type conductivity of ZnO is manly due to the defects and impurities in the ZnO crystal. Therefore, the electrical properties can be controlled by the amount of these defects and impurities. In ALD, this is controlled with the deposition temperature.[2]

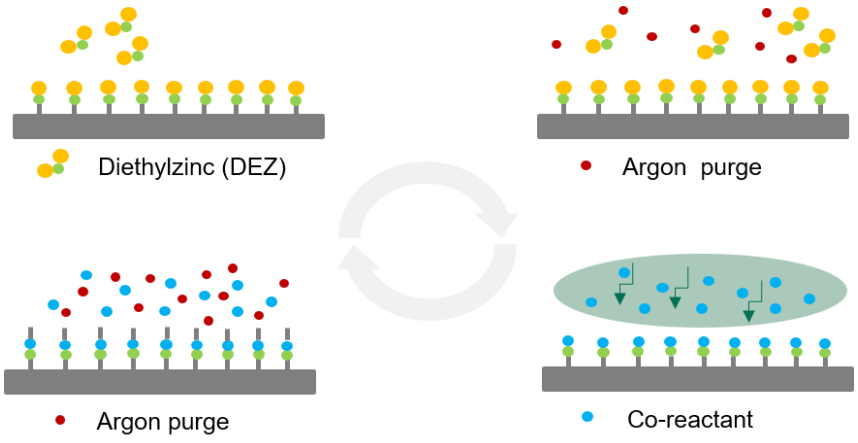


Figure 12. Four steps of an ALD cycle

### 2.3.4.2 Plasma-enhanced ALD

$O_2$ plasma, the typical co-reactant in PEALD, is much more reactive than $H_2O$, resulting in more stoichiometric films due to complete oxidation of Zn. This is translated to a decrease in oxygen vacancies and interstitial Zn, which reduces the n-type carrier concentration, resulting in films with higher resistivity. Additionally, the GPC greatly differs between the two processes. Significantly smaller ZnO crystallites are obtained from PEALD, which could contributes to the increasing the resistivity of the films. PEALD offers advantages over ALD:[9]

1. Reduced substrate temperature: less thermal energy is needed due to the high concentration of reactive species provided by the plasma. This is very handy when dealing with polymeric substrates with low thermal stability. However, substrate damage from plasma source is possible.
2. Improved material properties: as mentioned above, the use of plasma delivers films with less impurities, enhanced density and electronic properties.
3. Increased GPC and shorter purging times

The half-reactions of PE-ALD, applying DEZ and O2- plasma, can be written as:[10]

$OH + Zn(C_2H_5)_2 \rightarrow OZn(C_2H_5) + C_2H_6$

And

$OZn(C_2H_5) + 6O \rightarrow OZnOH + CO_2 + CO + 2H_2O$

Several reactor configurations are available for PEALD, with the plasma source and configuration being the main difference:[9]

1. Direct plasma: here the substrate is placed on the ground electrode, within the plasma region. The plasma is created between two parallel electrodes (capacitive coupling). The gases are usually introduced through a showerhead power electrode. Due to the high flux of radicals and ions, conformal and fast depositions are obtained. Direct plasma with mesh is another configuration of the direct plasma.

2. Remote plasma: here the plasma is created remotely. The plasma may however still be present above the substrate and the ion and electron density may be greater than zero. The main advantage of this configuration is the ability to tune the plasma and substrate conditions independently. The remote plasma can be generated inductively (through a dielectric tube and a coil), with a hollow cathode, or with microwave electron cyclotron resonance.

3. Radical-enhanced: in a radical-enhanced configuration, the plasma is placed relatively far away from the substrate. Through surface collisions on the way to the substrate, most ions and electrons are lost and only radicals arrive at the substrate. However, also the radical flux may be substantially reduced. The difference between remote and radical-enhanced configurations

is rather vague, and a configuration may be closer to one or the other. The general expression used for both configurations is remote plasma.

### 2.3.5 References


[1] Kołodziejczak-Radzimska, A., & Jesionowski, T. (2014). Zinc oxide—from synthesis to application: a review. *Materials*, *7*(4), 2833-2881.

[2] Özgür, Ü., Alivov, Y. I., Liu, C., Teke, A., Reshchikov, M., Doğan, S., ... & Morkoç, A. H. (2005). A comprehensive review of ZnO materials and devices. *Journal of applied physics*, *98*(4), 11.

[3] Kim, K. K., Song, J. H., Jung, H. J., Choi, W. K., Park, S. J., & Song, J. H. (2000). The grain size effects on the photoluminescence of ZnO/α-Al 2 O 3 grown by radio-frequency magnetron sputtering. *Journal of Applied Physics*, *87*(7), 3573-3575.

[4] Burgess, C. H. (2017). Review of tailoring ZnO for optoelectronics through atomic layer deposition experimental variables. *Materials Science and Technology*, *33*(7), 809-821.

[5] George, S. M. (2010). Atomic layer deposition: An overview. *Chemical Reviews*, *110*(1), 111–131.

[6] Puurunen, R. L. (2005). Surface chemistry of atomic layer deposition: A case study for the trimethylaluminum/water process. *Journal of Applied Physics,* 97,121301.

[7] King, D. M., Liang, X., Carney, C. S., Hakim, L. F., Li, P., & Weimer, A. W. (2008). Atomic layer deposition of UV-absorbing ZnO films on SiO2 and TiO2 nanoparticles using a fluidized bed reactor. *Advanced functional materials*, *18*(4), 607-615.

[8] Abu Ali, T., Pilz, J., Schäffner, P., Kratzer, M., Teichert, C., Stadlober, B., & Coclite, A. M. (2020). Piezoelectric Properties of Zinc Oxide Thin Films Grown by

Plasma-Enhanced Atomic Layer Deposition. *physica status solidi (a)*, *217*(21), 2000319.

[9] Profijt, H. B., Potts, S. E., Van de Sanden, M. C. M., & Kessels, W. M. M. (2011). Plasma-assisted atomic layer deposition: basics, opportunities, and challenges. *Journal of Vacuum Science & Technology A: Vacuum, Surfaces, and Films*, *29*(5), 050801.

[10] Pilz, J. Plasma-Enhanced Atomic Layer Deposition and Vapor Phase Infiltration of ZnO: From Fundamental Growth Characteristics to Piezoelectric Films. Ph.D. thesis, Graz University of Technology, 2020.

## 2.4 Nano imprint lithography (NIL)

Nanoimprint lithography is a micro/nanoscale fabrication technique with high resolution, low fabrication cost and high throughput. Structuring in NIL relies on mechanical deformations rather than electrons or photons (conventional in lithography processes), which achieves structures with higher resolution, as the diffraction limit (resolution limit in conventional lithography processes) is superseded. NIL is capable of sub-10 nm features fabrication with proper alignment of mask and substrate/resist as well as the choice of resist material, with viscoelastic properties being very important. Additionally, the substrate resist interface, resist stamp interface and the substrate stamp interface are defining factors.[1]

NIL is subcategorized into two main processes, which are:

1. Thermal-NIL or T-NIL
2. Ultraviolet-NIL or UV-NIL

According to **Figure 13**, T-NIL involves the following fabrications steps:[1]

1. Polymeric resist is applied as a thin film layer onto the substrate, typically using spin-coating
2. The stamp, with defined pattern, is brought into contact (pressure is applied) with the substrate/resin
3. The system is heated up above the glass transition temperature $T_g$ of the resin
4. After cooling down, stamp demolding is carried out
5. Optionally, etching is used to transfer the resist pattern into the underlying layer

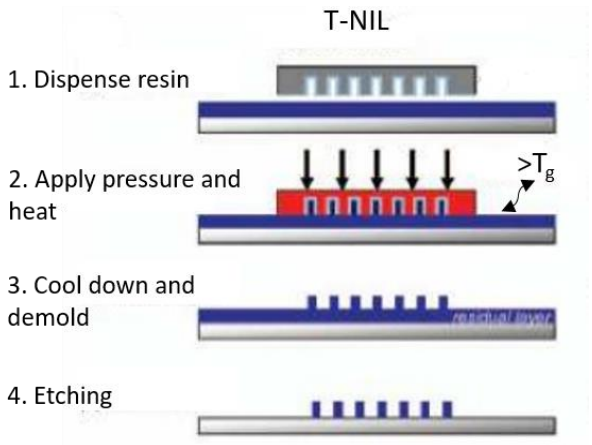


Figure 13. General fabrication steps involved in T-NIL

### 2.4.1 Ultraviolet-NIL

The main difference between UV-NIL and T-NIL is the resin choice, which is cured (hardened) by UV-light at room temperature. UV-NIL typically involves the following steps, which are depicted in **Figure 14**:

1. UV-curable resist is applied onto the substrate
2. Stamp, typically transparent, is brought into contact with the substrate/resin
3. UV light exposure through the transparent stamp, results in a cured resin
4. Demolding is performed and similar to T-NIL, subsequent etching is carried out for pattern transfer to underneath layers.

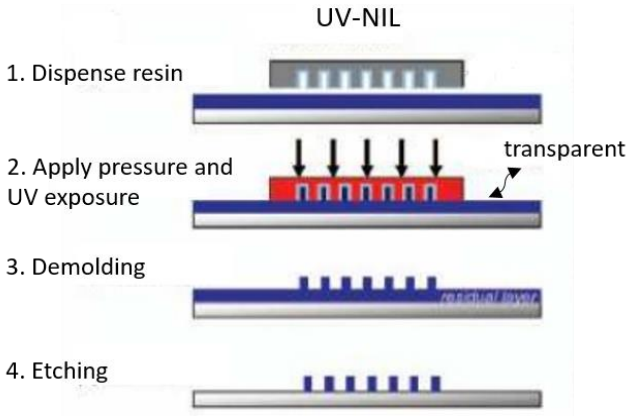


Figure 14. General fabrication steps involved in UV-NIL

Typically, UV-NIL processes limit the choice of resist material to UV-curable polymers. In comparison, T-NIL allows resist material versatility. Additionally, UV-exposure can only be performed by using a transparent stamp or/and substrate. However, due to the absence of high imprint contact pressure and thermal heating cycles, can be used in structuring large substrate areas (*d* = 30 cm).

The final thickness $h_f$ of the cured resin is calculated following the Navier-Stroke **Equation 22**:[2]

$$h_f = \left(\frac{2F}{\mu a^2 LV} + \frac{1}{h_0^2}\right)^{-\frac{1}{2}} \qquad (22)$$

Where, *F* is the force applied, $\mu$ is the dynamic viscosity, *a* is the contacting length, *L* is the width of the panel, *V* is the web speed and $h_0$ is the initial thickness.

The time *t* needed to reach the final thickness $h_f$ is calculated following **Equation 23**:

$$t = \frac{\mu a^2}{2P}\left(\frac{1}{h_f^2} - \frac{1}{h_0^2}\right) = \frac{\mu a^3 L}{2F}\left(\frac{1}{h_f^2} - \frac{1}{h_0^2}\right) \qquad (23)$$

Based on the stamp material, UV-NIL can be categorized into hard or soft UV-NIL. In hard UV-NIL, the demolding force after curing is very high. Moreover, due to the waviness and roughness of the substrate and the stamp, parallel and uniform contact is hard to maintain, especially for large imprint areas. These drawbacks can be reduced with soft UV-NIL.

The reproducibility or pattern transfer effectiveness from the stamp to the resin can be described thermodynamically following **Equation 24**:[3]

$$\varepsilon \approx \frac{\gamma_{sr}}{E_{stamp}\, x\, R_0} \qquad (24)$$

Where, $\varepsilon$ is the maximum inaccuracy, $E_{stamp}$ is the Young's modulus of the stamp, $\gamma_{sr}$ is the solid-resin interfacial energy and $R_0$ is the radius and/or height of the structures. To imprint high-resolution structures with good fidelity, $\boldsymbol{\varepsilon} < 0.1$ is required. This translates to increased *E* of the stamp and a reduced $\gamma_{sr}$, which results in higher replication accuracy for features with small $R_0$. Additionally, reducing the demolding force needed to separate stamp from the cured resin, minimizes the mechanical stresses that can damage the transferred pattern. A lower force during the demolding process reduces the $\gamma_{sr}$, between stamp and the cured resin, following **Equation 25**:

$$\gamma_{sr} = \gamma_s + \gamma_r - 2(\gamma_s\, x\, \gamma_r)^{\frac{1}{2}} \qquad (25)$$

Proper demolding is essential for defect-free imprints and could be achieved with lower stamp resin adhesion energy $W_A$, which is given in **Equation 26**:

$$W_A = 2(\gamma_s\, x\, \gamma_r)^{\frac{1}{2}} \qquad (26)$$

Thus, $\gamma_s$ and $\gamma_r$ should be minimized and equal in magnitude ($\gamma_s \sim \gamma_r$).

### 2.4.2 Residual free imprint

The interfacial energy is a dominant factor in residue-free imprinting. The interaction between the surface energies of the stamp, the substrate and the resin, which is described by the spreading parameter during nanoimprinting $S_{NIL}$, is given in **Equation 27**:[3]

$$S_{NIL} = \gamma_{substrate/stamp} - \gamma_{\frac{substrate}{resin}} - \gamma_{\frac{stamp}{resin}} \qquad (27)$$

For $S_{NIL} < 0$, stamp induced dewetting is observed.

During the coating step, the substrate wetting by the resist, which is described by a positive spreading parameter $S_{coat}$ is given in **Equation 28**:

$$S_{coat} = \gamma_{substrate/air} - \gamma_{\frac{substrate}{resin}} - \gamma_{\frac{air}{resin}} \qquad (28)$$

Here, complete wetting of substrate surface is desired and is applicable in case $S_{coat} \geq 0$, which is achieved with a lower $\gamma_{substrate/resin}$. Last, a resin with low viscosity improves residual-free-layer imprinting due to improved dewetting. The dewetting velocity $V$ is given in **Equation 29**:

$$V = \frac{1}{\eta}\, x\, \frac{{S_{NIL}}^2}{E\, x\, h} \qquad (29)$$

Where $\eta$ is the resin viscosity, $E$ is the stamp Young's modulus and $h$ is the film thickness.

### 2.4.3 References

[1] Lan, H., & Ding, Y. (2010). *Nanoimprint lithography* (pp. 457-494). Croatia: InTech.

[2] Ahn, S. H., & Guo, L. J. (2009). Large-area roll-to-roll and roll-to-plate nanoimprint lithography: a step toward high-throughput application of continuous nanoimprinting. *ACS nano*, *3*(8), 2304-2310.

[3] Leitgeb, M., Nees, D., Ruttloff, S., Palfinger, U., Götz, J., Liska, R. & Stadlober, B. (2016). Multilength scale patterning of functional layers by roll-to-roll ultraviolet-light-assisted nanoimprint lithography. *ACS nano*, *10*(5), 4926-4941.

## 2.5 Finite element method simulation

### 2.5.1 COMSOL Multiphysics

COMSOL Multiphysics is a finite element analysis (FEA)/ finite element method (FEM) simulation package that provides single-physics and coupled multiphysics modeling. The modeling workflow involves defining the geometry, material properties and physics with a wide range of possible operating conditions and physical effects considered. Modeling with COMSOL Multiphysics allows switching and combining different physical phenomena such as electromagnetics, structural mechanics, acoustics, fluid flow, heat transfer and chemical reactions.

The modeling workflow encompasses:

- Define geometry
- Define materials and respective properties
- Define respective physics (single or multi)
- Meshing
- Studies and optimization
- Visualization and post processing

#### 2.5.1.1 Structural mechanics module

The structural mechanics module is an FEA package for the analysis of mechanical behavior of solid structures. The module delivers a wide range of modeling tools and functionalities for solid mechanics, dynamics and vibrations, materials modeling, shells, beams, contact and fractures. In addition to modeling of 3D structures, 2D structures are modelled (plane stress, plane strain, generalized plane strain, and axial symmetry). The Structural Mechanics Module can be combined with a wide range of other COMSOL modules to model thermal stress, fluid–structure interaction, and piezoelectricity. Analysis types provided within the module include:[1]

- Static
- Eigenfrequency
- Undamped
- Damped
- Prestressed
- Transient
- Direct or mode superposition
- Frequency response

- Direct or mode superposition
- Geometric nonlinearity and large deformations
- Mechanical contact
- Buckling
- Response spectrum
- Random vibration
- Component mode synthesis

Additionally, there are different material models within the module, which include:

• Linear elastic materials: can be isotropic, orthotropic or anisotropic

• Linear viscoelastic materials

• Piezoelectric material

• Magnetostrictive materials

• Nonlinear structural materials

#### 2.5.1.1.1 Linear elastic material

For isotropic linear elastic materials, Hooke's law relates the stress tensor $\sigma$ to the strain tensor as given in **Equation 30**:

$$\sigma = \sigma_{ex} + C\ x\ \varepsilon_{el} = \sigma_{ex} + C\ x\ (\varepsilon - \varepsilon_{inel}) \qquad (30)$$

Where C is the elasticity tensor, $\varepsilon_{el}$ is the elastic strain (difference between total strain $\varepsilon$ and inelastic strain $\varepsilon_{inel}$) and $\sigma_{ex}$ is the extra stress defined as initial and viscoelastic stress. With the inelastic strain calculated from **Equation 31**:

$$\varepsilon_{inel} = \varepsilon_0 + \varepsilon_{ext} + \varepsilon_{th} + \varepsilon_{hs} + \varepsilon_{pl} + \varepsilon_{cr} + \varepsilon_{ve} \qquad (31)$$

Where $\varepsilon_0$ is the initial strain, $\varepsilon_{ext}$ is the external strain, $\varepsilon_{th}$ is the thermal strain, $\varepsilon_{hs}$ is the hygroscopic strain, $\varepsilon_{pl}$ is the plastic strain, $\varepsilon_{cr}$ is the creep strain and $\varepsilon_{ve}$ is the viscoplastic strain. The hygroscopic strain is calculated following **Equation 32**:

$$\varepsilon_{hs} = \beta_{hs}\, x\, C_{moi} \qquad (32)$$

Where $\beta_{hs}$ is the hygroscopic swelling coefficient and $C_{moi}$ is the concentration of moisture. The elastic strain energy density $W_s$ is given following **Equation 33**:

$$W_s = \frac{1}{2}\varepsilon_{el}\, x\, (C\, x\, \varepsilon_{el} + 2\sigma_0) = \frac{1}{2}\varepsilon_{el}\, x\, (\sigma + \sigma_0) \qquad (33)$$

The stress and strain tensors are generally defined by a 3x3 matrix as given in **Equation 34**:

$$\begin{bmatrix} \sigma_{xx} & \sigma_{xy} & \sigma_{xz} \\ \sigma_{xy} & \sigma_{yy} & \sigma_{yz} \\ \sigma_{xz} & \sigma_{yz} & \sigma_{zz} \end{bmatrix} and \begin{bmatrix} \varepsilon_{xx} & \varepsilon_{xy} & \varepsilon_{xz} \\ \varepsilon_{xy} & \varepsilon_{yy} & \varepsilon_{yz} \\ \varepsilon_{xz} & \varepsilon_{yz} & \varepsilon_{zz} \end{bmatrix} \qquad (34)$$

Due to the isotropic material symmetry, the elasticity matrix *C* is given in **Equation 35**:

$$C = \frac{E}{(1+v)(1-2v)} \begin{bmatrix} 1-v & v & v & & 0 & 0 & 0 \\ v & 1-v & v & & 0 & 0 & 0 \\ v & v & 1-v & & 0 & 0 & 0 \\ & & & \frac{1-2v}{v} & 0 & 0 & \\ 0 & 0 & 0 & & \frac{1-2v}{v} & 0 & \\ 0 & 0 & 0 & 0 & & & \\ & & & & 0 & \frac{1-2v}{v} & \end{bmatrix} \qquad (35)$$

#### 2.5.1.1.2 Piezoelectric material

Modelling of piezoelectric materials within the structural mechanics module relies on the piezoelectric coupling equations. The stress-charge form of the coupling equations is given in **Equation 36** and **37**:

$$\sigma = C_E \varepsilon + e^T E \qquad (36)$$

And

$$D = e\varepsilon + \varepsilon_0 \varepsilon_r E \qquad (37)$$

Where, $\sigma$ is the stress, $C_E$ is the elasticity matrix, $\varepsilon$ is the strain, $e^T$ is the coupling matrix, *E* is the electric field, *D* is electric field displacement, $\varepsilon_0$ is the vacuum permittivity and $\varepsilon_r$ is the relative permittivity. While, the strain-charge form is given in **Equation 38** and **39**:

$$\varepsilon = S_E \sigma + d^T E \qquad (38)$$

And

$$D = d\sigma + \varepsilon_0 \varepsilon_{r\sigma} E \qquad (39)$$

Where, $S_E$ and $d^T$ are the material compliance and coupling matrices. Transformation from strain-charge to stress-charge follows **Equation 40**, **41** and **42**:

$$C_E = S_E^{-1} \qquad (40)$$

$$e = d\, S_E^{-1} \qquad (41)$$

And

$$\varepsilon_\varepsilon = \varepsilon_0 \varepsilon_{r\varepsilon} - d\, S_E^{-1} d^T \qquad (42)$$

#### 2.5.1.2 AC/DC module

The AC/DC module provides you with a wide range of modeling features and numerical methods for investigating electromagnetic and electrostatic fields by solving Maxwell's equations. In combination with the structural mechanics module, the piezoelectric multiphysics coupling is used to model the behavior of piezoelectric-based devices.[2]

The charge conservation equation of electrostatics follows Gauss' law and is given in **Equation 43**:

$$\nabla . D = \rho_v \qquad (43)$$

Where, ∇ is the curl, *D* is the electric field displacement, $\rho_v$ is the volume electric charge density.

While, the electric field *E* is derived from the electric potential *V* following **Equation 44**:

$$E = -\nabla V \qquad (44)$$

The current density is calculated from **Equation 45**, referred to as the equation of continuity:

$$\nabla . J = -\frac{\partial p}{\partial t} \qquad (45)$$

Where, *J* is the current density, $p$ is the electric charge density and *t* is time. For linear materials, the polarization *P* is directly proportional to the electric field *E,* the vacuum permittivity $\varepsilon_0$ and the electric susceptibility $X_e$, as given in **Equation 46**:

$$P = \varepsilon_0 X_e E \qquad (46)$$

And the electric field displacement *D* is calculated from **Equation 47**:

$$D = \varepsilon_0 (1 + X_e) E \qquad (47)$$

### 2.5.2 References


[1] COMSOL Multiphysics. (2018). Structural mechanics module.

[2] COMSOL Multiphysics (2018). AC/DC module.

# 3
# Scientific Publications

In this chapter, the experimental work conducted to realize this thesis is presented in the form of peer-reviewed articles.

## 3.1 Piezoelectric Properties of Zinc Oxide Thin Films Grown by Plasma-Enhanced Atomic Layer Deposition


Original Paper | Open Access

**Piezoelectric Properties of Zinc Oxide Thin Films Grown by Plasma-Enhanced Atomic Layer Deposition**

Taher Abu Ali, Julian Pilz, Philipp Schäffner, Markus Kratzer, Christian Teichert, Barbara Stadlober
... See all authors

First published: 26 August 2020 | https://doi.org/10.1002/pssa.202000319 |

Reference: Abu Ali, T., Pilz, J., Schäffner, P., Kratzer, M., Teichert, C., Stadlober, B., & Coclite, A. M. (2020). Piezoelectric Properties of Zinc Oxide Thin Films Grown by Plasma-Enhanced Atomic Layer Deposition. Physica Status Solidi (A) Applications and Materials Science, 217(21). https://doi.org/10.1002/pssa.202000319

### 3.1.1 Preface

The work presented in this publication was conducted at Graz University of Technology in cooperation with Joanneum Research and University of Leoben. Taher Abu Ali and Julian Pilz performed sample preparation, measurements and manuscript preparation. Markus Kratzer performed the PFM measurements. Philipp Schäffner helped with data evaluation and interpretation. The work was supervised by Christian Teichert, Barbara Stadlober and Anna Maria Coclite. The published article is reproduced with permission from the publisher.

### 3.1.2 Introduction

Zinc oxide (ZnO) has attracted a lot of interest in material research due to its wide band gap energy (3.37 eV),[1] high excitonic binding energy (60 mV)[2] and relatively high piezoelectric coefficients ($d_{33}$= 11.67 $pCN^{-1}$ and $d_{31}$= -5.43 $pCN^{-1}$, for bulk ZnO).[3] Such properties, associated with its wurtzite structure, make ZnO of particular interest in many applications which include electronics (transparent electrodes and transparent thin film transistors),[1,4] optoelectronics (laser diodes and solar cells),[2,5] sensors (chemical, piezoelectric and pyroelectric),[6,7] transducers (surface acoustic wave devices),[8] and energy harvesting.[9] Additionally, ZnO is an n-type semiconductor, where its semiconducting properties are tuned by doping, annealing, and most importantly by the growth process and related process parameters. Therefore, several techniques have been implemented to synthesize ZnO bulk crystals or films and to tailor their properties for different applications.[10] Of particular interest is atomic layer deposition (ALD).[10] It allows the deposition of uniform and conformal ZnO thin films with Å-level precision.[11,12] Uniformity and conformality are products of self-limiting layer-by-layer film growth from vapor phase precursors, with each precursor dosing step being separated by a purging step. Common ALD processes include thermal ALD and plasma-enhanced ALD (PE-ALD). PE-ALD allows for the deposition of high-quality films at lower substrate temperature compared to thermal ALD as the surface reactions are driven by energetic plasma species rather than thermal energy.[13] Such low deposition temperatures are suitable for ZnO growth on flexible substrates such as polymers, while maintaining control over films' optical, electrical, and mechanical properties.[14,15]

Similarly, the piezoelectric properties of ZnO films are influenced by the deposition technique and the growth parameters. **Table 1** shows the piezoelectric coefficient $d_{33}$ of ZnO films prepared by several deposition techniques as reported in literature.

Table 1. Reported piezoelectric coefficient $d_{33}$ of ZnO films

| Technique | Film thickness [nm] | $d_{33}$ [$pmV^{-1}$] |
|---|---|---|
| PLD | 200 | 12[16] |
| PLD | 50 | 25[17] |
| PLD | 800 | 49.7[18] |
| RF magnetron sputtering | 285 | 5[19] |
| RF magnetron sputtering | 710 | 5.3[19] |
| RF magnetron sputtering | 1400 | 8[19] |
| DC sputtering | 210 | 110[20] |

The investigation of the piezoelectric properties in these studies were performed by piezo response force microscopy (PFM), which measures the indirect piezoelectric effect, i.e., the reported values result from a local microscopic effect.[21-23] Macroscopic piezoelectric properties can be measured with a stamp setup, which excites the piezoelectric material mechanically and measures the direct piezoelectric effect.

While the piezoelectric characterization has been reported for ZnO films grown by different techniques, literature on piezoelectric properties of ZnO films prepared by ALD is very limited.[24] Nevertheless, ZnO deposited by ALD and especially PE-ALD has shown ideal properties for piezoelectric applications such as polycrystallinity with (002) texture,[15,25,26] high resistivity,[15,25] and low amount of impurities.[14,25,27,28] Furthermore, the high reactivity of the plasma co-reactant allows for the deposition on thermo-sensitive substrates at substrate temperatures as low as room temperature.[14,15] This study therefore focuses on the piezoelectric properties of ZnO thin films grown on flexible PET and rigid glass substrates at different substrate temperatures.

### 3.1.3 Results

Since the crystallographic properties have a large effect on the piezoelectric coefficients,[29,30] X-ray diffraction was performed. The XRD spectra of ZnO thin films grown on ITO-PET and on glass at different substrate temperatures are shown in **Figure 15a** and **15b**, respectively. The spectra are shown in a 2θ range in which peaks corresponding to the ZnO wurtzite structure were observed. For all the measured spectra in Figure 15a, a decaying background can be observed, which can be associated with the amorphous PET substrate. The ZnO samples show a polycrystalline pattern with diffraction peaks which can be associated with the (100) and (002) crystallographic orientation of the ZnO wurtzite structure. By increasing the substrate temperature, the preferential orientation of the films switches from (100) to (002). By further increase of the substrate temperature beyond 150°C, the contribution from the (100) orientation further diminishes. Furthermore, the (002) peak position shifts to higher angles with increased substrate temperature, mainly for the samples deposited on ITO-PET, which could be explained by decreased microstrain within the sample. As the c-axis is the polar axis in the hexagonal wurtzite structure, a strong (002) preferential orientation of the crystallites is desired to enhance the measured piezoelectric current.[14,15,19,31-32]

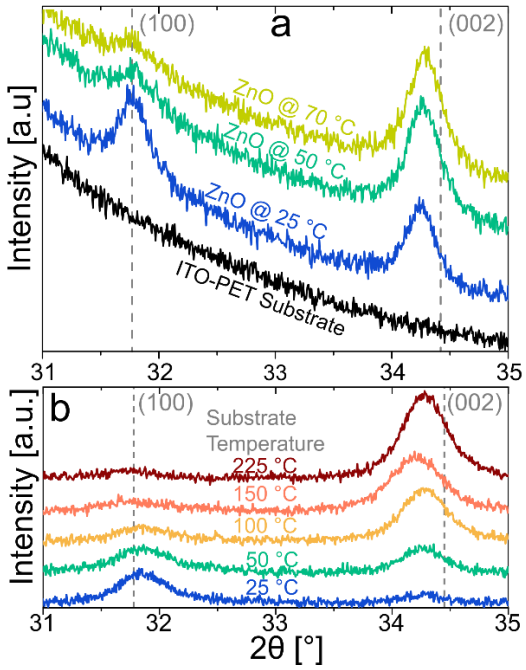


Figure 15. XRD patterns of ZnO films grown a) on PET and b) on glass at different substrate temperatures. Vertical, dashed lines show the peak positions of a ZnO powder reference (ICSD-26170) [33]

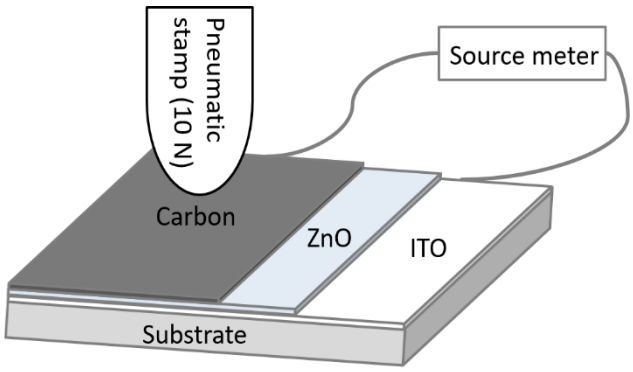


Figure 16. Schematic diagram of device architecture and piezoelectric measurement setup. Image not to scale, the area of the tip is 0.8 $cm^2$ and the sample size is 1.5 $cm^2$

The piezoelectric current signal *I* was measured as a function of time *t* upon periodic force cycles applied to the ZnO thin films by means of the setup shown in **Figure 16**. **Figure 17** shows the characteristic output plots for the films deposited at 25°C a) on ITO coated PET substrate and b) on ITO coated glass substrate. Positive current pulses are generated upon pressing onto the sample and negative current pulses upon releasing the stamp from the sample. For such films, the average positive piezoelectric peak current generated from one cycle was 1.8 ± 0.1 nA when deposited on PET and 0.3 ± 0.1 nA when deposited on glass. When the films deposited on ITO-PET were mechanically excited, a recoil current was detected upon pressing and releasing, due to the elasticity of the substrate.[34] The piezoelectric charge *Q* was calculated by integrating the piezoelectric current over time, as shown in **Equation 48**.

$$Q = \int I \, dt \tag{48}$$

**Figure 17c** shows the calculated piezoelectric charge *Q*, for ZnO thin films deposited on both flexible PET and rigid glass substrates at different substrate temperatures *T*, respectively. A linear increase of the piezoelectric charge for films on both substrates was observed. For ZnO on PET, increasing the substrate temperature to 50 °C resulted in a piezoelectric peak current of *I*= 3.6 $\pm$ 0.1 nA, corresponding to a charge of *Q* = 180 $\pm$ 10 pC. Further increase of the substrate temperature to 70 °C resulted in a piezoelectric peak current of *I* = 5.8 $\pm$ 0.1 nA and *Q* = 320 $\pm$ 10 pC. The increasing linear trend, attributed to the enhancement of the (002) orientation with increased temperature, was measured also for the samples deposited on glass: in this case, at 50°C, the generated piezoelectric peak current was *I* = 1.4 $\pm$ 0.2 nA and *Q* = 65$\pm$8 pC. Reaching a maximum of 4.3 $\pm$ 0.2 nA (*Q* = 190 $\pm$ 10 pC) for samples deposited at 225°C.

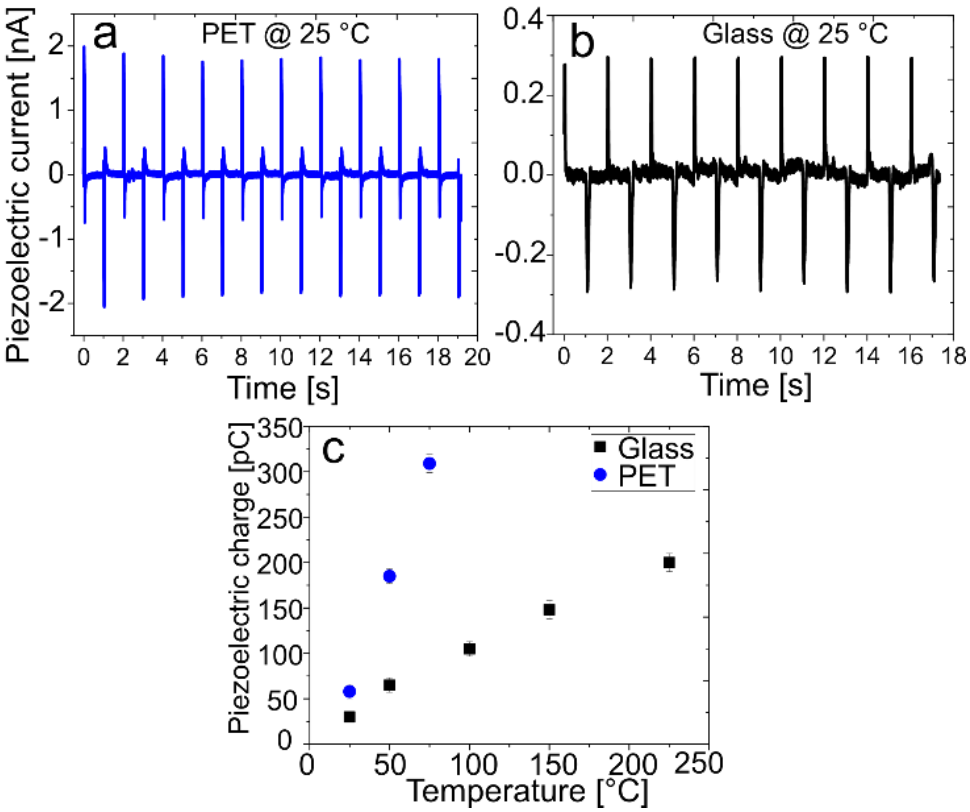


Figure 17. Piezoelectric current signal vs. time for 9-10 step force cycles applied to ZnO thin film deposited at 25°C a) on ITO coated PET b) on ITO coated glass. c) Generated piezoelectric charge as a function of the substrate deposition temperature for films grown on PET and glass

Piezoelectric current/charge generated from ZnO thin films deposited on rigid glass substrates were lower compared to those generated by ZnO thin films on flexible PET substrates, due to bending effects of the substrate.[35] Bending of PET substrates generates charges through the transverse piezoelectric effect (attributed to the $d_{31}$ coefficient), which results in higher measured piezoelectric current/charge.[36] However, ZnO films deposited on rigid glass substrates are not prone to bending, resulting in lower generated piezoelectric current/charge.

As the response of ZnO films deposited on glass is not expected to have $d_{31}$ contributions, the piezoelectric coefficient $d_{33}$ can be calculated by

$$d_{33} = Q/F \tag{49}$$

where $Q$ is the piezoelectric charge and $F$ is the excitation force. The calculated $d_{33}$ coefficients are shown in **Table 2** below.

Table 2. Calculated piezoelectric coefficient for ZnO films deposited on glass substrates at different temperatures

| Deposition temperature [°C] | $d_{33}$ [pC $N^{-1}$] |
|---|---|
| 25 | 3.0 |
| 50 | 6.5 |
| 100 | 10.5 |
| 150 | 14.8 |
| 225 | 20.0 |

The calculated piezoelectric coefficient ranges between 3.0 pC $N^{-1}$ and 20.0 pC $N^{-1}$, for ZnO films grown within the temperature range of 25°C and 225°C. The $d_{33}$ values are comparable to those reported in Table 1.

The results obtained from our in-house built piezoelectric setup allows macroscopic piezoelectric characterization of ZnO thin films. However, microscopic characterization using PFM, gives information about the local piezoelectric properties at a nanometer scale. **Figure 18a** shows the topography of ZnO film deposited at 25°C, which is characterized by small grains < 30 nm. The phase response (**Figure 18b**) does not show a coherent orientation of the grain polarization. However, large areas are recognizable, where the piezoelectric phase is ca. 180°. The piezo response (PR) amplitude (**Figure 18c**) is relatively low, with a maximum displacement of 20 pm. The incoherence of the phase response and the low amplitude can be explained by the crystallographic properties of the film, i.e. where the wurtzite ZnO structure is mostly oriented along the (100) axis. Figure 3d shows the topography of ZnO film deposited at 225°C, which is characterized by a granular topography with grain diameter of ~60 nm. The PR amplitude signal (**Figure 18f**) follows the grain structure, where regions with higher piezoelectric displacement are mostly located within the grains, while at the grain boundaries, the displacement is lower. This could be attributed to the fact that the grain boundaries are crystallographic defects. From the PFM phase image (**Figure 18e**), a certain degree of phase shift is recognizable. The grains seem to be in-phase with the external AC driving voltage, while boundaries seem to be mostly out-of-phase. Considering that the wurtzite ZnO structure in this film is mostly oriented along the (002) axis, the PFM phase can be related with the grain polarization, being this in-phase, it corresponds to a Zn-terminating surface.

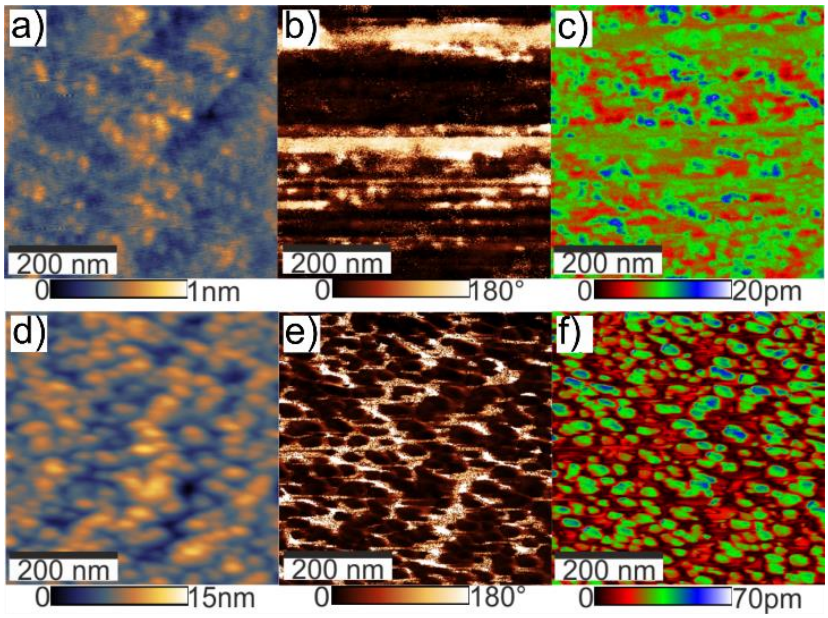


Figure 18. a) topography b) PR phase and c) PR Amplitude of ZnO at 25°C, d) topography e) PR phase and f) PR amplitude of ZnO at 225°C. Both films were grown on Si substrates

### 3.1.4 Conclusion

Piezoelectricity in ZnO thin films deposited on flexible PET substrates as well as on rigid glass substrates by PE-ALD at different substrate temperatures was investigated. For this purpose, the piezoelectric current/charge was macroscopically measured and evaluated with an in-house built piezoelectric measurement setup, applying a periodic step force signal of 10 N. ZnO films grown on flexible substrates showed increased piezoelectric output (up to 320 pC) compared to films grown on rigid substrates, possibly due to contributing bending effects upon force application. Furthermore, films showed increased piezoelectric output with increasing substrate temperature for both substrates, which can be related to an enhanced orientation of the crystallites along the polar (002) crystallographic axis. This is confirmed by PFM measurements, which indicate a predominant polarization orientation in the film.

### 3.1.5 Experimental

ZnO thin films were grown by PE-ALD in an in-house-built direct plasma reactor. Details on the setup can be found elsewhere.[14,15] One cycle of the process consisted of 0.15 s diethylzinc (DEZ) dose, 22 s Argon (Ar) purge, 8 s $O_2$-plasma (60 W power), and 15 s Ar purge. ZnO films were deposited on Si (100) wafers with native oxide (Siegert Wafer, cut to approx. 2 x 2 cm) for spectroscopic ellipsometry and piezoresponse force microscopy measurements and on PET coated with Indium Tin oxide (ITO; 60 Ω/sq surface resistivity) substrates (Sigma-Aldrich, Germany), as well as glass slides and glass coated with ITO (60 Ω/sq surface resistivity)

substrates (Sigma-Aldrich, Germany) for crystallographic and macroscopic piezoelectric characterization. Depositions on ITO coated PET substrates were performed at substrate temperatures of 25°C, 50°C and 70°C. Due to the temperature dependent growth per cycle of the ALD process,[14] the number of cycles was adapted for each deposition series to reach a thickness of around 65 nm. Depositions on ITO coated glass substrates were performed at 25°C, 50°C, 100°C, 150°C, and 225°C with resultant film thicknesses of around 50 nm.

Spectroscopic ellipsometry (SE, J.A. Woollam M-2000V) was performed on films grown on Si substrates to determine the thickness and optical constants of the films. Measurements were carried out in a wavelength range of 370–1000 nm at three different angles (65°, 70°, and 75°). Using a Cauchy model in the transparent region of the ZnO films (450–1000 nm), the thickness and refractive index of the films were extracted.

X-ray diffraction (XRD) in a θ/θ-configuration (Panalytical Empyrean) was performed to analyze the specular crystal orientation of films grown on ITO/PET substrates as well as films grown on glass substrates. A 1/8° divergence slit, a 4 mm mask, and a P7.5 antiscatter slit were used in the setup, and the detector was operated in 1D-mode.

The macroscopic piezoelectric properties were measured in an in-house-built piezoelectric measurement setup. For this evaluation, conductive carbon tape (Science Services GmbH) was applied on the ZnO film, as a top electrode. The setup consisted of a pneumatic stamp generating a step force signal with magnitude $F$ = 10 N and frequency $f$ = 0.5 Hz. The generated piezoelectric current $I$ was measured with a National Instruments PXIe-4139 source meter, for 9-10 cycles of step force. Piezoelectric charge $Q$ values were calculated from the integrated current signal.

To confirm the trends of the macroscopic measurements, PFM measurements were performed on ZnO films grown on Si. The measurements were conducted utilizing an Asylum Research (Oxford Instruments) MFP 3D atomic force microscope using Ti/Ir coated ASYLELEC-01-R2 conductive probe with a nominal tip radius of (25±10) nm and a cantilever spring constant of 2.8 (1.4-5.8) N $m^{-1}$. In order to extend the applicable voltage range, a 10× voltage amplifier F10A from FLC Electronics AB was interconnected between the AFM controller output and the AFM probe. For signal enhancement, the measurements were performed in Dual AC Resonance Tracking (DART) mode, exploiting the superior signal-to-noise ratio enhancement at contact resonance.[37]

### 3.1.6 Acknowledgements

This project has received funding from the European Research Council
(ERC) under the European Union's Horizon 2020 research and innovation program
(Grant Agreement No. 715403).
T. Abu Ali and J. Pilz contributed equally to this work.
Received: ((will be filled in by the editorial staff))
Revised: ((will be filled in by the editorial staff))
Published online: ((will be filled in by the editorial staff))

### 3.1.7 References

[1] H.W. Huang, W.C. Chang, S.J. Lin, Y.L. Chueh, *J. Appl. Phys.* **2012**, *112*, 124102.

[2] M. Jin, J. Jo, G.P. Neupane, J. Kim, K.S. An, J.-W. Yoo, *AIP Adv.* **2013**, *3*, 102114.

[3] Y. Lu, N. W. Emanetoglu, Y. Chen, *Zinc Oxide Bulk, Thin Films and Nanostructures*, Elsevier, **2006**, pp. 443–489.

[4] K. Park, D.K. Lee, B.S. Kim, H. Jeon, N.E. Lee, D. Whang, H.J. Lee, Y.J. Kim, J.H. Ahn, *Adv. Funct. Mater.* **2010**, *20*, 3577–3582.

[5] H. K. Liang, S. F. Yu, H. Y. Yang, *Appl. Phys. Lett.* **2010**, *97*, 241107.

[6] L. Zhu, W. Zeng, *Sensors Actuators A Phys.* **2017**, *267*, 242–261.

[7] C.C. Hsiao, K.Y. Huang, Y.C. Hu, *Sensors*, **2008**, *8*, 185–192.

[8] J. Chen, X. He, W. Wang, W. Xuan, J. Zhou, X. Wang, S. R. Dong, S. Garner, P. Cimo, J. K. Luo, *J. Mater. Chem. C*, **2014**, *2*, 9109–9114.

[9] Z. L. Wang, J. Song, *Science 80.* **2006**, *312*, 242–246.

[10] Ü. Özgür, Y. I. Alivov, C. Liu, A. Teke, M. A. Reshchikov, S. Doğan, V. Avrutin, S. J. Cho, H. Morkç, *J. Appl. Phys.* **2005**, *98*, 1–103.

[11] T. Tynell, M. Karppinen, *Semicond. Sci. Technol.* **2014**, *29*, 043001.

[12] S. M. George*, Chem. Rev.* **2010**, *110*, 111–131.

[13] H. B. Profijt, S. E. Potts, M. C. M. van de Sanden, W. M. M. Kessels, *J. Vac. Sci. Technol. A Vacuum, Surfaces, Film.* **2011**, *29*, 050801.

[14] J. Pilz, A. Perrotta, P. Christian, M. Tazreiter, R. Resel, G. Leising, T. Griesser, A. M. Coclite, *J. Vac. Sci. Technol. A Vacuum, Surfaces, Film.* **2018**, *36*, 01A109.

[15] J. Pilz, A. Perrotta, G. Leising, A. M. Coclite, *Phys. Status Solidi*, **2019**, 1900256.

[16] I. K. Bdikin, J. Gracio, R. Ayouchi, R. Schwarz, A. L. Kholkin, *Nanotechnology*, **2010**, *21*, 235703.

[17] D. D'Agostino, C. Di Giorgio, A. Di Trolio, A. Guarino, A. M. Cucolo, A. Vecchione, F. Bobba, *AIP Adv.* **2017**, *7*, 055010.

[18] W. Qin, T. Li, Y. Li, J. Qiu, X. Ma, X. Chen, X. Hu, W. Zhang, *Appl. Surf. Sci.* **2016**, *364*, 670–675.

[19] M. Laurenti, S. Stassi, M. Lorenzoni, M. Fontana, G. Canavese, V. Cauda, C. F. Pirri, *Nanotechnology*, **2015**, *26*, 215704.

[20] Y. C. Yang, C. Song, X. H. Wang, F. Zeng, F. Pan, *Appl. Phys. Lett.* **2008**, *92*, 012907.

[21] M. Kratzer, M. Lasnik, S. Röhrig, C. Teichert, M. Deluca, *Sci. Rep.* **2018**, *8*, 1–11.

[22] O. Kolosov, *Phys. Rev. Lett.* **1996**, *76*, 4292.

[23] E. Soergel, *J. Phys. D. Appl. Phys.* **2011**, *44*, 464003.

[24] B. S. Blagoev, M. Aleksandrova, P. Terziyska, P. Tzvetkov, D. Kovacheva, G. Kolev, V. Mehandzhiev, K. Denishev, D. Dimitrov, *J. Phys. Conf. Ser.* **2018**, *992*, 012027.

[25] D. Kim, H. Kang, J. M. Kim, H. Kim, *Appl. Surf. Sci.* **2011**, *257*, 3776–3779.

[26] S.H. K. Park, C.S. Hwang, H.S. Kwack, J.H. Lee, H.Y. Chu, *Electrochem. Solid-State Lett.* **2006**, *9*.

[27] P. C. Rowlette, C. G. Allen, O. B. Bromley, A. E. Dubetz, C. A. Wolden, *Chem. Vap. Depos.* **2009**, *15*, 15–20.

[28] J. Zhang, H. Yang, Q. Zhang, S. Dong, J. K. Luo, *Appl. Surf. Sci.* **2013**, *282*, 390–395.

[29] B. Liu, M. Wang, M. Chen, J. Wang, J. Liu, D. Hu, S. Liu, X. Yao, H. Yang, *ACS Appl. Mater. Interfaces*, **2019**, 11, 12656–12665.

[30] J. G. E. Gardeniers, Z. M. Rittersma, G. J. Burger, *J. Appl. Phys.* **1998**, *83*, 7844–7854.

[31] N. J. Blumenstein, F. Streb, S. Walheim, T. Schimmel, Z. Burghard, J. Bill, *Beilstein J. Nanotechnol.* **2017**, *8*, 296–303.

[32] S. J. Kang, Y. H. Joung, *Appl. Surf. Sci.* **2007**, *253*, 7330–7335.

[33] S. C. Abrahams, J. L. Bernstein, *Struct. Crystallogr. Cryst. Chem.* **1969**, *25*, 1233–1236.

[34] S. Park, H. Kim, M. Vosgueritchian, S. Cheon, H. Kim, J. H. Koo, T. R. Kim, S. Lee, G. Schwartz, H. Chang, Z. Bao, *Adv. Mater.* **2014**, *26*, 7324–7332.

[35] X. Yan, W. Ren, H. Xin, P. Shi, X. Chen, X. Wu, *Ceram. Int.* **2013**, *39*, S583–S586.

[36] G. J. T. Leighton, Z. Huang, *Smart Mater. Struct.* **2010**, *19*, 065011.

[37] B. J. Rodriguez, C. Callahan, S. V. Kalinin, R. Proksch, *Nanotechnology*, **2007**, *18*.

## 3.2 Smart Core-Shell Nanostructures for Force, Humidity and Temperature Multi-Stimuli Responsiveness


Reference: Abu Ali, T., Schäffner, P., Belegratis, M., Schider, G., Stadlober, B., & Coclite, A. M. (2022). Smart Core-Shell Nanostructures for Force, Humidity, and Temperature Multi-Stimuli Responsiveness. Advanced Materials Technologies, 2200246. https://doi.org/10.1002/admt.202200246

### 3.2.1 Preface

The work presented in this publication was conducted at Graz University of Technology in cooperation with Joanneum Research. Taher Abu Ali prepared the sample and performed measurements and wrote the manuscript. Philipp Schäffner and Gerburg Schider helped with the data evaluation. Gerburg Schider and Maria Belegratis performed sample preparation and characterization with SEM. Barbara Stadlober and Anna Maria Coclite supervised the work. The published article is reproduced with permission from the publisher.

### 3.2.2 Abstract

A force, humidity and temperature responsive electronic skin is presented by combining piezoelectric zinc oxide (ZnO) and poly-N-vinylcaprolactam-co-di(ethylene glycol) divinyl ether hydrogel into core-shell nanostructures using state-of-the-art dry vapor-based techniques. The proposed concept is realized with biocompatible materials in a simplified design that delivers multi-stimuli sensitivity with high spatial resolution, all of which are prerequisites for an efficient electronic skin. While the piezoelectric property of ZnO provides sensitivity to external force excitations, the thermoresponsive properties of the hydrogel core provide sensitivity to surrounding temperature and humidity changes. The hydrogel core exerts a mechanical stress onto the ZnO shell, which is translated to a measurable piezoelectric signal. A localized force sensitivity of 364 ± 66 pC $N^{-1}$ is achieved with very low cross talk between 0.25 $mm^2$ pixels. Additionally, the sensor's sensitivity to humidity is demonstrated at 25°C and 40°C, i.e. above and below the hydrogel's lower critical solution temperature (LCST) of 34°C. The largest response to temperature is obtained at high humidity and below the hydrogel's LCST. The sensor response to force, humidity and temperature was significantly faster than the system's intrinsic or excitation-induced time scale. Finally, the sensor response to touch and breath demonstrated its applicability as e-skin in real life environment.

### 3.2.3 Introduction

The human skin is composed of a complex and specialized sensory system, which detects surrounding environmental stimuli and transmits the information to the brain.[1] In the last decade, substantial understanding of how this complex system behaves has been gained.[2–4] Nevertheless, its replication to form artificial skins is still a relatively new field with massive potential. Relying on advancements in functional materials, structural design and state-of-art production/deposition techniques, a wide variety of single/multi-stimuli responsive sensory systems, suitable for electronic skin (e-skin) applications, have been reported.[5–8] An efficient e-skin design requires a combination of functional materials with suitable mechanical and electrical properties,[9] in addition to the micro/nanoscale control of the layer's thickness and dimensions, which is optimized by the choice of suitable fabrication techniques.

For pressure and force detection, the most common methods exploit piezoelectric, piezoresistive or capacitive sensing.[10-13] Bao's group investigated an e-skin design based on flexible pressure-sensitive organic thin film transistors deploying a force-sensitive gate dielectric capacitance. The sensor has a maximum sensitivity of 8.4 $kPa^{-1}$ and a fast response time of 10 ms. This was realized with a combination of microstructured polydimethylsiloxane (PDMS) gate dielectric and a high-mobility semiconducting polymer in a transistor design. The sensor relies on capacitance change due to mechanical excitations.[14] Another pressure sensitive e-skin design, investigated by Bao's group, is realized by a composite piezoresistive

material consisting of an organic polymer and nickel nanostructured microparticles.[15] Park and Jang investigated hybrid piezoelectric/piezoresistive pressure sensors based on a nanohybrid material from graphene with free-standing nanofibers of PEDOT/P(VDF-HFP). Their e-skin device impresses with a gauge factor as high as 320 under tensile strain thus showing high sensitivity to pressure with a low limit of detection of 0.5 Pa only.[16]

Humidity sensors for e-skin applications have also been investigated.[17,18] Guo et al. demonstrated that a tungsten sulfite ($WS_2$) film combined with graphene electrodes and PDMS substrate exhibits a high humidity response (up to 90% relative humidity or RH) due to the change in the $WS_2$ conductivity.[19] Similarly, e-skin sensitivity to changes in surrounding temperature is desired and has been investigated.[20–22] Chen et al. presented a flexible temperature sensor for e-skin application based on a semipermeable polyurethane active layer, where its resistivity changes noticeably with the surrounding temperature.[23]

The above-discussed concepts rely on sensors for single physical stimulus. However, multi-stimuli responsiveness is a prerequisite for an efficient e-skin. Several examples of multi-stimuli responsive e-skins are present in literature.[24–29] Ho et al. developed a transparent and stretchable all-graphene multifunctional e-skin sensor matrix sensitive to humidity, temperature and pressure.[30] Another concept of multi-stimuli responsive sensors is presented by Han et al., in which an organic aerogel with mixed ion–electron conductivity is developed to be sensitive to pressure, temperature and humidity with minimal cross-talk.[31] However, of the above-mentioned sensor solutions none can demonstrate multi-stimuli responsiveness and location-specific stimuli-response all at once and they also lack of a simplified architecture as well as biocompatible materials.

In this publication, we demonstrate a flexible skin-like sensor that is responsive to multiple stimuli (force, humidity and temperature, abbreviated as F-H-T) and, since constructed as an array of vertical nanorod pixels, reacts in a location-specific manner to said stimuli. The active layer is made of an array of core-shell nanorods consisting of a Poly-N-vinylcaprolactam-co-di(ethylene glycol) divinyl ether (p(NVCL-co-DEGDVE)) hydrogel core and a zinc oxide (ZnO) piezoelectric shell. The choice of p(NVCL) hydrogel is due to its thermoresponsive nature. p(NVCL), which is non-toxic and biocompatible,[32] possesses hydrophilic functional groups (caprolactam ring) that bond with water molecules. This bonding mechanism is dependent on a specific temperature defined as the lower critical solution temperature (LCST): the hydrogel undergoes a phase transition from a swollen hydrated state below to a shrunken dehydrated state above the LCST, resulting in desired sensitivity to temperature and humidity. In a previous contribution, we showed that the LCST can be tailored by copolymerization of the NVCL with DEGDVE. This, beyond being a cross-linker, adds hydrophobic functional groups to the polymer chains reducing the LCST of p(NVCL).[33]

In our design, temperature and humidity changes in the surrounding environment are sensed by the p(NVCL-co-DEGDVE) core, which swells as a result (**Figure 19a**). The hydrogel swelling mechanically strains the ZnO shell and a measurable current/charge is in turn generated due to its piezoelectric nature.[34] Apart from this indirectly induced mechanical stress, an applied force can be directly sensed by the ZnO shell. The choice of ZnO for the shell is based on several advantages related to this material. First, it exhibits both semiconducting and piezoelectric properties that can be used to transform mechanical stresses into electric current for electromechanically coupled sensors and transducers.[35] Secondly, ZnO is relatively biosafe and biocompatible, and it can be used for biomedical applications with little toxicity.

Arrays of core-shell structures, like the one schematized in Figure 19a, can be obtained by subsequent deposition in porous templates. The template-deposition of polymers or of inorganic materials requires the coating of high-aspect-ratio nanopores with high conformality. Liquid phase-based or line-of-sight deposition methods (sputtering, plasma-assisted chemical vapor deposition, evaporation) may not uniformly fill the pores, resulting in low quality nanorods. Therefore, we used initiated chemical vapor deposition (iCVD) for the hydrogel core and plasma-enhanced atomic layer deposition (PEALD) for the ZnO shell. Both these techniques are driven by surface-limited reactions, which ensure highly conformal coating and/or filling of the template pores. We previously demonstrated that the piezoelectric properties of ZnO deposited by PEALD depend on the deposition temperature, where a film of ZnO as thin as 50 nm deposited on a glass/ITO substrate at 25°C exhibits an apparent $d_{33}$ coefficient of 3 pC $N^{-1}$, which increases to 20 pC $N^{-1}$ when deposited at 225°C.[36]

Skin-like sensors usually consist of an array of touch sensitive sites, called tactile pixels or taxels, which may be capable of measuring more than one property.[15] In nature, tactile recognition, i.e. the detection of object features, such as surface texture and fine form discrimination, is carried out by a large number of corpuscles and free nerve endings sensitive to mechanical stimuli (mechanoreceptors). Psychophysical studies have shown that the limiting spatial resolution of human fingertips is of the order of 1 mm.[1] Skin normally experiences multi-axial forces and undergoes a range of angular and linear motions at different body locations. This heterogeneity in movements and strains of skin suggests the need for location-specific optimization of sensors in artificial skins and prosthetics.[37] Kim et al.[26] have achieved such location-specificity in a prosthetic skin equipped with a series of different sensors for strain, pressure and temperature in a multi-layered device. Different sensors for each stimulus were used (e.g. a sensor for strain, another for temperature, another for pressure) and dislocated into the matrix with a quite laborious architecture. To achieve high resolution and multi-sensitivity at the same time we used a completely different device architecture, based on vertical sensing nanorods with a lateral dimension of only 500 nm,

instead of horizontal layers. Each pixel of our device contains thousands of sensing nanorods and the signal is read out electronically at every individual pixel.

### 3.2.4 Results and Discussion

The core-shell nanorods are embedded in a polyurethane acrylate (PUA) polymeric template that is nanopatterned by UV-nanoimprint lithography (UV-NIL). The nanostructured layer is then sandwiched between two electrodes. The detailed fabrication steps of the core-shell nanorod array are shown in **Figure 19b** (thickness of layers not shown to scale). Starting with a PET substrate, a bottom electrode (BE) of chromium/silver (Cr/Ag) with thickness of 2.5/50 nm is first deposited by thermal evaporation through a shadow mask. Then, UV-NIL is utilized to imprint nanoholes into a layer of PUA deposited on top with a stamp (**Figure 25a**) featuring nanorods, as shown in **Figure 25b**. During the imprint process, a force $F$ = 30 N is applied onto the stamp for 30 minutes, which reduces the thickness of the PUA layer to ≈ 6 µm (**Figure 25c**). The resulting nanoholes (diameter $d$ = 500 nm and height $H$ = 500 nm) prior to deposition of the core-shell layers are shown in **Figure 19c**. Subsequently, deposition of the ZnO shell with a thickness of 50 nm is carried out at 35°C using PEALD, followed by deposition of the p(NVCL-co-DEGDVE) core with a thickness of 200 nm via iCVD. The diameter of the nanoholes was chosen to maximize the number of nanorods in the electrode area ($10^8$ nanorods in 1 $cm^2$ electrode area) and at the same time have that both ZnO and the hydrogel are thick enough to ensure large response. As a last fabrication step, two designs of an Ag top electrode (TE) with a thickness of 50 nm are deposited by evaporation through respective shadow masks. The first design is composed of a single TE field with an active area of 1 $cm^2$ (**Figure 19d**). The second design is composed of six TE fields, each with an active area of 0.25 $mm^2$ and spaced 5 mm apart. The fabrication of the sensor consists exclusively of process steps that can be carried out sequentially in a pilot line, such as vacuum evaporation for the electrodes, nanoimprint lithography and chemical vapor deposition (for the hydrogel core and the piezoelectric shell).

Figure 1c corresponds to the cross-sectional SEM image of a patterned PUA template prior to filling, whereby **Figure 19e** is an SEM close-up of three nanoholes after filling with a thin ZnO layer (50 nm) and hydrogel (200 nm). It can be observed that the techniques used to deposit the core-shell nanorods deliver the desired uniform profiles: conformal ZnO deposition by PEALD and complete filling of nanoholes with the iCVD-deposited hydrogel core. The iCVD deposition conditions were optimized to achieve a fractional saturation pressure for the monomer ($p_m/p_{sat}$) and cross-linker at 0.15 and 0.04, respectively, which is recommended for conformal layer coating.[38] During cross-sectional cuts of samples for SEM imaging, slight delamination was observed within some nanoholes due to the difference in Young's modulus $E$ of the PUA template and ZnO.[39-43]

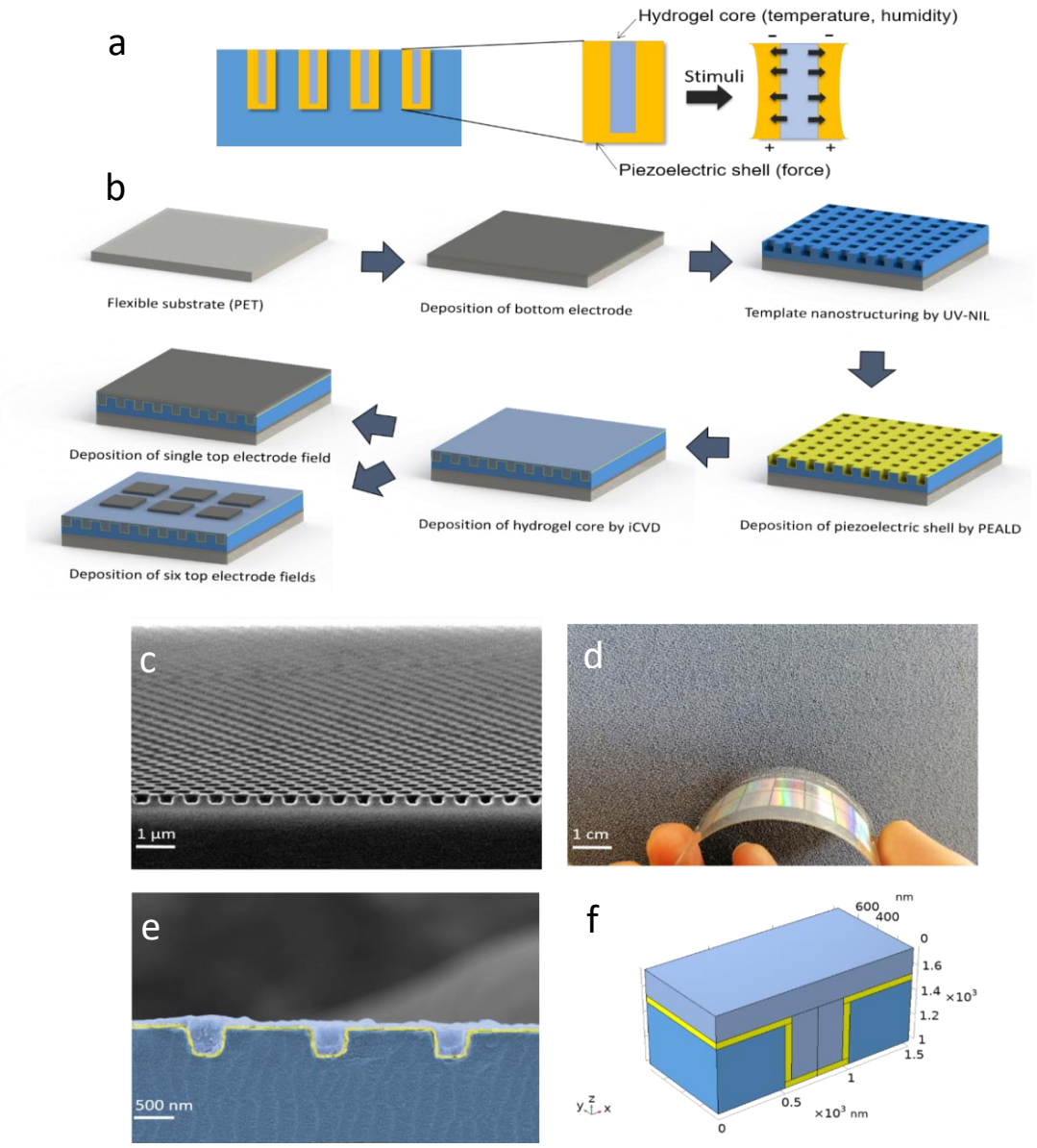


Figure 19. a) Cross-sectional view of the core-shell nanorod sensing concept, where a ZnO piezoelectric shell directly senses force. The hydrogel core, which swells, senses humidity and temperature changes and a resultant stress is applied onto the ZnO piezoelectric shell. b) F-H-T responsive sensor fabrication routine (dimensions are not shown to scale). Starting with a PET substrate, a bottom electrode (BE) is deposited using e-beam evaporation. A PUA template layer is then applied and nanostructured using UV-NIL. The ZnO piezoelectric shell is deposited using PEALD. Next, the hydrogel core consisting of p(NVCL-co-DEGDVE) is deposited using iCVD and finally, two top electrode (TE) designs are deposited with e-beam evaporation (indicated as single electrode field and six electrode fields). c) SEM image of a patterned PUA template prior to filling with core-shell structures. d) Photograph of the complete sensor design with 1 $cm^2$ TE active area under bending. e) Colorized SEM image featuring three core-shell nanorod structures: a conformal ZnO shell (yellow) deposited on the nanopatterned PUA (dark blue) and the hydrogel core (navy blue) completely filling the nanoholes. f) Corresponding geometry model used for FEM simulations

The working principle of the as-fabricated device is based on the deformation of the piezoelectric shell induced by the swelling of the hydrogel. Previous work published by our group extensively characterized the swelling behavior of p(NVCL-co-DEGDVE) films on Si

(100) substrate, deposited using the same iCVD reactor/conditions used in this work. [33] It is indicated that films with 10% nominal cross-linking experienced the highest swelling response in water (represented by the ratio of thickness upon swelling to dry thickness, $d/d_{dry}$) but delaminated from the substrate during prolonged water-exposure and therefore were unstable. [33] Stable films were obtained with 20% nominal cross-linking. In the present work, p(NVCL-co-DEGDVE) films with 25% nominal cross-linking have been deposited for improved stability. The cross-linker fraction influences the LCST of the hydrogel (increasing cross-linker fraction decreases the LCST). For p(NVCL-co-DEGDVE) with 25% nominal cross-linker fraction, the LCST is measured at 34±2 °C.[33]

The swelling behavior of the hydrogel core is of high importance to simulate the sensor performance with respect to humidity and temperature. Within the finite element method (FEM) simulation, the symmetrical geometry allows to model one-half of a nanorod. **Figure 19f** shows the geometry used for the simulations: a section of the patterned PUA template (colored in blue), bare, with 50 nm of conformal ZnO layer (colored in yellow) and with complete filling of the nanohole by the hydrogel core (colored in navy blue). The hydrogel swelling behavior is modelled following **Equation 50**:

$$\varepsilon = \beta \, x \, C_{mo} \qquad (50)$$

Where, $\varepsilon$ is the hygroscopic strain exerted by the hydrogel core on the ZnO shell. $\beta$ is the hydrogel swelling coefficient ($m^3$ $kg^{-1}$) and $C_{mo}$ is the moisture concentration in air (kg $m^{-3}$; equivalent to RH %). **Table 3** shows $\beta$ and $C_{mo}$ values calculated for p(NVCL-co-DEGDVE) 25 % nominally cross-linked grown on ZnO (50 nm) on a Si substrate. $\beta$ is calculated at 10, 25, 35, 40 and 50°C (below and above LCST) at different RH% ($C_{mo}$). In addition to simulating the response to humidity and temperature, the simulated sensor response to force is performed by applying a boundary load condition, where the input force is given per unit area (N $m^{-2}$).

The sensor dielectric properties as well as I-V response is performed in order to assess the current flow from bottom to top electrode across the template, which acts as a dielectric layer. **Figure 20a** shows the real part of the dielectric constant $\varepsilon'$, which is measured in the frequency range $f$ = 42 Hz up to 5 MHz for a sensor with a hydrogel core in comparison to a reference sensor without a hydrogel core. The measurements were performed on a sensor with an active TE area of 1 $cm^2$. At 42 Hz, the dielectric constant amounts to 6.3 for the sensor with a hydrogel core and 5.3 for the sensor without the hydrogel core. $\varepsilon'$ drops to 5.3 and 4.7 at $f$ = 10 kHz, The sharp drop in ε' between 10 kHz and 1 MHz is related to dipolar relaxation, which typically occurs between 1 Hz and 100 MHz for polymers.[44] The dielectric properties of the hydrogel

are influenced by the moisture content inside its polymeric mesh, where the dielectric constant of water is ≈ 80.[45] However, in its dry state, a thermoresponsive hydrogel typically shows ε' values of 3 to 4.[46] Moreover, due to the measurements being performed in ambient humidity conditions (40% RH) and the much thinner hydrogel core layer in comparison to the PUA template layer (200 nm << 6 µm), the sensor overall ε' is mainly dependent on the thickness and dielectric properties of the PUA layer (see supporting note 1 for calculation of theoretical dielectric constant). *I-V* characterization curves were measured for both sensors (with and without the hydrogel core) in the voltage range $V = \pm 20$ V (**Figure 20b**). For the sensor with a hydrogel core, the measured current density $J$ is $1.7 \times 10^{-6}$ A cm$^{-2}$ at –20 V and $1.3 \times 10^{-5}$ A cm$^{-2}$ at +20 V. For the sensor without a hydrogel core (reference), $J = 1.7 \times 10^{-7}$ A.cm$^{-2}$ and $1.8 \times 10^{-7}$ A.cm$^{-2}$ at –20 V and +20 V, respectively. The results indicate that the hydrogel core increases the leakage current of the sensor. The current density asymmetry is related to charging effects, which are enhanced with the presence of a sensor with a hydrogel core of respectively.

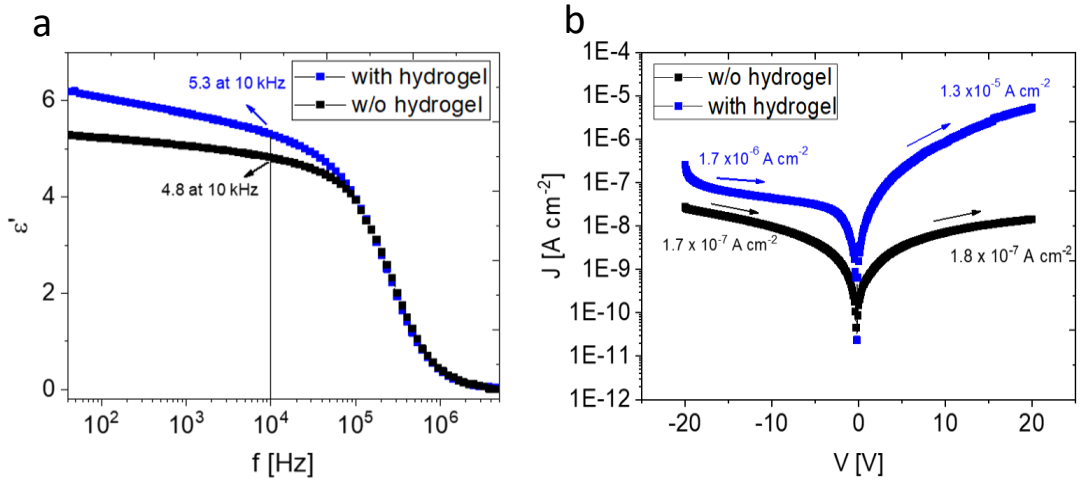


Figure 20. a) Real part of dielectric constant ε' measured as a function of frequency *f* in the range of 42 Hz - 5 MHz for a sensor with and without a hydrogel core. b) I-V characterization performed at V = ±20 V for a sensor with and without a hydrogel core

*Full-area force response:* **Figure 21a-d** show the sensor scheme (single TE with an active area of 1 cm$^2$) and response to external force stimuli, where different force intensities of $F$ = 10, 12, 15 and 20 N were applied using a piezoelectric test setup, as schematized in **Figure 26a**. **Figure 21b** shows the generated current as a function of time for a step excitation force signal of 10 N for 4 cycles, with a maximum current $I$ of 0.21 ± 0.02 nA measured upon pressing with a rounded pneumatic stamp (diameter $d$ = 5 mm). A zoomed-in graph shows a sensor response time of ≈ 28 ms (**Figure 21c**). The charge $Q$ is calculated from integrating $I$ over time $t$ and is plotted as a function of the force (**Figure 21d**).

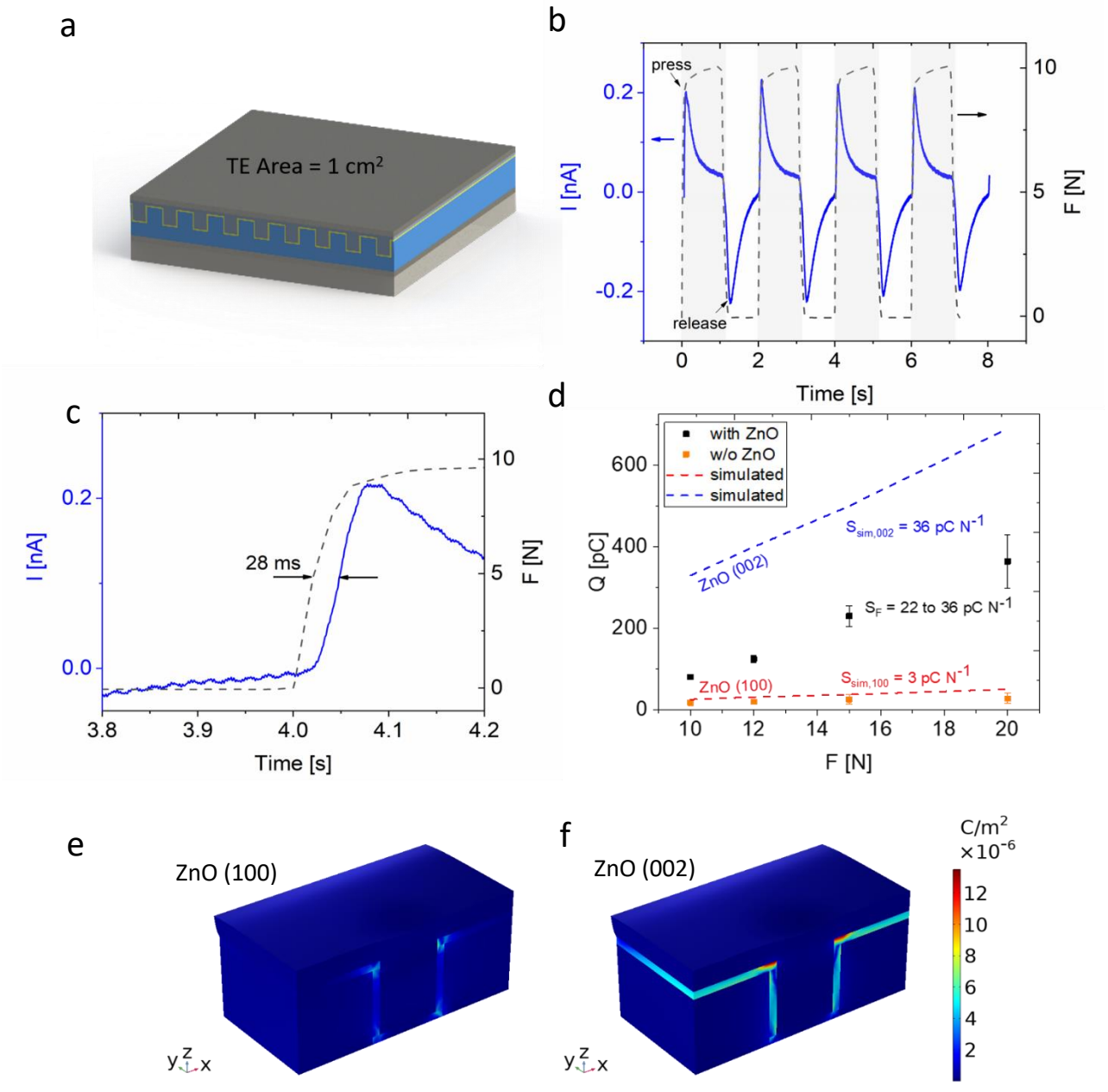


Figure 21. a) Schematics of a sensor with a TE active area of 1 cm$^2$ (dimensions are not shown to scale). b) Current I response over time *t* to a 10 N step force stimulus. c) Zoom-in of figure 21b showing the sensor response time to 10 N step force stimulus. d) Charge *Q* (integrated current signal) as a function of excitation force (10, 12, 15 and 20 N) for a sensor with ZnO, a reference sensor without ZnO as well as the simulated response using FEM simulations. The variation in the charge response for a given force level (error bars) is calculated from three measurements each performed on two sensors (sample size, $n$ = 6). The sensor sensitivity to force, $S_F$, is also reported in the figure. 21D polarization distribution spatial maps (cf. colour bar) obtained from FEM simulation on piezoelectric ZnO with d) (100) preferential orientation and e) with (002) preferential orientation

As observed from Figure 21d, upon a force excitation of $F$ = 10 N, a charge response of 81.0 ± 1.7 pC is measured, increasing to 364 ± 66 pC at $F$ = 20 N. The charge response corresponds in good approximation linearly to the force, with an apparent offset. This offset can be related to a high deformation/compression of the hydrogel layer at low forces, thus lowering the stress exerted onto the ZnO layer. The sensor sensitivity to force excitations, $S_F$, is calculated following **Equation 51**.

$$S_F = \Delta Q / \Delta F \qquad (51)$$

It amounts to 22 - 36 pC $N^{-1}$. The upper sensitivity limit of the experimental data matches the sensitivity $S_{sim,002}$ = 36 pC $N^{-1}$ calculated from the FEM model, where ZnO (002) is considered. A reference sensor response (without ZnO shell and hydrogel core) was measured at $F$ = 10, 12, 15 and 20 N with a maximum $Q$ = 28 ± 12 pC. Given that the response is significantly lower than what is measured with a fully fabricated sensor containing the core-shell nanostructures, we can conclude that the sensor response to force is due to piezoelectric ZnO. The FEM model delivered different charge values compared to the ones measured experimentally. Such difference is attributed to two factors: first, ZnO deposited at 35°C crystalizes mainly into (100) crystallographic orientation (piezoelectric polar axis is parallel to substrate surface), [36,47,48] but also (002) crystallographic orientation (piezoelectric polar axis perpendicular to substrate surface). The presence of (002) orientated crystallites in ZnO enhances the piezoelectric response to force excitation parallel to the z-axis.[36,49–51] In the FEM model, ZnO is single crystalline, therefore the piezoelectric axis is oriented either completely along the (100) direction, or completely along the (002) one. As shown in Figure 21d, the piezoelectric charge obtained from the simulation with a (002) oriented ZnO single crystal is higher than the piezoelectric charge obtained from the simulation with (100) orientation.

The experimental results lie in between these two extreme cases, which is expectable, considering that the ZnO deposited by PEALD at 35°C has both (100) and (002) oriented crystals.

Another contribution affecting the force response comes from substrate bending, which has to be considered for the flexible PET substrates used. Bending of the substrate generates charges through the transverse piezoelectric effect (attributed to the $d_{31}$ coefficient of piezoelectric ZnO) in addition to the longitudinal piezoelectric effect (attributed to the $d_{33}$ coefficient of piezoelectric ZnO), which increases the measured piezoelectric charge.[52,53] In the FEM simulation of a single nanorod the substrate is not considered and the influence of substrate bending is not taken into account. To validate the assumption of substrate bending, a 2D FEM model is used to model the active layer/thin film/substrate bending due to the different contributions of the stress/strain components (**Figure 27a**). **Figure 27b** shows the stress distribution within the thin film layer and the PET substrate at $F$ = 10 N. It can be clearly

concluded that the highest stress occurs close to the stamp edge, which results in strong deformation. In this region, the deformation of the substrate induces a large longitudinal tensile strain component and a transverse compressive strain component within the thin film/active layer as shown in **Figure 27c** and **Figure 27d**. The results of the 2D FEM model clearly show that the experimentally measured piezoelectric response is strongly influenced by the transverse piezoelectric effect due to the bending of the flexible substrate and thus the active layer. The 3D polarization distribution spatial map shown in **Figure 21e** and **Figure 21f**, obtained for $F$ = 10 N applied as force per unit area through a boundary load condition, indicates that the maximum charge is generated at the edges of the nanostructure for both ZnO orientations, and decays substantially along the lateral dimensions.

This is important for obtaining site-specific pressure sensing with high lateral resolution and it is the advantage of using the nanostructuring approach. Contrarily, if the generated piezoelectric charge would be constant along the whole ZnO layer, the resolution of force sensing would be lower: the force response would be higher at the excitation location, where the force is applied, and would gradually decrease in the lateral direction.

*Localized-area force response:* in order to demonstrate such site-specific sensing, a set of sensors is fabricated with a structured TE depicted in **Figure 22a**. The design relies on six electrode fields/pixels, each with an active area of 0.5 mm × 0.5 mm and 5 mm spacing between neighboring fields. In the experiment, pixel B1 was excited with a step force signal of 10 N applied through a stamp with $d$ = 1 mm, using the same piezoelectric test setup schematized in Figure 26a. Minimum cross talk between electrode fields/pixels is observed as shown in **Figure 22b**. **Figure 22c** shows the piezoelectric current time response of pixel B1 when excited over 4 cycles. A peak current $I$ of 0.6 nA was measured, which translates to a piezoelectric charge $Q$ = 170 pC per step. **Figure 28** shows the generated charge from different pixels for step force excitations with magnitude of 10 N and 4 N. At $F$ = 10 N, a maximum charge $Q$ = 270 pC is measured for pixel A1 and a minimum charge $Q$ = 100 pC is measured for pixels B2 and C1, while for $F$ = 4 N a maximum charge of 170 pC and a minimum charge of 30 pC were measured for pixels A1 and C1, respectively. Variations in the measured charge at different pixels are attributed to thickness variations along the PUA imprint layer as explained in the SI. The sensor response to 5 cycles of force excitations from a finger touch is tested using the experimental setup schematized in **Figure 26b**, where $Q$ is calculated, showing a response of 216 to 252 pC with a signal rise time $t_r$ = 0.75 s (**Figure 22d**).

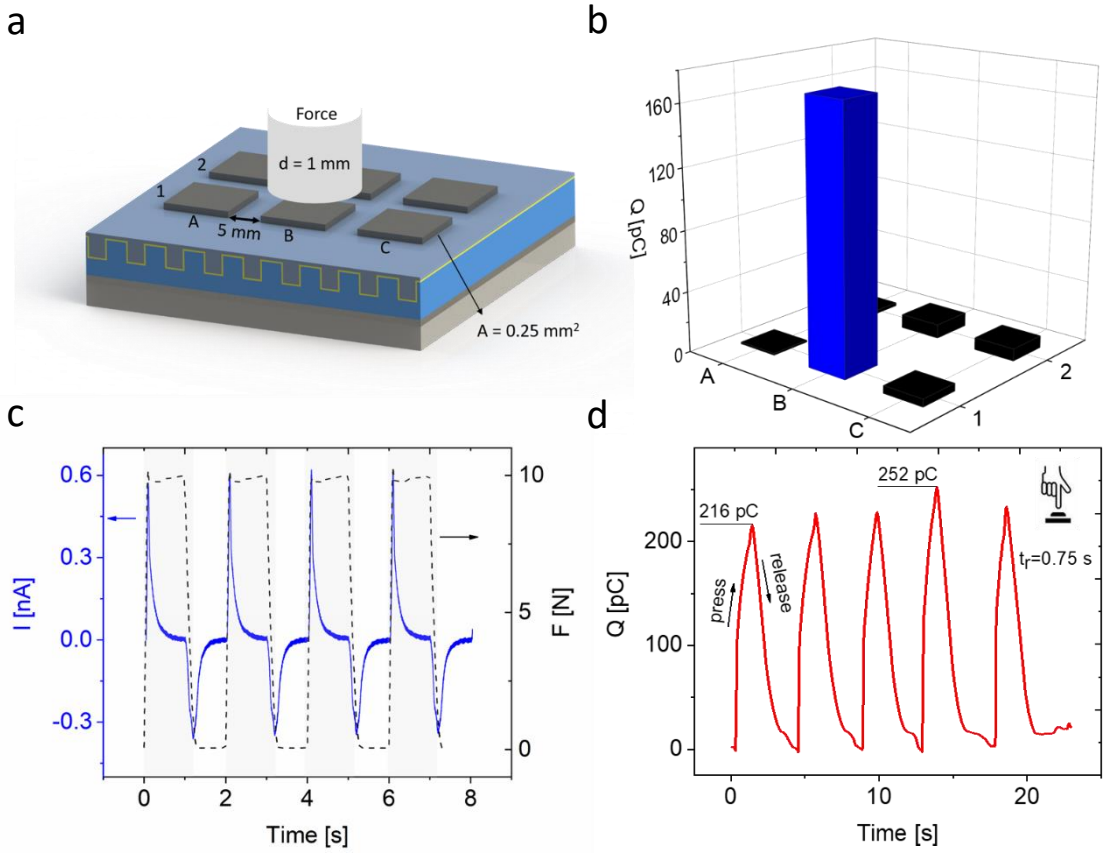


Figure 22. a) Schematics of six TE fields ($A$ = 0.25 mm$^2$) for localized response to force, where pixel B1 is excited with $F$ = 10 N, using a force stamp with diameter $d$ = 1 mm (dimensions are not shown to scale). b) 3D plot of piezoelectric charge response of pixel B1 and its neighboring pixels when excited with $F$ = 10 N. c) Current $I$ response of B1 over time, $t$, to 10 N step force signal for 4 cycles. d) Sensor response to 5 cycles of force excitations from a finger touch with a maximum response $Q$ = 252 pC

*Humidity and temperature response:* the sensor response upon humidity and temperature changes is measured in terms of piezoelectric charge in an environmental chamber as depicted in **Figure 26c**. The response is measured from 25% up to 96% RH, using a sensor with a TE area of 1 cm$^2$. The charge response over time at 25 °C for varying humidity conditions is shown in **Figure 23a**, while **Figure 23b** depicts the charge as a function of relative humidity. At 25°C, the hydrogel is below its LCST (34± 2°C) and as a result has a high tendency to absorb water molecules, compared to the hydrogel at 40°C, resulting in a maximum response of 14.2 ± 1 nC at 96% RH. This is due to the polymer chain configuration, where strong hydrogen bonds between the hydrogel's hydrophilic functional groups (carboxylic and cyclic amide) and water molecules are present (**Figure 23c and 23d)**.[54] The sensor sensitivity, $S_{H1}$, at 25 °C is calculated to be 0.1 nC %$^{-1}$ for the (relative) humidity range 25 to 85% and $S_{H2}$ = 1.2 nC %$^{-1}$ for the RH range between 85 and 96%. The previously observed non-linear increase in swelling [55] results in a high increase in $S_{H2}$ above 85% RH. Figure 23b shows $Q$ as a function of RH at 25°C (below LCST) and 40°C (above LCST) for the sensor with a hydrogel layer compared to a reference sensor. Above the LCST, a change in the hydrogel's polymer

chain configuration occurs, which enhances inter- and intramolecular interactions between the hydrogel's hydrophobic groups resulting in less water absorption and incorporation into the hydrogel's mesh (coil-globule transition as depicted in Figure 23c).[54] The hydrogel experiences less swelling and thus lower stress is exerted onto the ZnO shell compared to that measured at 25°C. Accordingly, above the LCST, the maximum response at 96% RH is 4.0 ± 0.3 nC, about one third of the value at room temperature. At 40°C, the sensitivity $S_{H3}$ is calculated to be 0.01 nC $\%^{-1}$ between 25 and 85% RH and $S_{H4}$ = 0.1 nC $\%^{-1}$ between 85 and 96% RH. The reference sensor shows no response to humidity, confirming that the sensor response is indeed due to the hydrogel core swelling.

These observations with regard to humidity sensing are also confirmed by FEM simulations, which according to **Figure 23e** and **23f** show a maximum stress σ of 17.4 MPa at 60% RH below the LCST vs 13.4 MPa above LCST. The simulated charge response obtained from the FEM model (Figure 23b, dashed lines) is in very good agreement with the experimental data for both temperature conditions up to a RH of 80%. In addition, in both cases, the maximum stress exerted on ZnO occurs at the edge of the nanostructures.

In the same experimental setup, the sensor response to temperature was investigated. **Figure 24a** displays the sensor response to a temperature profile at 96% RH. The temperature is gradually decreased from 50°C to 10°C, therefore ensuring that the hydrogel transitions from low to high swelling regime (LCST = 34 ± 2°C). The experiment was repeated for two different humidity levels (96% and 40%) as well as for the reference sensor and the corresponding charge curves are plotted as a function of temperature in **Figure 24b**. At 96% RH, the sensor temperature sensitivity, $S_T$, was found to be -0.14 nC $°C^{-1}$ within a temperature range between 50°C ($Q$ = 0.03 nC) and 30°C ($Q$ = 2.1 nC). Below 30°C, a signal is measured but it does not change with temperature. This is a direct consequence of the hydrogel swelling profile, where the thickness changes around the LCST and stays constant for lower temperatures. However, no response to temperature was observed at low RH (40%), indicating that the hydrogel's sensitivity to temperature occurs around the LCST and at high RH.[55] This trend is also confirmed by FEM simulations, which indicate a saturation of the generated charge generation below 30°C at 95% and 70% RH. Similar to the above-mentioned humidity characterization measurements, a reference sensor without hydrogel layer measured at 96% RH in the temperature range of 50°C to 10°C and it showed no significant response to temperature.

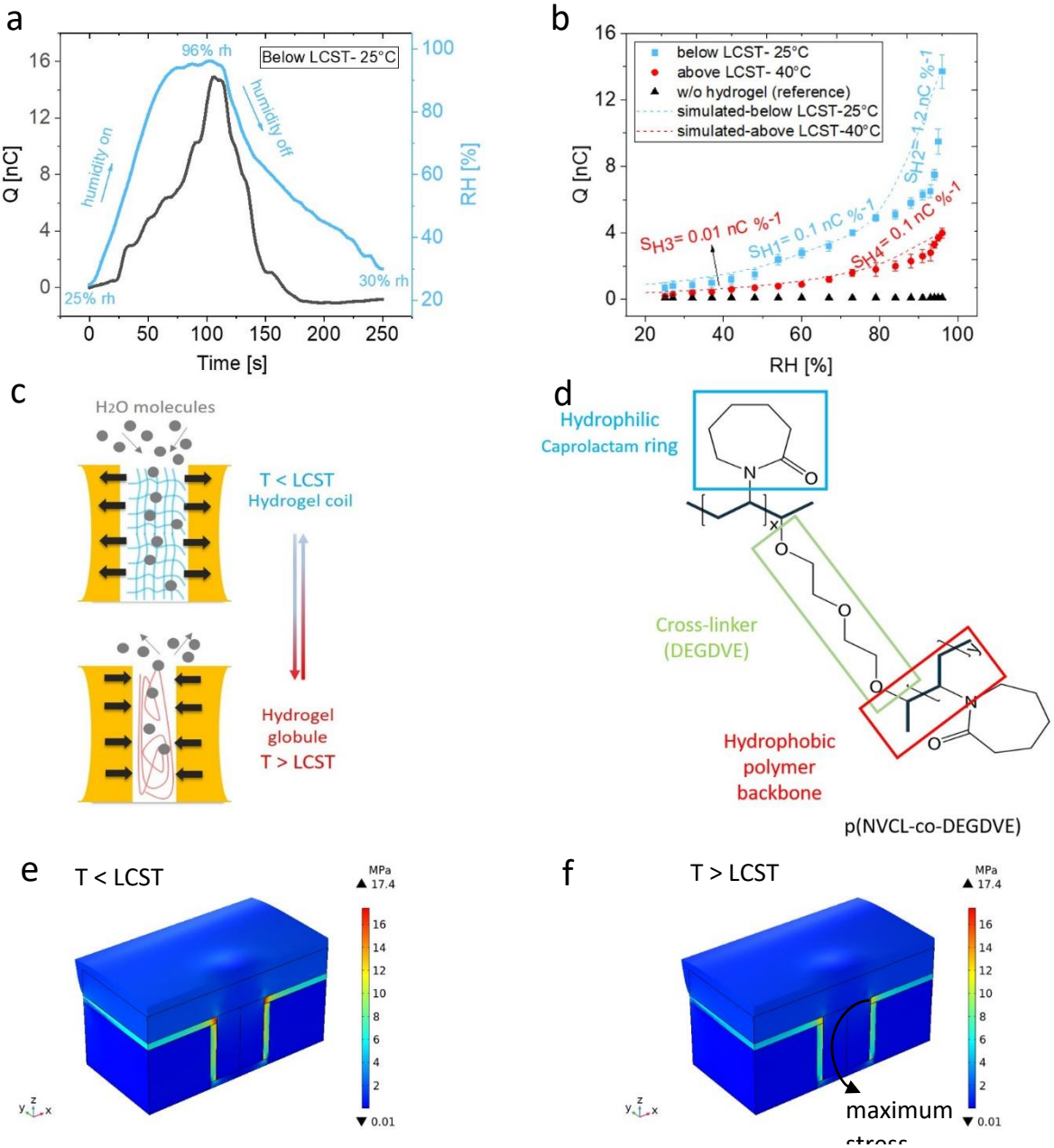


Figure 23. a) Sensor charge response to changes in humidity (RH = 25% - 96% - 30%) as a function of time. b) Humidity response of the sensor at 25°C (below LCST) and 40°C (above LCST), respectively, and a reference sensor (without a hydrogel), where $S_H$ is indicated for four regions. The experimental data are averaged over two measurements ($n$ = 2) and the standard deviation is shown as error bar. Where the error bar is not visible, it is hidden by the data symbol. c) Schematics of hydrogel swelling mechanism and LCST influence on hydrogel swelling. d) Molecular structure of the hydrogel core. Stress distribution in the ZnO shell due to hydrogel swelling e) below and (f) above LCST, obtained from FEM model

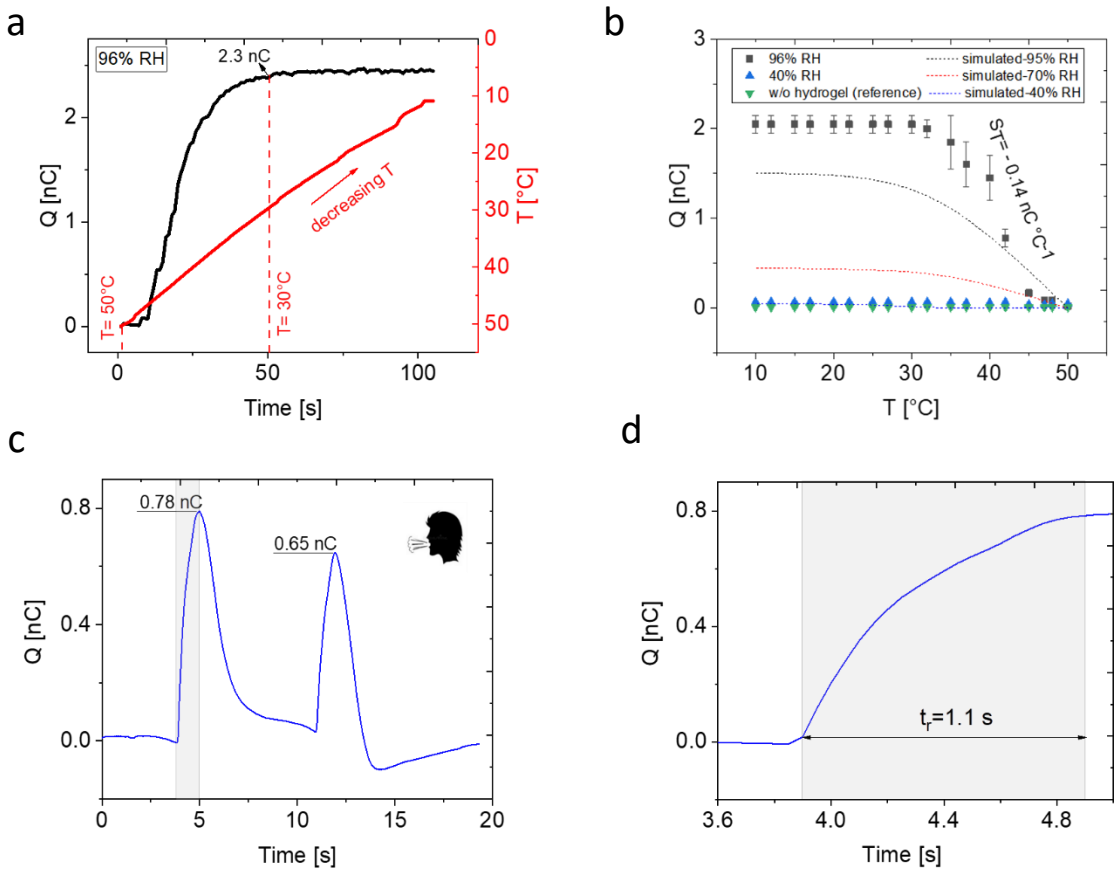


Figure 24. a) Sensor response *Q* to temperature *T* (50°C – 10°C) at 96% RH as a function of time. b) *Q* as a function of temperature at *RH* = 96% and 40 % and a reference sensor without a hydrogel layer, with $S_T$ indicated at 96% RH. The experimental data are averaged over two measurements ($n$ = 2) and the standard deviation is shown as error bar. Where the error bar is not visible, it is hidden by the data symbol. c) Sensor response to air blown from a human mouth, with a maximum *Q* = 0.78 nC. d) zoomed-in figure 24c showing signal rise time $t_r$ = 1.1 s

Finally, yet importantly, we could use the sensor to detect the air blows from a human mouth from an approximate distance of 10 cm using the experimental setup schematized in Figure 26b. For the consecutive blows the charge peaked with values between 0.65 nC to 0.78 nC (**Figure 24c**) and the signal rise time is about $t_r$ = 1.1 s (**Figure 24d**). The sensor response is attributed to highly humid air blown from the human mouth rather than to the induced temperature change as such an air blow has a relatively low temperature (30°C).

### 3.2.5 Conclusion

In conclusion, we have demonstrated a multi-stimuli force, humidity and temperature (F-H-T) responsive sensor fabricated on flexible PET substrate for electronic skin applications. The sensor relies on combining piezoelectric ZnO with p(NVCL-co-DEGDVE) hydrogel into novel core-shell nanostructures. In a previous paper from our group, we demonstrated that the transition temperature of p(NVCL-co-DEGDVE) can be tuned on a large range from ca. 40°C

to 15°C.[33] This allows to tune its response to a desired temperature range. In this design, the used deposition conditions were chosen to obtain a transition at near-body temperature, which may be useful for artificial skin applications.

The core-shell nanorods are embedded into a nanopatterned PUA template. The sensor response to force is successfully demonstrated with an in-house piezoelectric measurement setup at different force magnitudes, applied parallel to the sensor's z-axis. The force-sensitivity is as high as $S_F$ = 22 - 26 pC $N^{-1}$. As for the response to humidity and temperature, measurements in an environmental chamber revealed a maximum sensitivity to relative humidity of $S_{H2}$ = 1.2 nC $\%^{-1}$, obtainable below the LCST of the hydrogel and at high relative humidity (≥ 85% RH). Additionally, above the hydrogel LCST and at saturated relative humidity levels still a sensitivity of $S_{H4}$ = 0.1 nC $\%^{-1}$ could be achieved, while a maximum sensitivity to temperature $S_T$ = -0.14 at 96% RH is obtainable for a temperature range between 30 and 50 °C. The enhanced sensor sensitivity to humidity and temperature (in comparison to force) is a result of the nanostructuring approach,[14,56] which increases the contact surface area between the hydrogel core and the piezoelectric shell. We believe this difference in sensitivity for the different stimuli can be used for stimuli recognition, upon signal analysis. Alternatively, force and temperature can be distinguishable by slightly modifying the template/electrode design, to achieve pixels with nanorods filled with hydrogels and pixels with smaller trenches so that the rods would be filled only by ZnO.

Another advantage of this approach is that for force excitations parallel to the sensor's z-axis, the maximum charge is generated at the edges of the nanostructures and decays substantially along the lateral dimensions. This enables achieving site-specific force sensing with a very high spatial resolution, in principle, down to the dimensions of a single nanostructure, if the sensor electrodes were to be miniaturized to such dimensions. Using a design with adjacent square electrode fields each having only 0.25 mm², a force excitation could be spatially resolved with a negligible low cross talk between neighboring fields. The sensor response time to force as well as humidity is comparable to literature.[14,16,18,19,30] Moreover, the sensor response is significantly faster than the system's intrinsic or excitation induced time scale and any delay comes from the specifics of excitation. Finally, the sensor response to a finger touch and air blown from a human mouth demonstrates the sensor applicability as e-skin element in real life environment.

### 3.2.6 Experimental Setup

*Fabrication:* the multi-stimuli *F-H-T* responsive sensor is fabricated according to the processing steps shown in **Figure 19b**. Starting with a 125 µm thick polyethylene terephthalate (PET) substrate with dimensions of 90 × 60 mm² (Melinex STS 505, Dupont Teijen Films), e-beam evaporation is used to deposit an ultra-thin (2.5 nm) chromium adhesion layer, followed by a

layer of silver (50 nm) serving as a bottom electrode (BE). An e-beam deposition rate between 0.10 and 0.25 nm/s was applied. The BE had an active area of 75 × 40 mm². Then, a resin based on polyurethane acrylate (PUA) (NILcure™, Joanneum Research) was deposited manually using a glass pipette (resin volume ≈ 1 mL) and nanostructured by UV nanoimprint lithography (UV-NIL) using a UV light source (USDT-20ML-8R, Biostep) with a wavelength $\lambda$ = 365 nm and a curing time $t_{cur}$ of 60 s. For imprinting, a transparent polymeric stamp (NILcure™, Joanneum Research) was first prepared from a cyclic olefin copolymer master (COC, STRATEC Consumables GmbH and Fianostics GmbH) following the same UV-NIL parameters/procedure described above. The nanostructures, i.e. nanoholes, on the master had a diameter $d$ = 500 nm, height $H$ = 500 nm, aspect ratio AR = 1 and a pitch = 1000 nm and were arranged in 16 square fields each 8 × 8 mm structured squares. During imprinting, a force $F$ = 30 N was maintained on the stamp for 30 minutes to reduce the imprint layer to the desired thickness $t$. Finally, after stamp demolding, a UV-post curing step (395 nm, 120 s) (BLD-240-C210-ERS, uPowerTek) was performed. To form the piezoelectric shell, a thin ZnO layer (50 nm) was deposited at 35°C into the nanostructured PUA template by means of plasma-enhanced atomic layer deposition (PEALD), with a custom-built direct plasma ALD reactor used. The reactor has an asymmetrical plate configuration, in which the radio frequency (RF) and the ground electrode are 18 cm and 20 cm in diameter, respectively. A distance of 11 cm is maintained between both electrodes. Diethyl zinc (DEZn, Dock/Chemicals) flow into the reactor is controlled by an ALD-valve (ALD3, Swagelok). An RF plasma power generator (Cesar 13.56 MHz, Advanced Energy) is used to deliver the required input power through a matching network (Navio, Advanced Energy). Oxygen ($O_2$) and argon (Ar) are flown into the reactor using a mass flow controller (MFC-GE50A, MKS) with a flow rate set to 20 sccm. $O_2$ is flown into the reactor during the plasma step, while Ar is used as a purging gas. The pump system in use consists of a rotary vane pump (DUO 20, Pfeiffer Vacuum) and a turbomolecular pump (TMH071P, Pfeiffer Vacuum). Using a butterfly valve (MKS 253B), the pressure is set to 200 µbar during the plasma step. At 35 °C, 250 cycles are needed to deposit 50 nm of ZnO. A single cycle consists of (1) an $O_2$ plasma step, (2) an Ar purging step, (3) a DEZ step and (4) an Ar purging step.

Subsequently, the p(NVCL-co-DEGDVE) hydrogel core was deposited using initiated chemical vapor deposition (iCVD) in an in-house built reactor. Deposition of 200 nm p(NVCL-co-DEGDVE) was carried out by in-flowing NVCL (98% stabilized, Sigma Aldrich) at a constant flow rate of 0.275 sccm, DEGDVE cross-linker (99%, Sigma Aldrich) at a flow rate of 0.25 sccm and tert-butyl peroxide (TBPO) initiator (98%, Sigma Aldrich) at a flow rate of 2 sccm into the reactor. The filament temperature was set to 200 °C and the stage/substrate temperature to 35 °C. More details on the reactor can be found elsewhere.[57]

As a last fabrication step the top electrode (TE) was formed by depositing a 50 nm Ag layer on top using e-beam evaporation. The TE has an active area of 1 $cm^2$ for one set of samples. Another set of samples was fabricated with six neighboring TE fields/pixels (electrode active area of 0.25 $mm^2$) spaced 5 mm apart. This design is utilized to test the sensor response to localized force excitations as well as the cross talk between neighboring TE fields/pixels.

*Characterization:* images of the imprint stamp, template layer, nanostructures, ZnO shell and p(NVCL-co-DEGDVE) hydrogel core were obtained with a scanning electron microscope (SEM, part of an e-line system, RAITH GmbH). Cuts for cross-sectional SEM imaging were performed using an ultra-knife (MC 13858, DiATOME) with a knife angle of 45° and cut speed of 1 mm $s^{-1}$. The sensor dielectric properties were measured using an LCR meter (Hioki 3532-50 LCR HiTESTER, Hioki E.E Corporation), in a frequency range of $f$ = 42 Hz to 5 MHz. I-V measurements were performed in the voltage range $V$ = ±20 V using a parameter analyzer (PA1004, MB technology). Sensor response measurements to external force were carried out using an in-house built setup at $F$ = 4, 10, 12, 15 and 20 N. More details on the setup can be found elsewhere.[36] Sensor response measurements to humidity were performed in a commercial environmental chamber (SH-222, ESPEC) at relative humidity $RH$ = 25- 96 % and temperature $T$ = 25 °C and 40 °C. Due to condensation inside the humidity chamber, a relative humidity below 25 % was not obtainable. The generated current was converted into a voltage signal using a transimpedance amplifier (TIA) and recorded with a data acquisition system (SIRIUS Multi, Dewesoft). The charge $Q$ was then calculated from the calibrated V-I signal via numerical integration. The sensor response to temperature was measured using the same setup as used for humidity measurements with a temperature range of $T$ = 50°C - 10°C, at $RH$ = 40 and 96%. Finally, the sensor response to real life stimuli, namely excitation by finger touch and air blown from a human mouth was measured using the Dewesoft data acquisition system, similarly to humidity and temperature response measurements.The data is displayed as a mean value with a standard deviation. The sample size $n$ is indicated in each figure, where applicable.

*FEM simulations:* COMSOL Multiphysics® V5.6 in combination with the Structural Mechanics module was used to model the sensor response to external stimuli, namely, force, humidity and temperature. A multiphysics coupling was applied to account for the piezoelectric effect. A 3D geometry model of only half a single nanorod was used and proper symmetry boundary conditions were applied on the xz-plane of the geometry. Additionally, a periodic boundary condition was applied on the yz-plane to obtain the response over a periodic number of nanorods. The top and bottom electrodes were represented by floating potential and ground boundary conditions, respectively. The hydrogel swelling behavior was modelled following Equation 1 using the hygroscopic swelling node in COMSOL Multiphysics. Laser interferometry was used to obtain the thickness change due to swelling and dependently the data shown in

Table S1. The PUA template was modelled as a linear elastic material and the ZnO shell as piezoelectric material (piezoelectric coupling matrix imported from COMSOL material library, $d_{33}$ = 11.7 pC $N^{-1}$). Force excitations were applied as force per unit area using a boundary load condition.

Additionally, substrate/active layer bending due to applied force in the piezoelectric characterization setup was investigated using a simplified 2D model identical to the experimental setup. It consists of a hard flat stamp with radius $r$ = 2.5 mm getting in contact with and deforming a layer stack comprising the sensor element. In this model, the sensor (active layer) consists of a flat unstructured anisotropic thin film layer with a thickness of 6 µm, poisson's ratio v of the active layer is assumed isotropic (Table 4), on top of a PET substrate with a thickness of 125 µm and a sample support out of rubber with thickness 5 mm, as depicted in Figure 27a. A symmetry line exists at $x$ = 0 mm. All materials were assumed to behave linearly elastic, except for the active layer, for which material's effective elastic properties were first derived from a representative volume element (RVE) based on a unit cell containing a single nanorod. The contact boundary condition was applied to the bottom boundary of the stamp (source) and the top boundary of the thin film/active layer (drain), while the top side of the stamp was successively displaced to obtain a total stamp force $F$ = 0 - 20 N.

### 3.2.7 References


[1] D. De Rossi, F. Carpi and E. P. Scilingo, *Adv. Colloid Interface Sci.*, **2005**, *116*, 165–178.

[2] W. L. Jenkins, *Methods of psychology.*, John Wiley & Sons Inc, Hoboken, NJ, US, **1948**, pp. 250–267.

[3] M. Denda, M. Nakatani, K. Ikeyama, M. Tsutsumi and S. Denda, *Exp. Dermatol.*, **2007**, *16*, 157–161.

[4] D. Filingeri and G. Havenith, *Temperature*, **2015**, *2*, 86–104.

[5] M. L. Hammock, A. Chortos, B. C. K. Tee, J. B. H. Tok and Z. Bao, *Adv. Mater.*, **2013**, *25*, 5997–6038.

[6] X. Wang, L. Dong, H. Zhang, R. Yu, C. Pan and Z. L. Wang, *Adv. Sci.*, **2015**, *2*, 1–21.

[7] J. C. Yang, J. Mun, S. Y. Kwon, S. Park, Z. Bao and S. Park, *Adv. Mater.*, **2019**, *31*, 1904765.

[8] Z. Ma, S. Li, H. Wang, W. Cheng, Y. Li, L. Pan and Y. Shi, *J. Mater. Chem. B*, **2019**, *7*, 173–197.

[9] N. Yogeswaran, W. Dang, W. T. Navaraj, D. Shakthivel, S. Khan, E. O. Polat, S. Gupta, H. Heidari, M. Kaboli, L. Lorenzelli, G. Cheng and R. Dahiya, *Adv. Robot.*, **2015**, *29*, 1359–1373.

[10] W. Chen & X. Yan, *J. Mater. Sci. Techno.*, **2020**, *43*, 175-188.

[11] M. Xie, K. Hisano, M. Zhu, T. Toyoshi, M. Pan, S. Okada, O. Tsutsumi, S. Kawamura and C. Bowen, *Adv. Mater. Techno.,* **2019**, *4*, 1800626.

[12] Z. Li, M. Zhu, J. Shen, Q. Qiu, J. Yu and B. Ding, *Adv. Funct. Mater.*, **2020**, *30*, 1908411.

[13] Q. Li, L. Chen, M. Guo and Z. Hu, *Adv. Mater. Techno.*, **2021**, 2101371.

[14] G. Schwartz, B. C. K. Tee, J. Mei, A. L. Appleton, D. H. Kim, H. Wang and Z. Bao, *Nat. Commun.*, **2013**, *4*, 1859.

[15] B. C. K. Tee, C. Wang, R. Allen and Z. Bao, *Nat. Nanotechnol.*, **2012**, *7*, 825–832.

[16] J. W. Park and J. Jang, *Carbon N. Y.*, **2015**, *87*, 275–281.

[17] T. Q. Trung, L. T. Duy, S. Ramasundaram and N. E. Lee, *Nano Res.*, **2017**, *10*, 2021–2033.

[18] W. Jeong, J. Song, J. Bae, K. R. Nandanapalli and S. Lee, *ACS Appl. Mater. Interfaces*, **2019**, *11, 47*, 44758-44763.

[19] H. Guo, C. Lan, Z. Zhou, P. Sun, D. Wei and C. Li, *Nanoscale*, **2017**, *9*, 6246–6253.

[20] J. H. Oh, S. Y. Hong, H. Park, S. W. Jin, Y. R. Jeong, S. Y. Oh, J. Yun, H. Lee, J. W. Kim and J. S. Ha, *ACS Appl. Mater. Interfaces*, **2018**, *10*, 7263–7270.

[21] Z. Cao, Y. Yang, Y. Zheng, W. Wu, F. Xu, R. Wang and J. Sun, *J. Mater. Chem. A*, **2019**, *7*, 25314–25323.

[22] G. Liu, Q. Tan, H. Kou, L. Zhang, J. Wang, W. Lv, H. Dong and J. Xiong, *Sensors,* **2018**, *18(5)*, 1400.

[23] Y. Chen, B. Lu, Y. Chen and X. Feng, *Sci. Rep.*, **2015**, *5*, 1–11.

[24] M. Khatib, O. Zohar, W. Saliba and H. Haick, *Adv. Mater.*, **2020**, *32*, 2000246.

[25] H. Liu, H. Xiang, Y. Wang, Z. Li, L. Qian, P. Li, Y. Ma, H. Zhou and W. Huang, *ACS Appl. Mater. Interfaces*, **2019**, *11*, 40613–40619.

[26] J. Kim, M. Lee, H. J. Shim, R. Ghaffari, H. R. Cho, D. Son, Y. H. Jung, M. Soh, C. Choi, S. Jung, K. Chu, D. Jeon, S. T. Lee, J. H. Kim, S. H. Choi, T. Hyeon and D. H. Kim, *Nat.*

*Commun.*, **2014**, *5*, 5747.

[27] L. Wang, J. A. Jackman, E. L. Tan, J. H. Park, M. G. Potroz, E. T. Hwang and N. J. Cho, *Nano Energy*, **2017**, *36*, 38–45.

[28] X. Zhao, Y. Long, T. Yang, J. Li and H. Zhu, *ACS Appl. Mater. Interfaces*, **2017**, *9*, 30171–30176.

[29] L. Zhu, Y. Wang, D. Mei, W. Ding, C. Jiang and Y. Lu, *ACS Appl. Mater. Interfaces*, **2020**, *12*, 31725–31737.

[30] D. H. Ho, Q. Sun, S. Y. Kim, J. T. Han, D. H. Kim and J. H. Cho, *Adv. Mater.*, **2016**, *28*, 2601–2608.

[31] S. Han, N. U. H. Alvi, L. Granlöf, H. Granberg, M. Berggren, S. Fabiano and X. Crispin, *Adv. Sci.*, **2019**, *6*, 1802128.

[32] B. Lee, A. Jiao, S. Yu, J. B. You, D. H. Kim and S. G. Im, *Acta Biomater.*, **2013**, *9*, 7691–7698.

[33] F. Muralter, A. Perrotta, O. Werzer and A. M. Coclite, *Macromolecules*, **2019**, *52*, 6817–6824.

[34] L. Yicheng, N. W. Emanetoglu and Y. Chen, *Zinc Oxide Bulk, Thin Films and Nanostructures*, Elsevier Science Ltd, **2006**, pp. 443– 489.

[35] D. Bremecker, P. Keil, M. Gehringer, D. Isaia, J. Rödel and T. Frömlng, *J. Appl. Physics*, **2020**, *127*, 034101.

[36] T. Abu Ali, J. Pilz, P. Schäffner, M. Kratzer, C. Teichert, B. Stadlober and A. M. Coclite, *Phys. Status Solidi Appl. Mater. Sci.*, **2020**, *217*, 1–6.

[37] J. Rao, Z. Chen, D. Zhao, R. Ma, W. Yi, C. Zhang, D. Liu, X. Chen, Y. Yang, X. Wang, J. Wang, Y. Yin, X. Wang, G. Yang and F. Yi, *Nano Energy*, **2020**, *75*.

[38] G. Ozaydin-Ince and K. K. Gleason, *Chem. Vap. Depos.*, **2010**, *16*, 100–105.

[39] K. Tapily, D. Stegall, D. Gu, H. Baumgart, G. Namkoong and A. Elmustafa, *ECS Trans.*, **2009**, *25(4)*, 85–92.

[40] H. Kim, U. S. Jung, S. I. Kim, D. Yoon, H. Cheong, C. W. Lee and S. W. Lee, *Current Appl. Physics*, **2014**, *14(2)*, 166–170.

[41] C. Zhimin, L. Xinchun and H. Dannong*, Surface and Coatings Techno.,* **2012***, 207,* 361-366.

[42] C. Y. Yen, S. R. Jian, G. J. Chen, C. M. Lin, H. Y. Lee, W. C. Ke, Y. Y. Liao, P. F. Yang, C. T. Wang, Y. S Lai, J. S. C. Jang, and J. Y. Juang, *Appl. Surface Sci.*, **2011**, *257(17)*, 7900–7905.

[43] K. Tapily, D. Gu, H. Baumgart, G. Namkoong, D. Stegall and A. A. Elmustafa, *Semiconductor Sci. and Techno.*, **2011**, *26(11)*.

[44] L. Zhu, *J. Physical Chem. Letters,* **2014***, 5*, 3677–3687.

[45] M. Füllbrandt, E. Ermilova, A. Asadujjaman, R. Hölzel, F. F. Bier, R. von Klitzing and A. Schönhals, *J. of Physical Chem B*, **2014**, *118*(13), 3750–3759.

[46] F. Biryan, A. M. Abubakar and K, Demirelli, *Thermochimica Acta,* **2018***, 669*, 66–79.

[47] J. Pilz, A. Perrotta, P. Christian, M. Tazreiter, R. Resel, G. Leising, T. Griesser and A. M. Coclite, *J. Vac. Sci. Technol. A Vacuum, Surfaces, Film.*, **2018**, *36(1)*, 01A109.

[48] J. Pilz, A. Perrotta, G. Leising and A. M. Coclite, *Phys. Status Solidi*, **2020**, *217,* 1900256.

[49] M. Laurenti, S. Stassi, M. Lorenzoni, M. Fontana, G. Canavese, V. Cauda and C. F. Pirri, *Nanotechnology*, **2015**, *26*, 215704.

[50] N. J. Blumenstein, F. Streb, S. Walheim, T. Schimmel, Z. Burghard and J. Bill, *Beilstein J. Nanotechnol.*, **2017**, *8*, 296–303.

[51] S. J. Kang and Y. H. Joung, *Appl. Surf. Sci.*, **2007**, *253*, 7330–7335.

[52] X. Yan, W. Ren, H. Xin, P. Shi, X. Chen and X. Wu, *Ceram. Int.*, **2013**, *39*, 583–586.

[53] G. J. T. Leighton and Z. Huang, *Smart Mater. Struct.*, **2010**, *19(6)*, 065011.

[54] S. Kozanoğlu, T. Özdemir and A. Usanmaz, *J. Macromolecular Sci.*, **2011**, *48*(6), 467–477.

[55] F. Muralter, F. Greco and A. M. Coclite, *ACS Appl. Polym. Mater.*, **2020**, *2*, 1160–1168.

[56] S. Park, H. Kim, M. Vosgueritchian, S. Cheon, H. Kim, J. H. Koo, T. R. Kim, S. Lee, Schwartz, H. Chang and Z. Bao, *Adv. Mater.*, **2014**, *26(43)*, 7324–7332.

[57] F. Muralter, A. Perrotta and A. M. Coclite, *Macromolecules*, **2018**, *51(23)*, 9692-9699.

[58] S. H. Ahn and L. J. Guo, *ACS Nano*, **2009**, *3(8)*, 2304– 2310.

### 3.2.8 Acknowledgements

This project has received funding from the European Research Council (ERC) under the European Union's Horizon 2020 research and innovation program (Grant Agreement No. 715403).

We thank STRATEC Consumables GmbH and Fianostics GmbH for providing the COC master. In addition, we acknowledge Marlene Anzengruber for the hydrogel swelling measurements.

### 3.2.9 Supporting Information

**Supporting note 1: Dielectric characterization**

To validate the measured results, the overall ε' of the sensor (without and with a hydrogel core) is calculated following **Equation 52** and **Equation 53** (capacitors in series). For simplification, the overall dielectric constant is calculated by assuming a planar geometry of three layers with thicknesses $d_{PUA}$ = 6 µm, $d_{ZnO}$ = 50 nm and $d_{NVCL}$ = 200 nm, leading to a series capacitance:

$$C = \varepsilon' \varepsilon_0 \frac{A}{d} \tag{52}$$

and

$$\frac{1}{C} = \frac{1}{C_{PUA}} + \frac{1}{C_{ZnO}} + \frac{1}{C_{NVCL}} \tag{53}$$

where $C$ is the capacitance, $\boldsymbol{\varepsilon'}$ is the overall dielectric constant, $\varepsilon_0$ is the vacuum permittivity, $A$ is the active area and $d$ is the total dielectric layer thickness. Assuming $\boldsymbol{\varepsilon'}_{PUA}$ = 5 (measured at 1 kHz), $\boldsymbol{\varepsilon'}_{ZnO}$ = 8.5 (value adopted from COMSOL materials library) and $\boldsymbol{\varepsilon'}_{NVCL}$ = 3 (value adopted from reference 46), results in $\boldsymbol{\varepsilon'}$ of 5 and 4.7 for a sensor without and with a hydrogel core, respectively. When compared to the experimental data, a reverse trend is observed (see Figure 20a). In the calculation, the dielectric constant of the dry-state hydrogel is used. However, water molecules present within the hydrogel mesh increase the overall experimentally measured $\boldsymbol{\varepsilon'}$. Additionally, the assumption of a planar geometry (nanostructures not accounted for) is more comparable to experimental value when the hydrogel layer is excluded.

**Supporting information figures**

**Figure 25a** shows an image of the polymeric stamp used to structure the PUA template, where the nanostructures have an aspect ratio of 1 ($d$ = 500 nm and $H$ = 500 nm), as shown in the SEM image (**Figure 25b**). **Figure 25c** shows a cross-sectional SEM image of the patterned PUA template (prior to filling). A thickness of 6 µm is achieved with force $F$ = 30 N applied on the stamp for 30 minutes during the imprint process (nanoholes not visible).

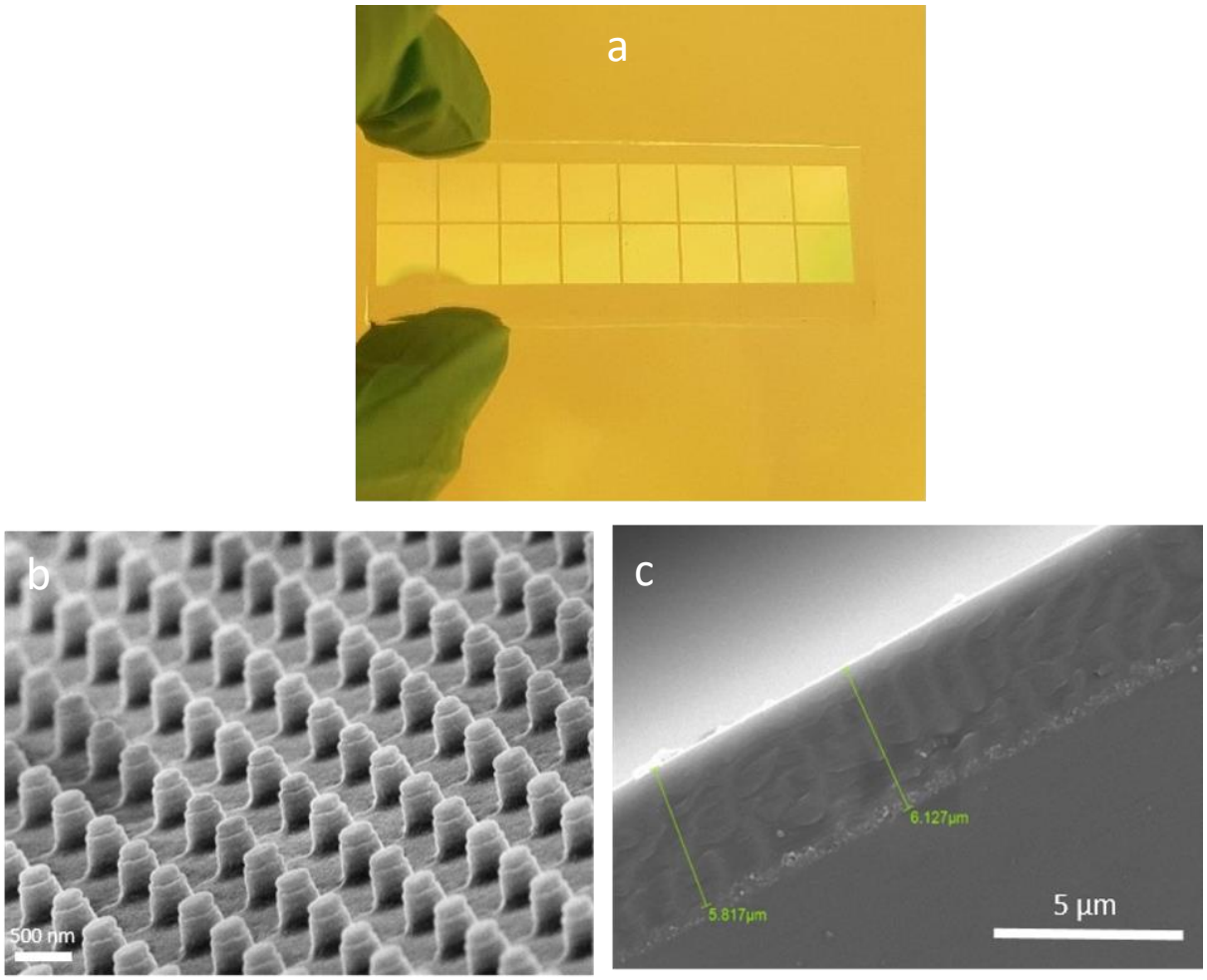


Figure 25. a) Image of the stamp used in the UV-NIL process. b) SEM image of the stamp, showing nanostructures with an aspect ratio of 1. The nanostructures have a diameter and height of 500 nm. c) Cross-sectional SEM image of the PUA layer after imprinting and curing, revealing a nominal thickness of 6 µm (nanoholes are not visible)

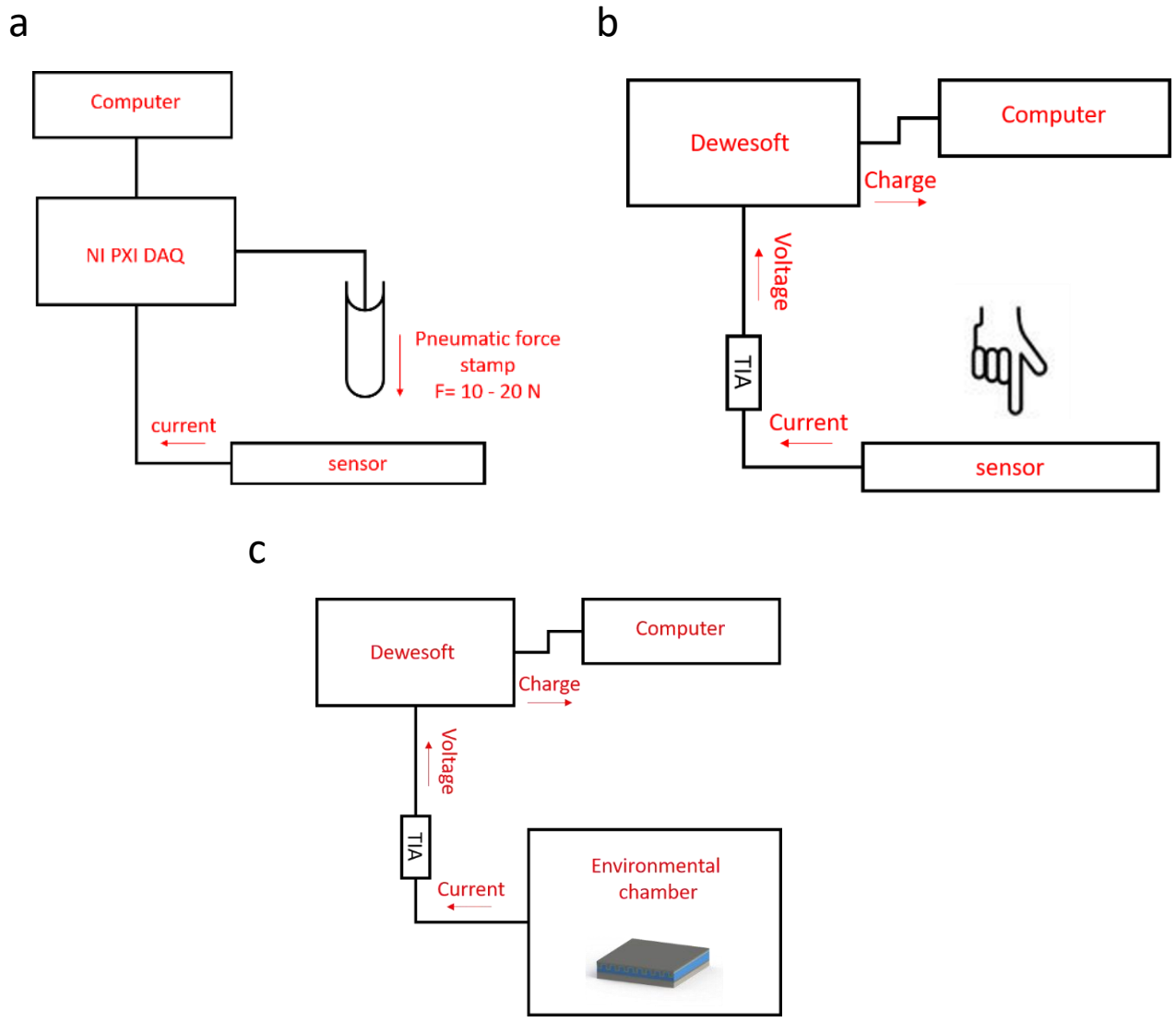


Figure 26. Schematics of a) the piezoelectric characterization setup used to measure data displayed in Figure 21, where a pneumatic rigid force stamp with a rounded tip ($d$ = 5 mm) is used to apply a step force signal up to 20 N in magnitude. The generated current is recorded using a NI PXI data acquisition system. b) Setup used to measure sensor response to force excitation by a human finger, where the generated current is converted and amplified into voltage using a TIA. The amplified signal is recorded using a Dewesoft DAQ, where the charge $Q$ is calculated by numerical integration. c) Setup used to measure sensor response to humidity and temperature (results displayed in Figure 23 and 24)

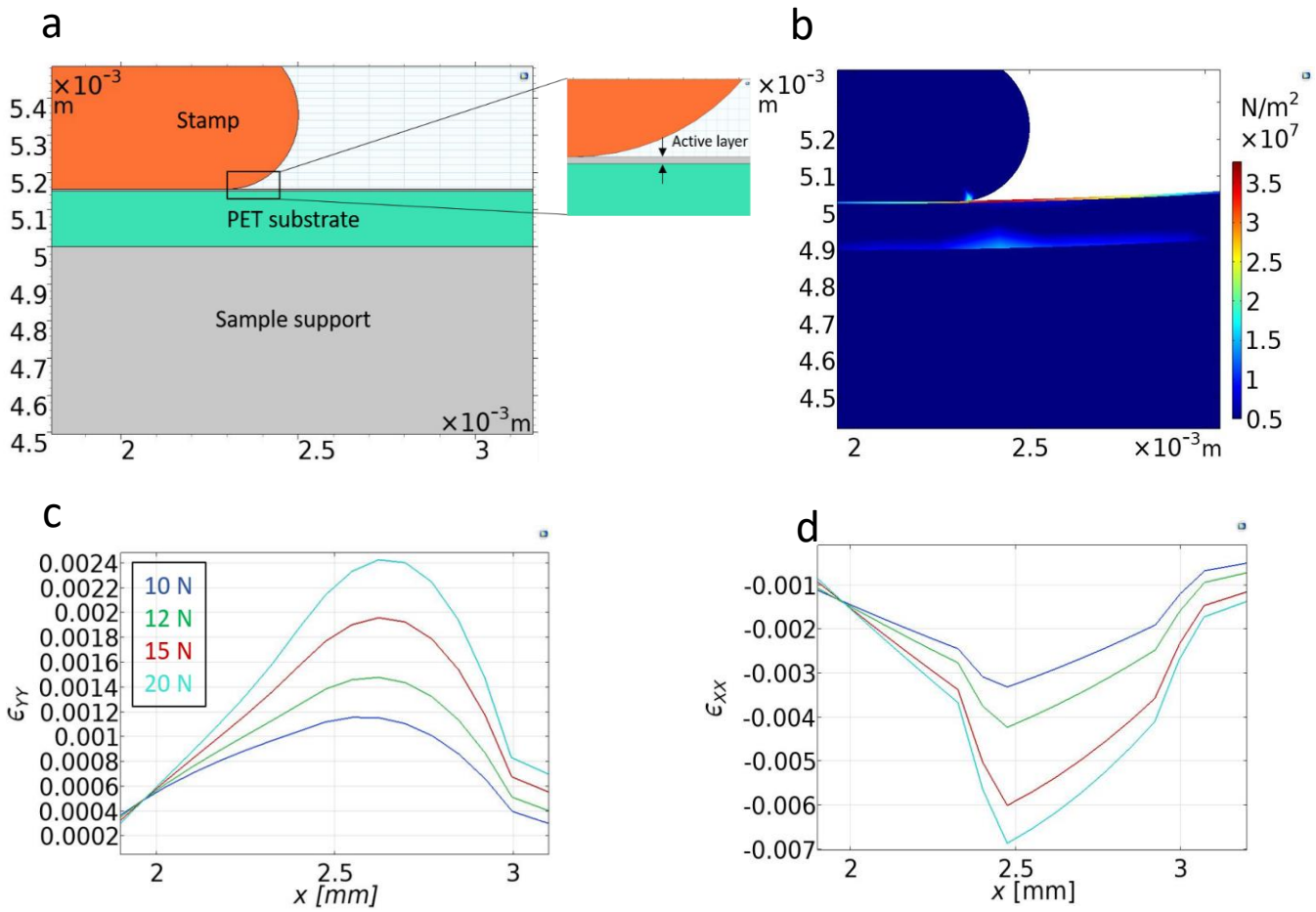


Figure 27. Simulated sensor bending during normal force excitation on a soft underground. a) 2D geometry model showing a solid stamp in contact with the thin film/active layer. The flat unstructured active layer represents a series of adjacent active nanorods with an effective elasticity matrix $[\bar{E}^M]$, given in Table 4, calculated from a RVE that consists of a unit cell with a single core-shell nanorod. The active layer has a thickness of 6 µm, while the PET substrate has a thickness of 125 µm. As in the experimental setup, a rubber sample support with a thickness of 5 mm was included in the model. b) Calculated von Mises stress within the active layer at $F$ = 10 N, which clearly indicates maximum stress being applied in the vicinity of the stamp edge ($3.5 \times 10^7$ N m$^{-2}$). c,d) Local strain components $\epsilon_{YY}$ (c) and $\epsilon_{XX}$ (d) in the active layer for different forces (10, 12, 15 and 20 N). The elastic substrate and soft sample support cause a strong deformation near the edge of the stamp ($x \approx 2.5$ mm). In the vicinity of the stamp edge the soft support causes a strong bending of the substrate, which introduces a compressive in-plane strain ($\epsilon_{XX} < 0$) and a tensile out-of-plane strain ($\epsilon_{YY} > 0$). The strain levels in this region dominate over those in the region right below the flat face of the stamp ($x < 2$ mm) and primarily contribute to the piezoelectric response under force excitation

**Figure 28** shows the generated charge *Q* from different electrode pixels/fields (design shown in Figure 22a) for step force excitations with a magnitude of 4 N and 10 N. To better understand how the final imprint layer thickness is related to the imprint pressure, we refer to the squeeze model of a Newtonian fluid, described as:[58]

$$t = \frac{\mu a^2}{2P}\left(\frac{1}{h_f^2} - \frac{1}{h_0^2}\right) \tag{54}$$

Where *t* is the time needed to reach final imprint layer thickness $h_f$, $h_0$ is the initial imprint layer thickness, *a* is the contacting length, *P* is the pressure and *μ* is the dynamic viscosity of the liquid uncured resin. The final imprint layer thickness is dependent on the initial thickness as well as the contact pressure, which is not applied uniformly, since the imprinting is performed by hand. Therefore, it is expected that the final film thickness varies along the PUA imprint layer due to uneven pressure distribution during the imprint process. Since the thickness influences the dielectric and micromechanic behavior of the local nanorods, this in turn affects the response of the individual pixel elements, each integrating over the response of hundreds of nanorods.

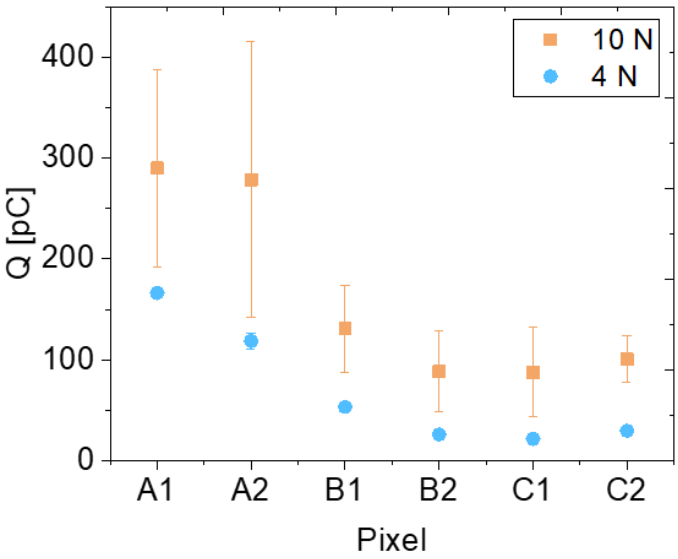


Figure 28. Piezoelectric charge response of each electrode pixel to force *F* = 4 N and 10 N. The variation in response from an individual bar (represented by error bar) is calculated from measurements performed on two sensors with the design shown in Figure 22a

## Supporting information tables

Table 3. Swelling coefficient β and moisture concentration in air Cmo of p(NVCL-co-DEGDVE) 25% nominally cross-linked at 10, 25, 35, 40 and 50 °C for RH = 20 – 95 % used in the FEM model of a single nanorod

| RH [%] | $C_{mo}$ (10 °C) [kg m$^3$] | β (10 °C) [m$^3$ kg$^{-1}$] | $C_{mo}$ (25 °C) [kg m$^3$] | β (25 °C) [m$^3$ kg$^{-1}$] | $C_{mo}$ (35 °C) [kg m$^3$] | β (35 °C) [m$^3$ kg$^{-1}$] | $C_{mo}$ (40 °C) [kg m$^3$] | β (40 °C] [m$^3$ kg$^{-1}$] | $C_{mo}$ (50 °C) [kg m$^3$] | β (50 °C) [m$^3$ kg$^{-1}$] |
|---|---|---|---|---|---|---|---|---|---|---|
| 20 | 0.002 | - | 0.005 | 0.3 | 0.008 | - | 0.01 | 0.1 | 0.02 | - |
| 30 | 0.003 | - | 0.007 | 0.35 | 0.012 | 0.1 | 0.015 | 0.2 | 0.025 | 0.1 |
| 40 | 0.004 | 0.4 | 0.009 | 0.4 | 0.015 | 0.15 | 0.02 | 0.3 | 0.033 | 0.2 |
| 50 | 0.006 | 1 | 0.01 | 0.6 | 0.02 | 0.3 | 0.025 | 0.4 | 0.04 | 0.3 |
| 60 | 0.0065 | 2 | 0.013 | 1 | 0.023 | 0.4 | 0.03 | 0.6 | 0.05 | 0.5 |
| 70 | 0.007 | 4.2 | 0.016 | 2.1 | 0.027 | 0.7 | 0.035 | 0.8 | 0.06 | 0.6 |
| 80 | 0.0075 | 6.1 | 0.018 | 4.1 | 0.03 | 1.3 | 0.04 | 1 | 0.066 | 0.7 |
| 90 | 0.008 | 26.4 | 0.02 | 9.5 | 0.035 | 3.7 | 0.045 | 2.3 | 0.075 | 1.5 |
| 95 | 0.009 | 28.6 | 0.021 | 10 | 0.037 | 4.7 | 0.05 | 2.6 | 0.08 | 1.7 |

Table 4. Elasticity matrix and Young's modulus of different materials used in FEM model of substrate bending

| Component | Description | Symbol | Value |
|---|---|---|---|
| Active layer | Elasticity matrix | $[\bar{E}^M]$ | $\begin{pmatrix} 1.1\,x\,10^{10} & 5.0\,x\,10^{9} & 3.4\,x\,10^{7} & 1.8\,x\,10^{5} & -320.0 & -810.0 \\ 5.0\,x\,10^{9} & 1.1\,x\,10^{10} & 3.4\,x\,10^{7} & 1.8\,x\,10^{5} & -574.0 & -458.0 \\ 3.4\,x\,10^{7} & 3.4\,x\,10^{7} & 5.4\,x\,10^{7} & -826.0 & 186.0 & 99.0 \\ -1.8\,x\,10^{5} & 5.7\,x\,10^{5} & -826 & 3.1\,x\,10^{9} & 197.0 & -77.2 \\ -320.0 & -574.0 & 186.0 & 197.0 & 1.7\,x\,10^{7} & -320.0 \\ -810.0 & -458 & 99.0 & -77.2 & -320.0 & 1.7\,x\,10^{7} \end{pmatrix}$ Pa |
| | Poisson's ratio | $v$ | 0.3 |
| Substrate | Young's modulus | $E_{sub}$ | 2.8 GPa |
| | Poisson's ratio | $v_{sub}$ | 0.4 |
| Sample support | Young's modulus | $E_{SS}$ | 1.45 MPa |
| | Poisson's ratio | $v_{SS}$ | 0.49 |
| Stamp | Young's modulus | $E_{stamp}$ | 200 GPa |
| | Poisson's ratio | $v_{stamp}$ | 0.27 |

## 3.3 Enhancement of the sensing performance in multi-stimuli responsive hybrid materials

Taher Abu Ali[1,2], Marlene Anzengruber[1], Katrin Unger[1], Barbara Stadlober[2], Anna Maria Coclite[1*]

1 Graz University of Technology, NAWI Graz, Institute of Solid State Physics, 8010 Graz, Austria

2 Joanneum Research Forschungsgesellschaft mbH, MATERIALS – Institute for Surface Technologies and Photonics, 8160 Weiz, Austria

### 3.3.1 Preface

The work presented in this publication was conducted at Graz University of Technology in cooperation with Joanneum Research. Taher Abu Ali and Marlene Anzengruber prepared the samples, performed the measurements and wrote the manuscript. Katrin Unger helped with the data evaluation. Barbara Stadlober and Anna Maria Coclite supervised the work. The published article is reproduced identical in text and illustrations with permission from publisher.

### 3.3.2 Abstract

Capturing environmental stimuli is an essential aspect of electronic skin applications in robotics and prosthetics. Sensors made of temperature and humidity responsive hydrogel and piezoelectric zinc oxide (ZnO) core-shell nanorods have shown the necessary sensitivity. This is achieved by using highly conformal and substrate independent deposition methods for the ZnO and the hydrogel, i.e. plasma enhanced atomic layer deposition (PEALD) and initiated chemical vapor deposition (iCVD). In this work we demonstrate that the use of a multi-chamber reactor enables performing PEALD and iCVD, sequentially, without breaking the vacuum. The sequential deposition of uniform as well as conformal thin films responsive to force, temperature and humidity improved the deposition time and quality significantly. Proper interlayer adhesion could be achieved via in situ interface activation, a procedure only realizable in this unique multi-chamber reactor. Beyond the fabrication method, also the mechanical properties of the template used to embed the core-shell nanorods and the cross-linker density in the hydrogel were optimized following the results of finite element models. Consequently, the core-shell nanorod structures showed a response of 550 pC to a force as high as 15 N over several compression cycles and maximum sensitivity to humidity of 34 pC $\%^{-}$

[1] and to temperature of 200 pC °C$^{-1}$. Finally, preliminary galvanostatic electrochemical impedance spectroscopy measurements were performed as a base for local signal readout, temperature and humidity cross-talk minimization and possibly distinction between different stimuli.

### 3.3.3 Introduction

The performance of sensor materials is commonly evaluated by their response towards external stimuli - a large amplitude and a fast response upon excitation are desirable. Lately, hydrogels have attracted growing interest for the integration in smart materials due to their unique properties.[1–6] Hydrogels are three dimensional polymer networks with the ability to incorporate water into their structure and even double or triple their initial volume when immersed in water.[7,8] Stimuli responsive hydrogels exhibit significant change in their properties when exposed to an external stimulus like humidity, temperature, light,[9] pH,[10] or magnetic and electric field.[11] For temperature responsive hydrogels a lower critical solution temperature (LCST) can be observed.[12] At this temperature, a phase change takes place and the hydrogel network collapses from its expanded state into a globule state as the temperature is increased.[13] Hydrogels based on biocompatible polymers with an LCST in the physiological temperature range are of particular interest for applications in tissue engineering,[14,15] biotechnology[16] or wearable electronics.[17] The strong signal stemming from the sharp LCST transition can be easily detected and with the use of smart architectures converted into an electrical output.

In a previous work, we successfully combined a piezoelectric semiconductor material, namely zinc oxide (ZnO), and a multi-stimuli responsive hydrogel, namely poly(N-vinylcaprolactam-co-di(ethyleneglycol) divinyl ether) or p(NVCL-co-DEGDVE) in core-shell nanorod structures capable of detecting force, humidity and temperature. As depicted in **Figure 29a**, the stimuli detection is achieved through measuring the piezoelectric current generated upon deformation of the ZnO shell due to the hydrogel core swelling in response to humidity (max sensitivity $S_H$ = 1.2 nC $\%^{-1}$ to relative humidity (RH) in the range of 85 – 96% at 25°C) and temperature (max $S_T$ = 0.14 nC $°C^{-1}$ response in the range 30 – 50°C at 96% RH).[17] Additionally, the piezoelectric properties of ZnO allow direct detection of the applied force (max $S_F$ = 36 pC $N^{-1}$), with site-specific force sensing and a resolution down to 0.25 $mm^2$.[17] The fabrication of such core-shell nanorod structures requires a deposition process able to operate at low temperatures due to the fragile nature of the hydrogel and of the template material. Additionally, highly conformal thin films are required for the realization of a nanostructured geometry. Initiated chemical vapor deposition (iCVD) is an ideal deposition method for polymer thin films due to its substrate independence and the wide range of possible reactants. Under certain conditions, the conformality of the process allows for the low temperature deposition of high quality polymer films even on substrates with complex geometries.[17,18]

For the deposition of metal oxides, plasma enhanced atomic layer deposition (PEALD) is considered the gold standard in conformal coating. PEALD can be operated at low temperatures since the reactions are plasma-driven instead of thermally activated.[19,20] This makes PEALD the perfect candidate for coating sensitive substrates. Combined with iCVD the

fabrication of uniform and conformal high quality hybrid thin films can be realized. Until now, the fabrication of a thin film consisting of one layer deposited via PEALD and a second deposited via iCVD was only possible with the consecutive layer fabrication in two separate reactors. This is a rather lengthy process and since the interface between the two layers is exposed to ambient conditions during the transfer from one chamber to the other, contamination can be expected to some extent. A combination of both deposition systems in a single multi-chamber reactor would therefore hold benefits like the reduction of overall deposition time and the simultaneous improvement of the multilayer quality.

The main aim of this work is to show the deposition of structured core-shell thin films in a one-of-a-kind multi-chamber reactor combining PEALD and iCVD and show the advantages of interface optimization on the sensing properties. Additionally, the work presents steps towards performance enhancement, namely, the influence of the template material mechanical properties and the p(NVCL-co-DEGDVE) cross-linker (CL) fraction. Finally, characterization with varying humidity and temperature using galvanostatic electrochemical impedance spectroscopy (GEIS) is presented as a method for signal readout, temperature and humidity cross-talk minimization.

### 3.3.4 Experimental

#### Sensor fabrication

Multi-stimuli responsive nanostructured multilayer thin films were fabricated using a custom-built reactor consisting of a PEALD chamber connected via transfer chamber to an iCVD chamber, as shown in **Figure 29b**. This enables the deposition of 200 nm of p(NVCL-co-DEGDVE) on top of the 50 nm of ZnO layer without breaking the vacuum. To realize such films, two resins, with different mechanical properties (Young's modulus, $E_{hard}$ = 2 GPa and $E_{soft}$ = 200 MPa ), based on polyurethane acrylate (PUA, NILcure™, Joanneum Research) were nanostructured on top of aluminum (Al) coated polyethylene terephthalate (PET) substrate (50 µm, Hueck Folien, Austria) or indium tin oxide (ITO, 100 nm, $R_s$ = 60 Ω $sq^{-1}$) coated PET substrate (Sigma Aldrich, Germany), by UV nanoimprint lithography (UV-NIL). Al or ITO served as a bottom electrode (BE). Two types of electrodes were used in order to test the stability of our UV-NIL approach. The resultant nanotrenches had a diameter $d$ = 500 nm, height $H$ = 500 nm, aspect ratio $AR$ = 1 and a pitch = 1000 nm and were arranged in 16 square fields each with dimensions of 8 × 8 mm. More details on the setup can be found elsewhere.[17] The samples were then placed in the transfer chamber, with the vacuum maintained at ≈ 20 µbar, and transferred into the PEALD chamber for the first deposition step.

The stainless steel PEALD chamber had a volume of 5.28 L with an inner diameter of 100 mm and a height of 137.8 mm. Via a stainless-steel transfer boat (70 x 70 mm), the samples were placed on the heated (35°C) sample stage, made from pyrolytic boron nitride (Boratec). The distance between the ground and the RF top electrode was 78 mm. A gate valve (VAT,

Switzerland) regulated the sample transfer between the two chambers. A two-stage rotary vane pump (DUO 20 Pfeiffer Vacuum) and a turbopump (Pfeiffer Vacuum, Germany) maintained a working pressure of 200 µbar and were connected to the PEALD chamber where the pressure was controlled via a butterfly throttle valve (MKS Instruments, USA). Further, a Baratron Type 626 pressure transducer and a PDR2000 (MKS Instruments, USA) were employed for the readout. Purging gas and co-reactant flows were controlled via the GE50A mass flow controller (MKS Instruments, USA). 60 W plasma was generated via the Cesar RF power generator (Advanced Energy, USA). The deposition recipe was an adapted version of the parameters previously optimized in our group.[21,22] A 0.15s pulse, controlled via an ALD valve (Swagelock ALD3, USA), introduced Diethylzinc (DEZ, Sigma Aldrich, USA) into the chamber. The deposition process consisted of four steps: 15s $O_2$ plasma dose, 15s Argon purge, DEZ dose and a second 15s Argon purge. The desired thickness was reached after 250 cycles, and the deposition was finalized with a plasma step to activate the surface for the following deposition. After evacuation of the transfer chamber, the sample was transported to the iCVD chamber without breaking the vacuum for the second deposition step.

The volume of the iCVD chamber was 3.15 L. A recirculating chiller (Polar Series 500 LC, Thermo Scientific, USA) was connected to the aluminum sample stage (d = 85 mm, H = 35 mm). A two-stage rotary vane pump (DUO 20, Pfeiffer Vacuum, Germany) protected via zeolite filter (Molecular Sieve Foreline Trap, Kurt J. Lesker Company, USA) was connected to the reactor. The chamber pressure was monitored via a pressure controller (600 Series, MKS Instruments, USA) and regulated via a butterfly throttle valve (MKS Instruments, USA) and a manual valve (XLH, High Vacuum Manual Angle Valve, SMC, Japan). Between monomer inlet and sample stage, a perforated diffuser plate was installed to ensure homogeneous gas mixing. The filament inside the chamber was heated resistively by a low voltage power supply (PTN 350-5, Heinzinger, Germany) to 200°C.

p(NVCL-co-DEGDVE) thin films were deposited directly on the ZnO layer. N-vinylcaprolactam (NVCL, Sigma Aldrich, 98% purity, USA) was used as a monomer, di(ethylene glycol) divinyl ether (DEGDVE, Sigma-Aldrich, 99% purity, USA) as a cross-linker and tert-butyl peroxide (TBPO, Sigma-Aldrich, 98% purity, USA) as an initiator. All chemicals were used without further purification. The monomer and cross-linker jars were heated to 85°C and 70°C, respectively and line heating of 90°C, whilst the initiator jar and line remained at room temperature. Flow rates of 0.1 ± 0.05 sccm for NVCL, 0.2 ± 0.10 sccm for DEGDVE and 0.9 ± 0.05 sccm for TBPO resulted in the formation of stable and highly responsive hydrogel thin films with ≈ 25 and 35% nominal cross-linking. The deposition was run at a working pressure of 466 µbar. A laser interferometry setup consisting of a self-contained HeNe laser ($\lambda$ = 632.8 nm, HNLS008L-EC, THORLABS, USA) and an energy meter (PM100USB, THORLABS, USA) was used for thickness monitoring of the hydrogel layer grown on a Si(100) wafer, which was

positioned next to the structured template inside the reactor chamber. After the hydrogel deposition was completed, the samples were removed from the reactor. Silver (Ag, 50 nm), serving as a top electrode (TE), was deposited via e-beam evaporation with a deposition rate between 0.1 and 0.2 nm $s^{-1}$. Using a stainless-steel shadow mask, eight neighboring Ag electrode fields were deposited, each with an active area of 6 x 6 mm.

**Characterization**

The nanostructured samples were investigated for conformality via atomic force microscopy (AFM) performed by a Nanosurf Easyscan 2 with NANOSENSORS scanning probe (model PPP-NCLR-20). The topography of semi-filled nanostructures and template material was recorded.

The piezoelectric response of the nanostructured multilayer samples was investigated in an in-house built setup with a step force-signal $F$ = 10, 12 and 15 N and frequency $f$ = 0.5 Hz. A detailed description of the setup can be found elsewhere.[17,19]

The generated charge to $RH$ = 35- 95% at temperature $T$ = 25 and 40°C, as well as the generated charge to temperature range of $T$ = 10 - 50°C, at RH = 40 and 85% was measured in a climate chamber (Espec SH222, interior volume 22 L, Japan) with a data acquisition system (DAQ, SIRIUS Multi, Dewesoft). More details on the set up can be found elsewhere.[19] Additionally, an alternative custom-built setup, which varies the relative humidity from 5 to 75% by mixing $N_2$ bubbled through water and pure $N_2$ via needle valves was used, with such measurements performed at room temperature. For comparison with the simulated data and our previous work, the charge density $\sigma$ was calculated by normalizing the charge to the electrode area.

The humidity and temperature response of the samples was investigated via galvanostatic electrochemical impedance spectroscopy (GEIS) executed with a two-electrode setup (Gamry 6000 Reference, USA) inside the same climate chamber. Measurements were performed within a frequency range $f$ = 200-1500 Hz, where the AC current is set to 1 x $10^{-7}$ A and at three different temperatures: 10, 23 and 35°C. The relative humidity was raised from 30 to 95% for each temperature. The set points were controlled via Python scripts where an accuracy of ± 0.2 °C and ± 1 % for temperature and RH respectively, was defined.

**FEM simulations**

COMSOL multiphysics v5.6 was utilized to perform an optimization study on the nanostructured multilayer thin films response to force, humidity and temperature, using the piezoelectric multiphysics obtained from coupling of the solid mechanics and electrostatics modules. To that, a 3D model was developed to model the influence of the template material rigidity, namely the young's modulus $E$ and the influence of the hydrogel CL % The geometry used within the 3D model is depicted in **Figure 35**. A 3D model of a cross-sectional single nanorod ($d_{nanotrench}$ = 500 nm, height $H$ = 500 nm, pitch = 1000 nm, $t_{ZnO}$ = 50 nm and $t_{hydrogel}$ =

200 nm) was used and multiple boundary conditions were applied- starting with a symmetry boundary condition applied to the front xz-plane and a periodic boundary condition applied to both yz-planes of the geometry. The hydrogel core was assigned as a hygroscopic material and the swelling behavior in response to humidity (*RH* = 20, 30, 50, 60, 70, 80, 90 and 95%) and temperature (*T* = 10, 25, 35 and 50°C) was modelled following **Equation 55**. Laser interferometry was used to obtain the thickness change due to swelling and dependently the data shown in **Table 5** and **6**. The zinc oxide shell, assumed as single crystalline with 100 orientation, was assigned as a piezoelectric material following **Equation 56** to **58**. Additionally, the PUA polymeric template was assigned as a linear elastic material, with $E_{soft,sim}$ = 200 MPa representing a soft polymeric template vs $E_{hard,sim}$ = 2 GPa representing a hard polymeric template. A list of the material properties required for the model are given in **Table 7**. The top and bottom electrodes where simulated as floating and ground boundary conditions, respectively. Finally, a boundary load condition was applied to the top xy-plane of the geometry to simulate the input force *F* = 10, 12, 15 and 20 N.

### 3.3.5 Results and discussion

**Morphological characterization:**

The fabrication steps elaborated in the experimental section are shown in **Figure 29c**. The resultant device, prior to the deposition of the TE, is shown in **Figure 29d**. Kapton tape is applied to cover parts of the BE. This is crucial to inhibit the deposition of any material on the covered BE regions. For electrical characterization, the Kapton tape is removed, exposing clean Al or ITO surface for contacting.

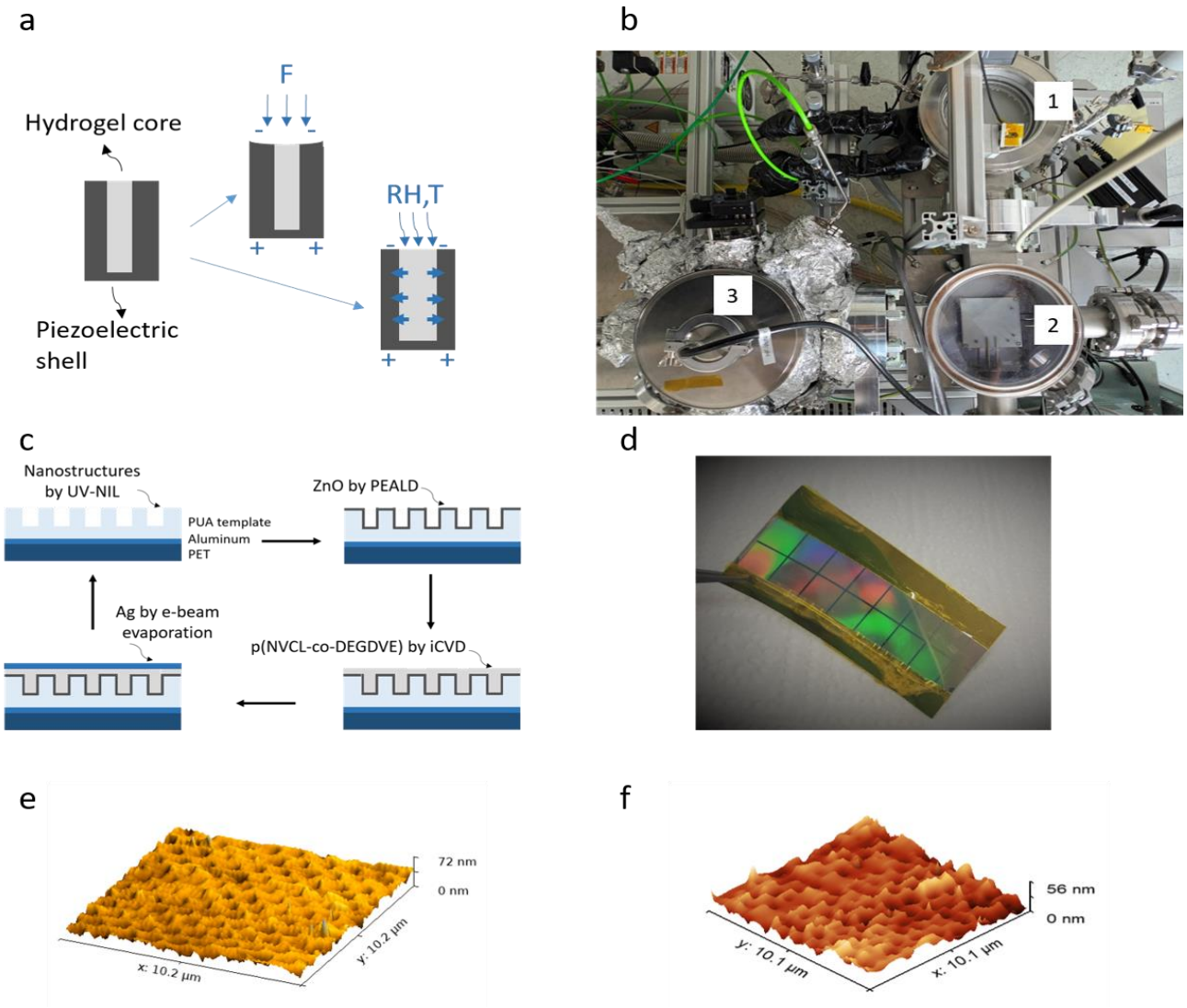


Figure 29. a) Schematics of a multi-stimuli responsive core-shell nanorod explaining the detection concept and responsiveness to force (directly sensed by ZnO shell), humidity and temperature (swelling of p(NVCL-co-DEGDVE) core is translated to piezoelectric response through stress/strain). b) Combined reactor, which consists of 1. iCVD reactor, 2. Transfer chamber, 3. PEALD reactor. c) Multi-stimuli responsive nanostructured sensors fabrication steps. Dimensions are not indicated to scale. d) An image of the sample prior to deposition of Ag TE, with aluminum BE and a hydrogel with 35% cross-linker fraction. The colors come from the diffraction grating in the visible spectrum. e) 3D AFM topography image of nanostructured PUA template prior to filling, clearly showing periodic nanotrenches with hexagonal grid arrangement. f) 3D AFM topography image after partially filling of the nanotrenches with 50 nm of ZnO and 150 nm of hydrogel

According to a previous study from our group, films of p(NVCL-co-DEGDVE) with 20% nominal DEGDVE cross-linker, deposited on Si(100) wafers, are stable in aqueous media.[23] Furthermore, it has been observed that ending the PEALD deposition with an $O_2$ plasma pulse improves the adhesion of the subsequently deposited hydrogel to the ZnO surface. Without plasma exposure, the hydrogel would eventually delaminate from the ZnO upon emersion in water, whereas this was not observed if the ZnO surface was activated with an $O_2$ plasma

before the hydrogel deposition. We conclude that the OH groups, formed by the $O_2$ plasma on the ZnO surface, lead to a stronger (covalent) bonding between the hydrogel and the ZnO.

Tridimensional AFM topography images show the nanostructures prior the deposition (**Figure 29e**) and after deposition of ZnO and p(NVCL-co-DEGDVE) (**Figure 29f**) over a scan area of 10 x 10 µm. The periodicity of nanostructures prior to filling clearly confirms the dimensions of the structures as well as the periodicity (d = 500 nm and pitch = 1000 nm, with hexagonal grid arrangement). After partial filling of these nanotrenches with the core-shell nanorods (50 nm of ZnO and 150 nm of p(NVCL-co-DEGDVE) with 35% DEGDVE fraction) no apparent change in roughness could be observed (Figure 29f), which indicates the conformality of the PEALD and iCVD techniques. However, due to the limited AFM tip dimensions in comparison to the nanostructures, an accurate quantization of the roughness was not possible.

**Piezoelectric charge response:**

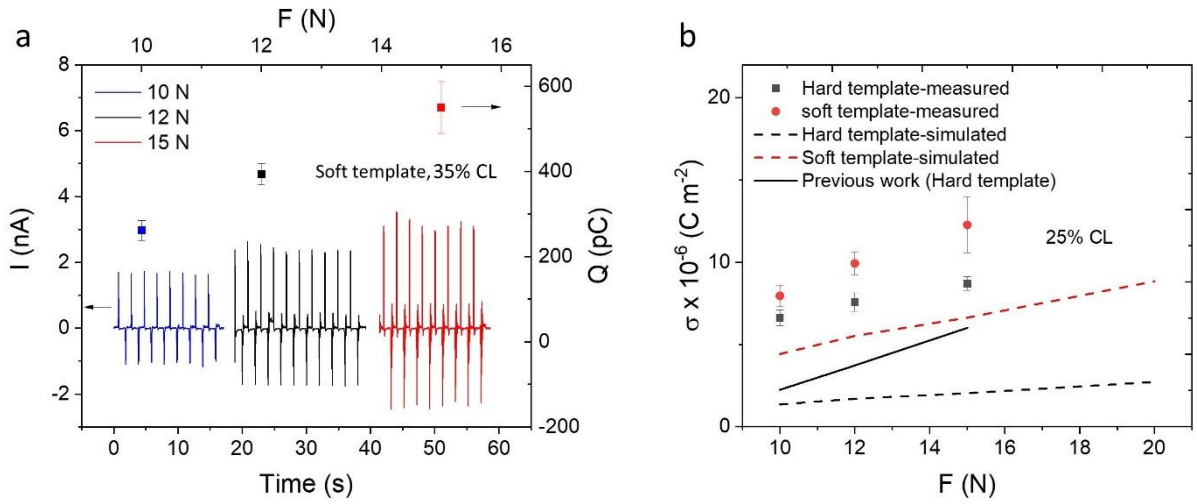


Figure 30. a) Piezoelectric current *I* (vs. time) and charge Q (vs. force) response to force *F* = 10, 12 and 15 N, over eight to ten cycles of press and release (the results are averaged over three electrode fields). The measurements were performed on a device with Al bottom electrode b) Charge density *σ* as a function of the force *F*, showing influence of template modulus using a FEM model (dashed lines), experimental data (each point was averaged over 3 measurements) and our previous experimental results from ref. [14] (solid line). The measurements were performed on a device with ITO bottom electrode

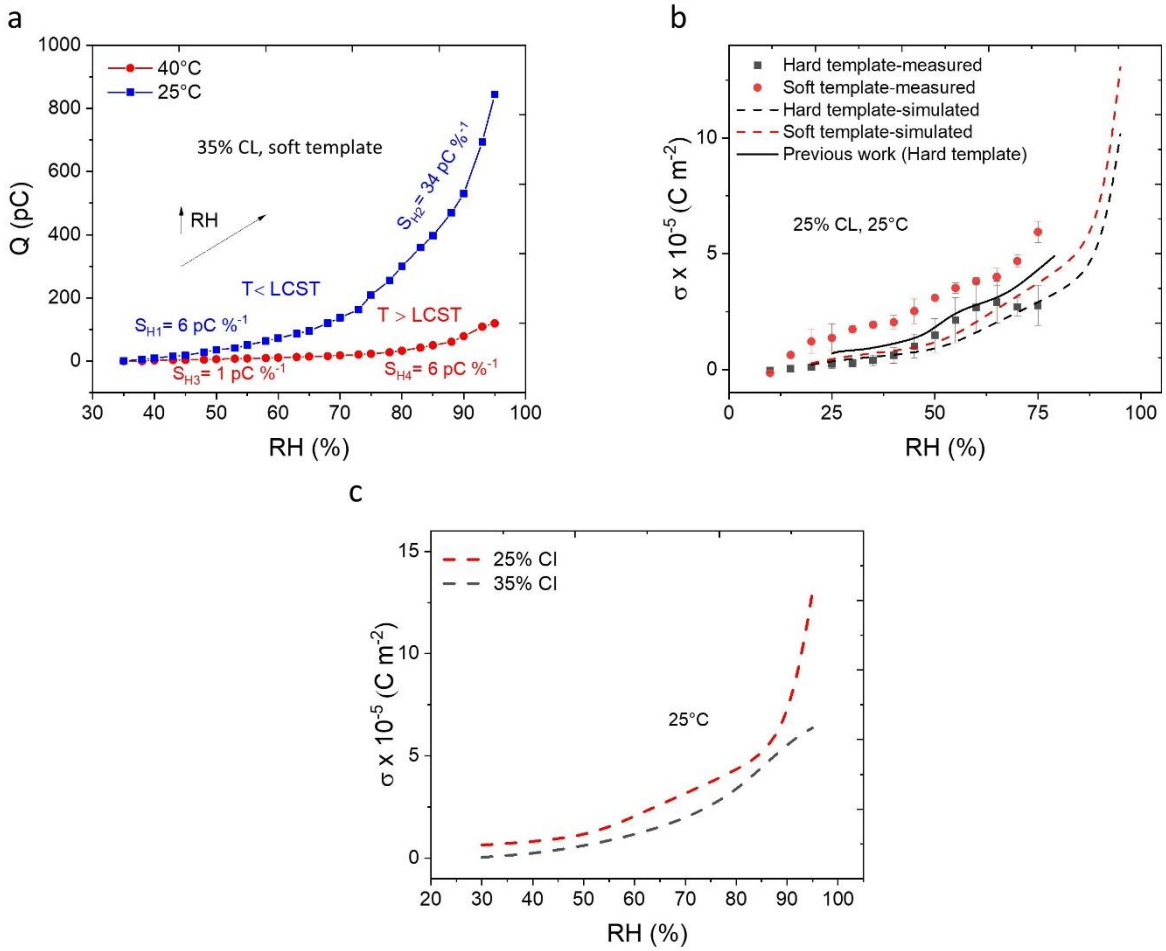


Figure 31. a) Charge response to humidity (*RH* = 35 – 95 %) at 25°C (blue) and 40°C (red). The sensitivity $S_H$ is indicated in the figure. Measurements were performed on a device with Al bottom electrode. b) Charge density as a function of RH showing the influence of the template modulus for nanorods with 25% cross-linked hydrogel layer. The dashed lines correspond to FEM data and are contrasted to the recent experimental data, obtained from a device with ITO bottom electrode, (each data point was averaged over 3 measurements) and our previous experimental data (solid line). The measurements were performed using the bubbler set-up, which allows fast and dynamic control of the humidity but limits it to a maximum of 75%. c) Charge density as a function of the relative humidity (30 to 95%) showing the influence of the hydrogel cross-linker fraction (25 vs 35%), data obtained from FEM simulations

**Figure 30a** shows the device piezoelectric response to step force signal *F* = 10, 12 and 15 N (*f* = 0.5 Hz) for eight to ten cycles of press and release, with the piezoelectric current *I* recorded as a function of time and the charge *Q* (corresponding to the time integral of *I(t)*), plotted as a function of *F*. In response to *F* = 10 N, applied with a rounded stamp (*d* = 5 mm), *I* = 1.7 ± 0.1 nA and *Q* = 261 ± 23 pC are measured. The magnitudes of *I* and *Q* increase to 3.3 ± 0.2 nA and 550 ± 61 pC at 15 N, respectively. It can be observed that the peak-to-peak current of each cycle varies slightly, which is attributed to the hydrogel/Ag interface as well as plastic deformation of the hydrogel layer/core due to contact with the relatively hard stamp. Additionally, the use of a flexible PET substrate promotes mechanical deformation of the active

layer, where in-plane and out-of-plane strain components, which are enhanced with increasing force magnitude, influence the micromechanical deformation of substrate and active layer. The substrate delayed relaxation results in current peak difference between press and release. This leads to the above-mentioned fluctuations between cycles.[24] In our previous work, we have demonstrated a maximum $Q$ = 252 ± 25 pC at $F$ = 15 N for a sample with hard PUA template (high $E$) and an active TE area of 1 $cm^2$. In this work, the improvement in signal magnitude is attributed to the softness (low $E$) of the PUA template, as assessed also with the FEM model shown in **Figure 30b**. Figure 30b shows the charge density $\sigma$ as a function of $F$, where the influence of the template rigidity ($E_{soft}$ = 200 MPa vs $E_{hard}$ = 2 GPa) is investigated using the FEM model, and compared to the experimental data and to our previous work. According to the FEM model, the soft template ($E_{soft,sim}$= 200 MPa) resulted in a charge density $\sigma$ = 6.63 x $10^{-6}$ and 8.85 x $10^{-6}$ C $m^{-2}$ at $F$ = 15 and 20 N, respectively, which is at least three times the charge density obtained from the FEM model for a hard template (2.04 x $10^{-6}$ and 2.7 x $10^{-6}$ C $m^{-2}$ at $F$ = 15 and 20 N, respectively). The enhanced σ is attributed to the higher deformability of the soft template, which is reflected in higher strain on the ZnO shell resulting in the generation of more piezoelectric charges. The same trend is observed experimentally yielding e.g. $\sigma$ = 1.22 x $10^{-5}$ C $m^{-2}$ for the soft template and $\sigma$ = 8.7 x $10^{-6}$ C $m^{-2}$ for the hard template at $F$ = 15 N. The small deviations between the experimental and the simulated curves (roughly a factor of two) are attributed to the limits of the model, as explained in our previous work.[14] Previously, we measured a lower charge density for the hard template, $\sigma$ = 6 x $10^{-6}$ C $m^{-2}$ for $F$ = 15 N. Such improvement is attributed to the improved layers adhesion due to the plasma activation step prior to the hydrogel core deposition. Better adhesion leads to improved interface between the different layers, which improves interfacial charge transfer.

**Figure 31a** shows the response to humidity changes as a consequence of the swelling of the hydrogel core, which is translated to piezoelectric charge output due to stress exerted from the swollen hydrogel (upon water molecules intake) onto the ZnO shell. $Q$ is measured for a relative humidity range of 35 to 95% RH, at 25°C and 40°C, i.e. below and above the LCST, respectively, considering that the LCST of the 35% cross-linked hydrogel was determined to be 30 ± 2 °C.[20] Below the LCST (25°C), a maximum $Q$ = 850 pC is measured at 95% RH (data set shown in blue), which drops to 120 pC above the LCST (data set shown in red). At 25 °C, the sensitivity to humidity, $S_H = \frac{\Delta Q}{\Delta RH\%}$, is $S_{H1}$ = 6 pC $\%^{-1}$ for the (relative) humidity range 35 to 80 % and $S_{H2}$ = 34 pC $\%^{-1}$ for the RH range between 80 and 95%. Such difference in sensitivity for the different humidity ranges, is related to the non-linear dependence of the hydrogel swelling with humidity.[7] Above the LCST (40°C), the sensitivity significantly decreases since the hydrogel is in its unswollen state, with $S_{H3}$ = 0.7 pC $\%^{-1}$ between 35 and 80 % RH and $S_{H4}$ = 6 pC $\%^{-1}$ for the RH range between 80 and 95%.

The influence of the PUA template mechanical properties on the response to humidity is investigated in **Figure 31b**, where the use of a soft template enhances the response magnitude and with the same trend validated experimentally. In our previous work, we reported higher response magnitude of the core-shell nanorods to humidity. Such difference is due to the fact that the previous sensors were fabricated with a less cross-linked hydrogel (25% nominally cross-linked vs 35% in this work).[17] At room temperature, 25% hydrogel planar films on Si wafer show a swelling of ≈ 225% of their initial thickness (dry-state), while the 35% films show ≈ 200% swelling. Moreover, the cross-linker fraction has an influence on the mechanical properties of the hydrogel ($E_{10\%cl}$ = 5.8 MPa and $E_{75\%cl}$ = 107.2 MPa)[23] and as a result, influences the applied stress $\sigma$ on the ZnO shell. This assumption is validated by the FEM model and the results are shown in **Figure 31c**, revealing that a hydrogel with lower cross-linking results in a higher charge density.

**Figure 32a** depicts the response to a temperature profile (10 – 50°C) at 85% RH (data set shown in blue) and 40% RH (data set shown in red). Within this temperature range, a transition through the LCST is expected. At 85 % RH, a maximum $Q$ = 3700 pC (in comparison to 2100 pC achieved in our previous work) is measured and a temperature sensitivity, $S_{T1}$ = 45 pC °C$^{-1}$ is calculated between $T$ = 10 – 35°C. The sensitivity increases for the temperature range $T$ = 35 – 50°C, with $S_{T2}$ = 200 pC °C$^{-1}$. As demonstrated in our previous work, a single sensitivity to temperature ($S_T$ = 140 pC °C$^{-1}$) is expected at elevated RH and around the hydrogel's LCST.[17] However, for this device, were p(NVCL-co-DEGDVE) has a higher cross-linker %, the coil to globule transition is less sharp, providing temperature sensitivity for a wider range, in comparison to lower cross-linked p(NVCL-co-DEGDVE).[20] . At 40% RH, a maximum $Q$ = 2200 pC is measured and the sensitivity $S_{T3}$ and $S_{T4}$ are calculated to be 22 and 110 pC °C$^{-1}$ respectively. However, as indicated in **Figure 32b**, a hydrogel with 35% cross-linker fraction results in lower σ.

**Figure 32c** illustrates the influence of the template modulus on the temperature response for a device with 25% cross-linked hydrogel core. The soft template clearly increases the charge density as is revealed both in the model and in the measured data.

The response of the multi-stimuli responsive nanorod skin to six cycles of force excitations from touching is about 1800 pC, as shown in **Figure 33a** and **33b**. Additionally, five cycles of humid air blown from a human mouth are shown in **Figure 33c** and **33d**. For the consecutive blows, a maximum $Q$ = 625 pC is measured. The response is attributed to the high humidity of the breath.

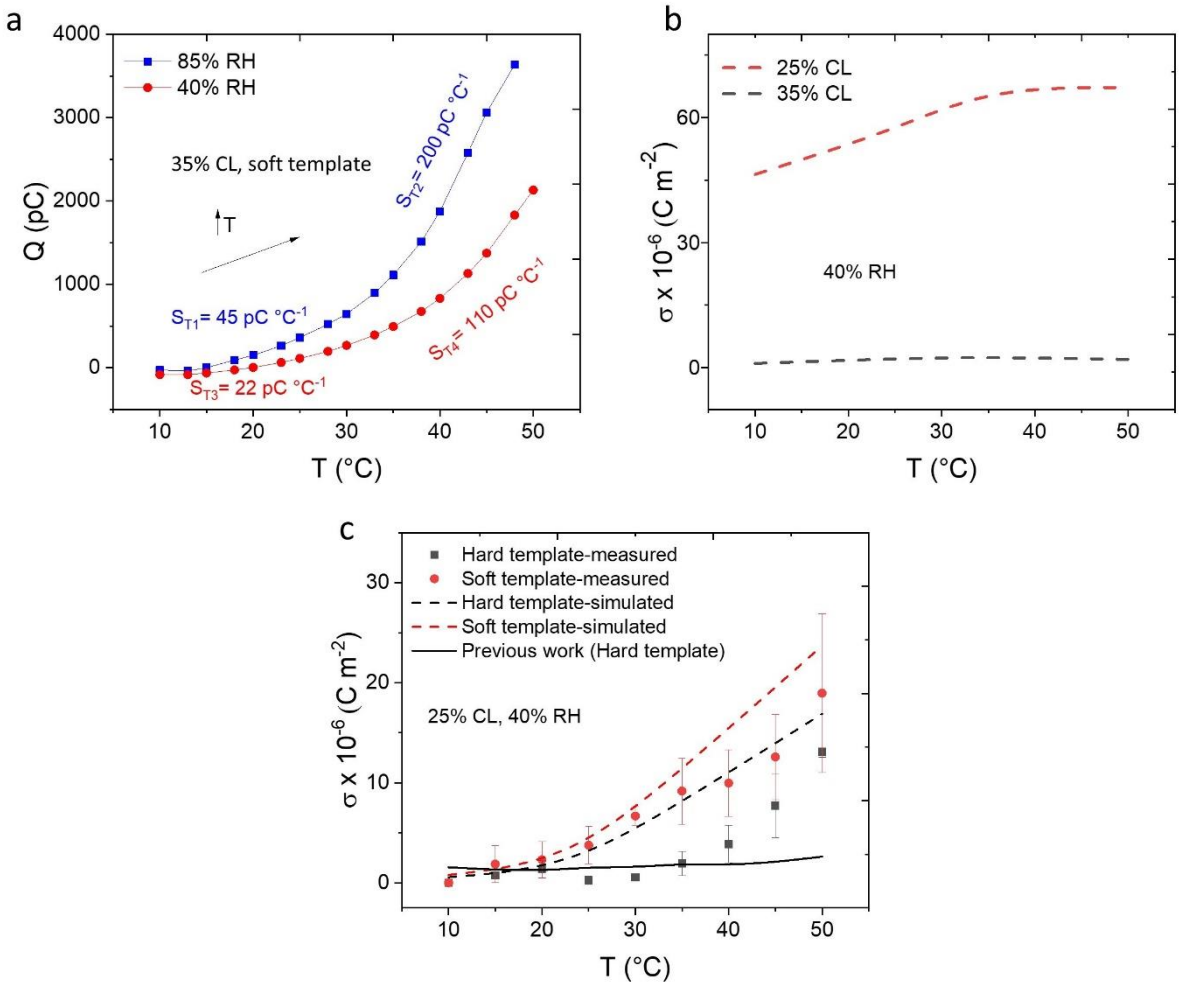


Figure 32. a) Charge *Q* as a function of *T* (10 to 50°C) at 85 and 40% *RH*, with sensitivity to temperature $S_T$ indicated in the figure. Measurements were performed on a sample with Al bottom electrode. b) FEM results for $\sigma$ as a function of *RH* (30 to 95%) for hydrogels with cross-linker fraction 25% and 35%. b) c) $\sigma$ as a function of *T* for 25% CL sample at 40% *RH*, showing influence of template *E* using an FEM model (dashed lines), experimental data (data points averaged over 3 measurements) and our previous experimental results from ref. [14] data (solid line). Measurements were performed on a sample with ITO bottom electrode

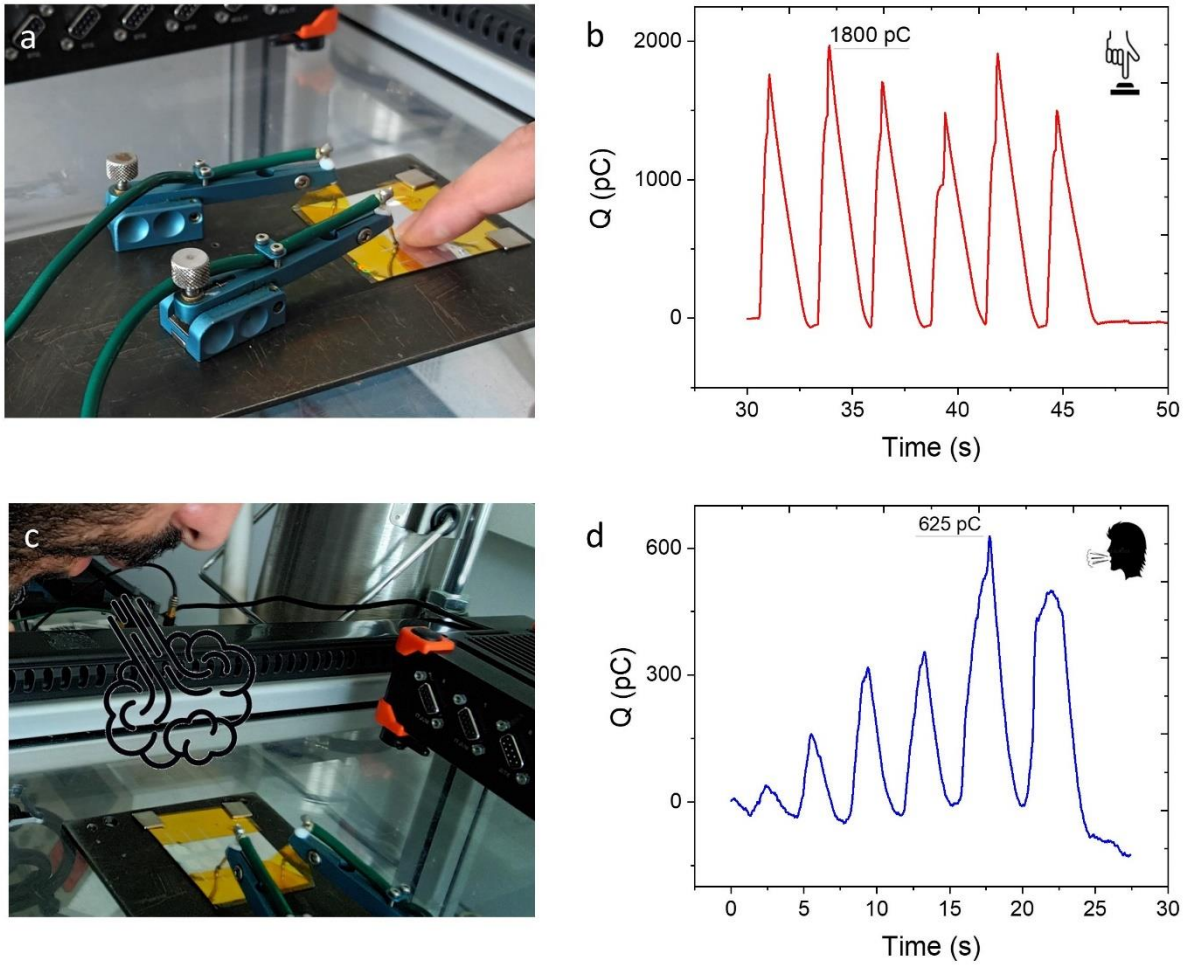


Figure 33. a,b) Response to six cycles of force excitation through finger touch yielding a maximum response of 1800 pC. c,d) Response to five cycles of air blown from a human mouth ($Q_{max}$ = 625 pC). Measurements were performed on a sample with 35% cross-linked hydrogel and Al serving as bottom electrode

**GEIS measurements:**

Literature shows that many pressure/force, humidity and temperature sensors rely on change in the active material resistance or capacitance to achieve desired sensitivity,[24–30] such parameters are probed with GEIS, which is investigated as an alternative and more comprehensive route for signal readout.

The core-shell nanorod devices were sequentially exposed to the temperatures of 10°C, 23°C and 35°C. At each temperature, the humidity was ramped from 30% to 95%. In **Figure 34a**, the Bode plots are depicted at the three temperature steps and 45% RH (exemplary). The impedance ($Z_{mod}$) decreases exponentially and the phase increases within the frequency range $f$ = 200 to 1500 Hz for all the performed measurements. This is a standard behavior for multilayers composed of dielectric materials, where each layer can be modelled as a parallel capacitive and resistive component (RC element).[31] A falling $Z_{mod}$ above the so-called cut off frequency (dipolar relaxation) is a typical performance of dielectrics.[31–33] Given that the input

and the output signals inside a capacitor have a 90° phase shift, the increase in phase angle with increasing frequency can be explained by the decrease in impedance of the capacitive component of the dielectric. This eases current flow (path of least impedance is favorable).[34] Moreover, it can be observed that the phase shifts down (increases) with increasing temperature, regardless of the coil-to-globule transition in the hydrogel. At 10 °C, the phase is measured to be -80° at *f* = 1000 Hz, which increases to -87° at 35°C.

$Z_{mod}$ decreases when temperature is increased from 10°C to 23°C (< LCST) but increases again at 35°C (>LCST). At the low frequency range where the measurements were conducted, only diffusional-limited electron transfer processes can be observed.[35] The diffusion is enhanced by temperature, therefore the higher the temperature, the lower the impedance. Diffusion, though, can be also affected by the coil-to-globule transition of the hydrogel. Below the LCST, the p(NVCL-co-DEGDVE) forms hydrogen bonds with water molecules and has a swollen and expanded coil structure in contact to the top electrode surface, leading to a lower diffusional barrier and to a decrease in the impedance. When temperature increases, the hydrophobic interaction inside the film becomes overwhelming, resulting in the break of hydrogen bonds between the hydrogel and water molecules and producing a contracted and compact globule structure, which forms now an effective diffusional barrier, therefore the impedance increases again. This is an indication that incorporation of water molecules into the hydrogel (which is influenced by the LCST) has a dominant effect on the overall impedance of the nanostructured multi-layer film, in comparison to temperature related dipole-dipole interactions.

Further, the phase and $Z_{mod}$ and were extracted at 210 Hz (at this frequency slight diffusion processes can still be expected)[36] and at the standard sampling frequency of 1000 Hz and plotted versus the relative humidity at the sequentially performed temperature steps (**Figure 34b** and **34c**). For both frequencies, the decrease in $Z_{mod}$ with increasing RH can be explained by the formation of hydronium ions, which hydrate and enhance the diffusion of excess protons via Grotthus chain reaction, resulting in a decrease in the resistivity.[37,38] Additionally, at high RH levels (≈ 90 %), a decrease in the phase angle magnitude coupled with decrease in $Z_{mod}$ can be explained by a decrease in the capacitance of the overall dielectric layers. It can be concluded that the phase angle and $Z_{mod}$ are sensitive to humidity and temperature.

The presented measurements are preliminary results and will only strive to present a proof-of-concept and the huge potential of extracting information from impedance spectra. A more profound analysis would be needed, by measuring each layer individually in a patterned and non-patterned configuration.

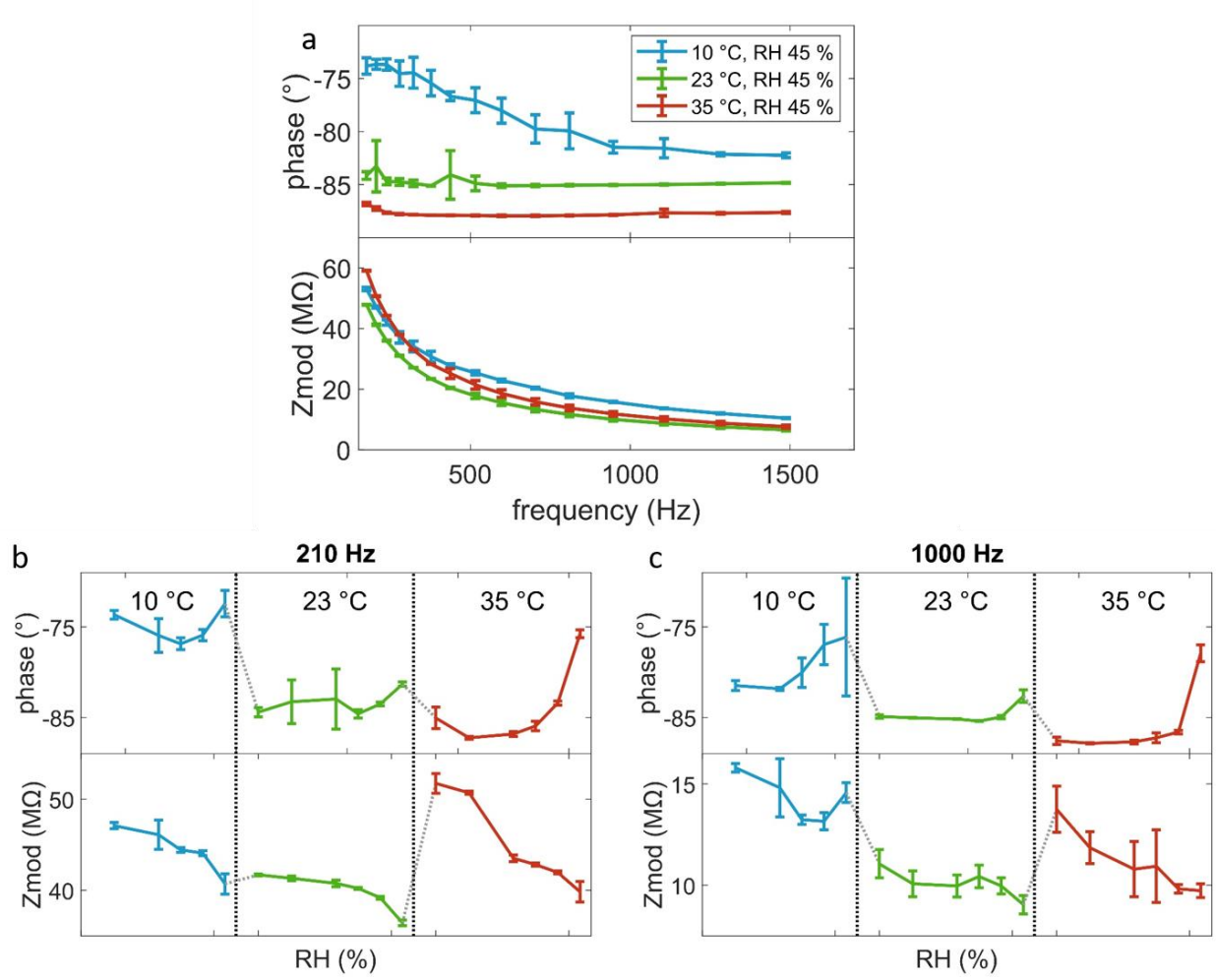


Figure 34. a) Bode plots showing the phase and the impedance ($Z_{mod}$) as a function of frequency $f$ = 200 – 1500 Hz of the patterned multilayer exposed to 10°C, 23°C and 35°C at 45% $RH$, $n$ = 3. b), c) Extracted at 210 Hz and 1000 Hz: phase and $Z_{mod}$ versus the relative humidity ($RH$ = 30 – 95%) at sequentially performed temperature steps, $n$ = 3

### 3.3.6 Conclusion

In conclusion, we fabricated force, humidity and temperature responsive sensors based on nanostructured thin films in one-of-a-kind multi-chamber reactor combining PEALD and iCVD. The sensing performance was optimized with respect to three parameters: (i) the fabrication method that allows in-situ interface activation; (ii) the template mechanical properties and (iii) the hydrogel cross-linker percentage. The multi-chamber reactor is equipped with a transfer chamber kept under vacuum to permit sample transfer and subsequent depositions without breaking the vacuum. Such reactor layout reduces surface contaminations arising from transfer processes as well as fabrication time, paving the road for industrial and large-scale fabrication. In addition, it improves the adhesion of the hydrogel to the ZnO and reduces delamination related to the hydrogel swelling, which yielded devices with better performance as apparent from the results compared to our previous work. Further, the devices are assessed

for multi-stimuli responsiveness, with a response of 550 pC to a 15 N force, a maximum sensitivity of 34 pC $\%^{-1}$ to humidity and 200 pC $°C^{-1}$ to temperature. Additionally, FEM simulations as well as experimental measurements indicate an improvement of the performance with the use of a PUA template with lower young's modulus, concluding first steps towards design optimization. Lastly, GEIS is employed to further understand and investigate the device's electrical properties for signal readout.

### 3.3.7 Author information

**Author Contributions**

The manuscript was written through contributions of all authors. All authors have given approval to the final version of the manuscript. Marlene Anzengruber and Taher Abu Ali share first authorship.

**ACKNOWLEDGMENT**

This project has received funding from the European Research Council (ERC) under the European Union's Horizon 2020 research and innovation program (Grant Agreement No. 715403).

### 3.3.8 References

(1) Cai, G.; Wang, J.; Qian, K.; Chen, J.; Li, S.; Lee, P. S. Extremely Stretchable Strain Sensors Based on Conductive Self-Healing Dynamic Cross-Links Hydrogels for Human-Motion Detection. *Advanced Science* **2017**, *4* (2). https://doi.org/10.1002/advs.201600190.

(2) An, R.; Zhang, X.; Han, L.; Wang, X.; Zhang, Y.; Shi, L.; Ran, R. Healing, Flexible, High Thermal Sensitive Dual-Network Ionic Conductive Hydrogels for 3D Linear Temperature Sensor. *Materials Science and Engineering C* **2020**, *107*. https://doi.org/10.1016/j.msec.2019.110310.

(3) Zhao, Y.; Lei, M.; Liu, S. X.; Zhao, Q. Smart Hydrogel-Based Optical Fiber SPR Sensor for PH Measurements. *Sens Actuators B Chem* **2018**, *261*, 226–232. https://doi.org/10.1016/j.snb.2018.01.120.

(4) Dallinger, A.; Kindlhofer, P.; Greco, F.; Coclite, A. M. Multiresponsive Soft Actuators Based on a Thermoresponsive Hydrogel and Embedded Laser-Induced Graphene. *ACS Appl Polym Mater* **2021**, *3* (4), 1809–1818. https://doi.org/10.1021/acsapm.0c01385.

(5) Zhang, D.; Ren, B.; Zhang, Y.; Xu, L.; Huang, Q.; He, Y.; Li, X.; Wu, J.; Yang, J.; Chen, Q.; Chang, Y.; Zheng, J. From Design to Applications of Stimuli-Responsive Hydrogel Strain Sensors. *Journal of Materials Chemistry B*. Royal Society of Chemistry April 28, **2020**, pp 3171–3191. https://doi.org/10.1039/c9tb02692d.

(6) Zheng, K.; Tong, Y.; Zhang, S.; He, R.; Xiao, L.; Iqbal, Z.; Zhang, Y.; Gao, J.; Zhang, L.; Jiang, L.; Li, Y. Flexible Bicolorimetric Polyacrylamide/Chitosan Hydrogels for Smart Real-Time Monitoring and Promotion of Wound Healing. *Adv Funct Mater* **2021**, *31* (34). https://doi.org/10.1002/adfm.202102599.

(7) Muralter, F.; Greco, F.; Coclite, A. M. Applicability of Vapor-Deposited Thermoresponsive Hydrogel Thin Films in Ultrafast Humidity Sensors/Actuators. *ACS Appl Polym Mater* **2020**, *2* (3), 1160–1168. https://doi.org/10.1021/acsapm.9b00957.

(8) Halligan, S. C.; Dalton, M. B.; Murray, K. A.; Dong, Y.; Wang, W.; Lyons, J. G.; Geever, L. M. Synthesis, Characterisation and Phase Transition Behaviour of Temperature-Responsive Physically Crosslinked Poly (N-Vinylcaprolactam) Based Polymers for Biomedical Applications. *Materials Science and Engineering C* **2017**, *79*, 130–139. https://doi.org/10.1016/j.msec.2017.03.241.

(9) Unger, K.; Salzmann, P.; Masciullo, C.; Cecchini, M.; Koller, G.; Coclite, A. M. Novel Light-Responsive Biocompatible Hydrogels Produced by Initiated Chemical Vapor Deposition. *ACS Appl Mater Interfaces* **2017**, *9* (20), 17408–17416. https://doi.org/10.1021/acsami.7b01527.

(10) Unger, K.; Greco, F.; Coclite, A. M. Temporary Tattoo PH Sensor with PH-Responsive Hydrogel via Initiated Chemical Vapor Deposition. *Adv Mater Technol* **2022**, *7* (5). https://doi.org/10.1002/admt.202100717.

(11) Mo, K.; He, M.; Cao, X.; Chang, C. Direct Current Electric Field Induced Gradient Hydrogel Actuators with Rapid Thermo-Responsive Performance as Soft Manipulators. *J Mater Chem C Mater* **2020**, *8* (8), 2756–2763. https://doi.org/10.1039/c9tc06407a.

(12) Salzmann, P.; Perrotta, A.; Coclite, A. M. Different Response Kinetics to Temperature and Water Vapor of Acrylamide Polymers Obtained by Initiated Chemical Vapor Deposition. *ACS Appl Mater Interfaces* **2018**, *10* (7), 6636–6645. https://doi.org/10.1021/acsami.7b18878.

(13) Kozanoğlu, S.; Özdemir, T.; Usanmaz, A. Polymerization of N-Vinylcaprolactam and Characterization of Poly(N-Vinylcaprolactam). *Journal of Macromolecular Science, Part A: Pure and Applied Chemistry* **2011**, *48* (6), 467–477. https://doi.org/10.1080/10601325.2011.573350.

(14) Suntornnond, R.; An, J.; Chua, C. K. Bioprinting of Thermoresponsive Hydrogels for Next Generation Tissue Engineering: A Review. *Macromolecular Materials and Engineering*. Wiley-VCH Verlag January 1, 2017. https://doi.org/10.1002/mame.201600266.

(15) Bruggeman, K. F.; Williams, R. J.; Nisbet, D. R. Dynamic and Responsive Growth Factor Delivery from Electrospun and Hydrogel Tissue Engineering Materials. *Adv Healthc Mater* **2018**, *7* (1). https://doi.org/10.1002/adhm.201700836.

(16) Marsili, L.; Dal Bo, M.; Eisele, G.; Donati, I.; Berti, F.; Toffoli, G. Characterization of Thermoresponsive Poly-n-Vinylcaprolactam Polymers for Biological Applications. *Polymers (Basel)* **2021**, *13* (16). https://doi.org/10.3390/polym13162639.

(17) Abu Ali, T.; Schäffner, P.; Belegratis, M.; Schider, G.; Stadlober, B.; Coclite, A. M. Smart Core-Shell Nanostructures for Force, Humidity, and Temperature Multi-Stimuli Responsiveness. *Adv Mater Technol* **2022**, 2200246. https://doi.org/10.1002/admt.202200246.

(18) Alf, M. E.; Godfrin, P. D.; Hatton, T. A.; Gleason, K. K. Sharp Hydrophilicity Switching and Conformality on Nanostructured Surfaces Prepared via Initiated Chemical Vapor Deposition (ICVD) of a Novel Thermally Responsive Copolymer. *Macromol Rapid Commun* **2010**, *31* (24), 2166–2172. https://doi.org/10.1002/marc.201000452.

(19) Abu Ali, T.; Pilz, J.; Schäffner, P.; Kratzer, M.; Teichert, C.; Stadlober, B.; Coclite, A. M. Piezoelectric Properties of Zinc Oxide Thin Films Grown by Plasma-Enhanced Atomic Layer Deposition. *Physica Status Solidi (A) Applications and Materials Science* **2020**, *217* (21). https://doi.org/10.1002/pssa.202000319.

(20) Perrotta, A.; Pilz, J.; Resel, R.; Werzer, O.; Coclite, A. M. Initial Growth and Crystallization Onset of Plasma Enhanced-Atomic Layer Deposited ZnO. *Crystals (Basel)* **2020**, *10* (4). https://doi.org/10.3390/cryst10040291.

(21) Pilz, J.; Perrotta, A.; Christian, P.; Tazreiter, M.; Resel, R.; Leising, G.; Griesser, T.; Coclite, A. M. Tuning of Material Properties of ZnO Thin Films Grown by Plasma-Enhanced Atomic Layer Deposition at Room Temperature. *Journal of Vacuum Science & Technology A: Vacuum, Surfaces, and Films* **2018**, *36* (1), 01A109. https://doi.org/10.1116/1.5003334.

(22) Pilz, J.; Perrotta, A.; Leising, G.; Coclite, A. M. ZnO Thin Films Grown by Plasma-Enhanced Atomic Layer Deposition: Material Properties Within and Outside the “Atomic Layer Deposition Window.” *Physica Status Solidi (A) Applications and Materials Science* **2020**, *217* (8). https://doi.org/10.1002/pssa.201900256.

(23) Muralter, F.; Perrotta, A.; Werzer, O.; Coclite, A. M. Interlink between Tunable Material Properties and Thermoresponsiveness of Cross-Linked Poly(N-Vinylcaprolactam) Thin Films Deposited by Initiated Chemical Vapor Deposition. *Macromolecules* **2019**, *52* (18), 6817–6824. https://doi.org/10.1021/acs.macromol.9b01364.

(24) Petritz, A.; Karner-Petritz, E.; Uemura, T.; Schäffner, P.; Araki, T.; Stadlober, B.; Sekitani, T. Imperceptible Energy Harvesting Device and Biomedical Sensor Based on Ultraflexible Ferroelectric Transducers and Organic Diodes. *Nat Commun* **2021**, *12* (1). https://doi.org/10.1038/s41467-021-22663-6.

(25) Zhong, Y.; Li, W.; Zhao, X.; Jiang, X.; Lin, S.; Zhen, Z.; Chen, W.; Xie, D.; Zhu, H. High-Response Room-Temperature NO 2 Sensor and Ultrafast Humidity Sensor Based on SnO 2 with Rich Oxygen Vacancy. *ACS Appl Mater Interfaces* **2019**, *11* (14), 13441–13449. https://doi.org/10.1021/acsami.9b01737.

(26) Xu, L.; Xuan, W.; Chen, J.; Zhang, C.; Tang, Y.; Huang, X.; Li, W.; Jin, H.; Dong, S.; Yin, W.; Fu, Y.; Luo, J. Fully Self-Powered Instantaneous Wireless Humidity Sensing System Based on Triboelectric Nanogenerator. *Nano Energy* **2021**, *83*. https://doi.org/10.1016/j.nanoen.2021.105814.

(27) Wang, Y. F.; Sekine, T.; Takeda, Y.; Yokosawa, K.; Matsui, H.; Kumaki, D.; Shiba, T.; Nishikawa, T.; Tokito, S. Fully Printed PEDOT:PSS-Based Temperature Sensor with High Humidity Stability for Wireless Healthcare Monitoring. *Sci Rep* **2020**, *10* (1). https://doi.org/10.1038/s41598-020-59432-2.

(28) Liu, G.; Tan, Q.; Kou, H.; Zhang, L.; Wang, J.; Lv, W.; Dong, H.; Xiong, J. A Flexible Temperature Sensor Based on Reduced Graphene Oxide for Robot Skin Used in Internet of Things. *Sensors (Switzerland)* **2018**, *18* (5). https://doi.org/10.3390/s18051400.

(29) Wang, Y.; Zhang, L.; Zhang, Z.; Sun, P.; Chen, H. High-Sensitivity Wearable and Flexible Humidity Sensor Based on Graphene Oxide/Non-Woven Fabric for Respiration Monitoring. *Langmuir* **2020**, *36* (32), 9443–9448. https://doi.org/10.1021/acs.langmuir.0c01315.

(30) Zhang, D.; Zong, X.; Wu, Z.; Zhang, Y. Hierarchical Self-Assembled SnS2 Nanoflower/Zn2SnO4 Hollow Sphere Nanohybrid for Humidity-Sensing Applications. *ACS Appl Mater Interfaces* **2018**, *10* (38), 32631–32639. https://doi.org/10.1021/acsami.8b08493.

(31) Faia, P. M.; Furtado, C. S.; Ferreira, A. J. AC Impedance Spectroscopy: A New Equivalent Circuit for Titania Thick Film Humidity Sensors. In *Sensors and Actuators, B: Chemical*; Elsevier, 2005; Vol. 107, pp 353–359. https://doi.org/10.1016/j.snb.2004.10.021.

(32) Ersöz, B.; Schmitt, K.; Wöllenstein, J. CO2 Gas Sensing with an Electrolyte-Gated Transistor Using Impedance Spectroscopy. *Sens Actuators B Chem* **2021**, *334*. https://doi.org/10.1016/j.snb.2021.129598.

(33) Ali, T. A.; Groten, J.; Clade, J.; Collin, D.; Schaffner, P.; Zirkl, M.; Coclite, A. M.; Domann, G.; Stadlober, B. Screen-Printed Ferroelectric P(VDF-TrFE)- Co-PbTiO3and P(VDF-TrFE)- Co-NaBiTi2O6Nanocomposites for Selective Temperature and Pressure Sensing. *ACS Appl Mater Interfaces* **2020**, *12* (34), 38614–38625. https://doi.org/10.1021/acsami.0c08469.

(34) Gamry Instruments. "Basics of electrochemical impedance spectroscopy." G. Instruments, Complex impedance in Corrosion (2007): 1-30.

(35) Sheeney-Haj-Ichia, L.; Sharabi, G.; Willner, I. *Control of the Electronic Properties of Thermosensitive Poly(N-Isopropylacrylamide) and Au-Nanoparticle/Poly(N-Isopropylacrylamide) Composite Hydrogels upon Phase Transition***.

(36) Chen, C.; Yesilbas, G.; Lenz, A.; Schneider, O.; Knoll, A. C. Machine Learning Approach for Full Impedance Spectrum Study of Li-Ion Battery. In *IECON Proceedings (Industrial Electronics Conference)*; IEEE Computer Society, 2020; Vol. 2020-October, pp 3747–3752. https://doi.org/10.1109/IECON43393.2020.9254622.

(37) Mistewicz, K.; Starczewska, A.; Jesionek, M.; Nowak, M.; Kozioł, M.; Stróż, D. Humidity Dependent Impedance Characteristics of SbSeI Nanowires. *Appl Surf Sci* **2020**, *513*. https://doi.org/10.1016/j.apsusc.2020.145859.

(38) Wu, Z.; Yang, J.; Sun, X.; Wu, Y.; Wang, L.; Meng, G.; Kuang, D.; Guo, X. Z.; Qu, W.; Du, B.; Liang, C.; Fang, X.; Tang, X.; He, Y. An Excellent Impedance-Type Humidity Sensor Based on Halide Perovskite CsPbBr3 Nanoparticles for Human Respiration Monitoring. *Sens Actuators B Chem* **2021**, *337*. https://doi.org/10.1016/j.snb.2021.129772.

### 3.3.9 Supporting information

**Geometry used in FEM simulations:**

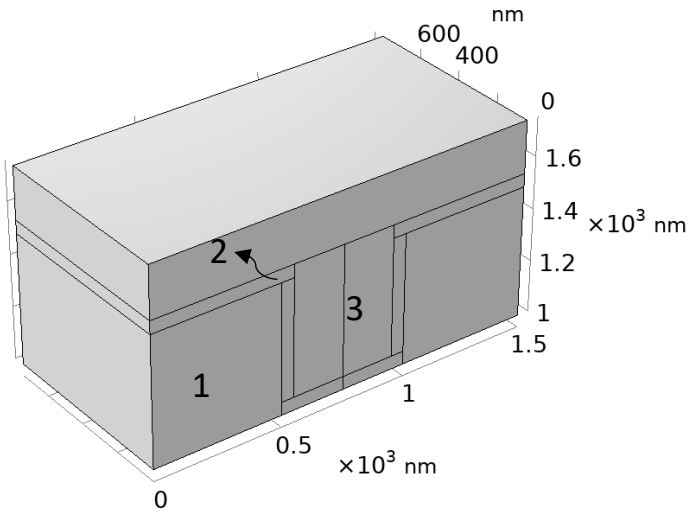


Figure 35. Geometry of half a nanorod used in the FEM model with 1.PUA template, 2.ZnO shell and 3.Hydrogel core

**Equations used in FEM simulations:**

*Hygroscopic swelling:*

$$\varepsilon = \beta \, x \, C_{mo} \qquad (55)$$

Where,

$\varepsilon$ is the hygroscopic strain

β is the hydrogel swelling coefficient ($m^3\ Kg^{-1}$)

$C_{mo}$ is the moisture concentration in air ($Kg^{-1}\ m^3$), which is equivalent to RH %

*Piezoelectric consecutive equations (strain-charge form):*

$$\sigma = c_E \varepsilon - eE \qquad (56)$$

$$D = e\varepsilon + \varepsilon_0 \varepsilon_r E \qquad (57)$$

Where,

σ is the stress (Pa)

$c_E$ is the stiffness matrix (Pa)

ε is the strain

e is the coupling matrix (C $m^{-2}$)

E is the electric field (V $m^{-1}$)

D is the electric field displacement (C $m^{-2}$)

$\varepsilon_0$ is the vacuum permittivity (F $m^{-1}$)

$\varepsilon_r$ is the relative permittivity matrix

*Charge conservation:*

$$\rho_v = \nabla . D \qquad (58)$$

Where,

$\rho_v$ is the charge density (C $m^{-3}$)

∇ is the divergence ($m^{-1}$)

D is the electric field displacement (C $m^{-2}$)

**Material properties used in FEM simulations:**

Table 5. Swelling coefficient β and moisture concentration in air Cmo of p(NVCL-co-DEGDVE) 25% nominally cross-linked at 10, 25, 35 and 50 °C for RH = 20 – 95

| RH [%] | $C_{mo}$ (10 °C) [kg m$^3$] | β (10 °C) [m$^3$ kg$^{-1}$] | $C_{mo}$ (25 °C) [kg m$^3$] | β (25 °C) [m$^3$ kg$^{-1}$] | $C_{mo}$ (35 °C) [kg m$^3$] | β (35 °C) [m$^3$ kg$^{-1}$] | $C_{mo}$ (50 °C) [kg m$^3$] | β (50 °C) [m$^3$ kg$^{-1}$] |
|---|---|---|---|---|---|---|---|---|
| 20 | 0.002 | - | 0.005 | 0.3 | 0.008 | - | 0.02 | - |
| 30 | 0.003 | - | 0.007 | 0.35 | 0.012 | 0.1 | 0.025 | 0.1 |
| 40 | 0.004 | 0.4 | 0.009 | 0.4 | 0.015 | 0.15 | 0.033 | 0.2 |
| 50 | 0.006 | 1 | 0.01 | 0.6 | 0.02 | 0.3 | 0.04 | 0.3 |
| 60 | 0.0065 | 2 | 0.013 | 1 | 0.023 | 0.4 | 0.05 | 0.5 |
| 70 | 0.007 | 4.2 | 0.016 | 2.1 | 0.027 | 0.7 | 0.06 | 0.6 |
| 80 | 0.0075 | 6.1 | 0.018 | 4.1 | 0.03 | 1.3 | 0.066 | 0.7 |
| 90 | 0.008 | 26.4 | 0.02 | 9.5 | 0.035 | 3.7 | 0.075 | 1.5 |
| 95 | 0.009 | 28.6 | 0.021 | 10 | 0.037 | 4.7 | 0.08 | 1.7 |

Table 6. Swelling coefficient β and moisture concentration in air Cmo of p(NVCL-co-DEGDVE) 35% nominally cross-linked at 10, 25, 35, 40 and 50 °C for RH = 30 – 95 %

| RH [%] | $C_{mo}$ (10 °C) [kg m$^3$] | β (10 °C) [m$^3$ kg$^{-1}$] | $C_{mo}$ (25 °C) [kg m$^3$] | β (25 °C) [m$^3$ kg$^{-1}$] | $C_{mo}$ (35 °C) [kg m$^3$] | β (35 °C) [m$^3$ kg$^{-1}$] | $C_{mo}$ (50 °C) [kg m$^3$] | β (50 °C) [m$^3$ kg$^{-1}$] |
|---|---|---|---|---|---|---|---|---|
| 30 | - | - | 0.007 | 0.17 | 0.012 | - | 0.025 | 0.062 |
| 40 | 0.004 | - | 0.009 | 0.64 | 0.015 | 0.45 | 0.033 | 0.23 |
| 50 | 0.006 | 0.45 | 0.01 | 1.56 | 0.02 | - | 0.04 | 0.46 |
| 60 | 0.0065 | 1.31 | 0.013 | 2.28 | 0.023 | 1.42 | 0.05 | 0.66 |
| 70 | 0.007 | 2.42 | 0.016 | 3.14 | 0.027 | - | 0.06 | 0.94 |
| 80 | 0.0075 | 7.62 | 0.018 | 4.70 | 0.03 | - | 0.066 | 1.35 |
| 90 | 0.008 | 19.13 | 0.02 | 7.44 | 0.035 | - | 0.075 | 1.94 |
| 95 | 0.009 | 19.3 | 0.021 | 7.96 | 0.037 | - | 0.08 | 2.16 |

## Table 7. Input parameters of different materials used in FEM models

| Component | Description | Symbol | Value |
|---|---|---|---|
| ZnO | Stiffness matrix | $c_E$ | $\begin{pmatrix} 2.1\,x\,10^{11} & 1.2\,x\,10^{11} & 1.05\,x\,10^{11} & 0 & 0 & 0 \\ 1.2\,x\,10^{11} & 2.1\,x\,10^{11} & 1.05\,x\,10^{11} & 0 & 0 & 0 \\ 1.05\,x\,10^{11} & 1.05\,x\,10^{11} & 2.1\,x\,10^{11} & 0 & 0 & 0 \\ 0 & 0 & 0 & 4.2\,x\,10^{10} & 0 & 0 \\ 0 & 0 & 0 & 0 & 4.2\,x\,10^{10} & 0 \\ 0 & 0 & 0 & 0 & 0 & 4.4\,x\,10^{10} \end{pmatrix}$ Pa |
| | Poisson's ratio | $v$ | 0.3 |
| | Density | $\rho$ | 5680 Kg m$^{-3}$ |
| | Coupling matrix | $E$ | $\begin{pmatrix} 0 & 0 & 0 & 0 & -0.48 & 0 \\ 0 & 0 & 0 & -0.48 & 0 & 0 \\ -0.56 & -0.56 & 1.32 & 0 & 0 & 0 \end{pmatrix}$ C m$^{-2}$ |
| p(NVCL-co-DEGDVE) | Young's modulus | $E$ | 12 MPa |
| | Poisson's ratio | $v$ | 0.3 |
| | Density | $\rho$ | 1200 Kg m$^{-3}$ |
| | Relative permittivity | $\varepsilon_r$ | 2.7 |
| PUA | Young's modulus | $E$ | 200 MPa or 2 GPa |
| | Poisson's ratio | $v$ | 0.4 |
| | Density | $\rho$ | 1060 Kg m$^{-3}$ |
| | Relative permittivity | $\varepsilon_r$ | 4.97 |

# 4
# Conclusions

This chapter provides a summary of the conclusions drawn from the peer-reviewed articles presented in chapter 3.

The work explored in this thesis presents a new e-skin concept based on force, humidity and temperature multi-stimuli responsive nanorods. In this context, three peer-reviewed research papers were presented starting with the first work titled 'Piezoelectric Properties of Zinc Oxide Thin Films Grown by Plasma-Enhanced Atomic Layer Deposition', in which ZnO thin films with $t$ = 50-65 nm were deposited by PEALD on ITO coated PET and glass. In the paper, the influence of the substrate temperature during deposition on the crystallographic orientation and the related directional piezoelectric properties has been investigated. At low substrate temperatures (<50°C), the films exhibit (100) preferential orientation, which changes to (002) with increasing temperature. ZnO deposited on ITO coated PET demonstrated the applicability of PEALD in depositions on flexible substrates with low thermal stability. Both macroscopic and microscopic piezoelectric properties were explored in two separate setups. Macroscopic characterization of the piezoelectric properties was done with an in-house built setup with a step force signal $F$ = 10 N. It has been demonstrated that, films grown on PET result in higher piezoelectric charge output, when compared to films grown on glass. This is explained by the mechanical deformation of the substrate and therefore, the ZnO film on top, which introduces transversal and longitudinal strain components contributing to the generated charge. Additionally, the $d_{33}$ coefficient of ZnO films deposited on glass substrate was calculated between 3 and 20 pC $N^{-1}$ for substrate temperature between 25 and 225°C. Piezo force microscopy was utilized for microscopic characterization of the piezoelectric properties. From the topography images, it can be concluded that ZnO deposited at 25°C has polycrystalline morphology with grain size ≈ 30 nm, while the piezo response amplitude shows a maximum displacement of 20 pm. However, at 225°C a grain size of ≈60 nm is obtained. Within the grain, maximum displacement is measured, which decays at the grain boundary.

In the second publication titled 'Smart Core-Shell Nanostructures for Force, Humidity and Temperature Multi-Stimuli Responsiveness', the full concept of the multi-stimuli responsive nanorods was presented. It started with presenting the full fabrication of the sensor on flexible PET substrate, where state-of-the-art nanofabrication techniques such as UV-NIL, PEALD and iCVD were utilized. The fabricated device had an active layer with a thickness of 6 µm and a nanorod density of $10^8$ $cm^{-2}$. SEM imaging of the nanostructured polymeric template surface as well as filling with the core-shell nanorods was performed. Dielectric spectroscopy performed within a frequency range of 42 to 5 MHz, indicated that the hydrogel core increases the overall dielectric constant of the active layer, due to incorporation of water molecules within its mesh ($\varepsilon'$ = 5.3 at 10 kHz). Moreover, I-V characteristic measurements indicated that the hydrogel core increases the leakage current as well as current density asymmetry. More importantly, multi-stimuli characterization is presented starting with force, where $F$ = 10 – 20 N was applied and a sensitivity $S_f$ = 22-36

pC $N^{-1}$ was demonstrated. As expected, the sensitivity to force is influenced by the flexibility of the PET substrate. FEM simulations indicate that the maximum charge response to force occurs at the edge of the nanorod and decays substantially along the lateral dimensions, which indicates a force sensing resolution down to the geometry of a single nanorod. To that, localized force response with minimum cross talk between pixels ($A$ = 0.25 $mm^2$) was additionally demonstrated. The e-skin response to humidity and temperature through the swelling of the hydrogel core was carried out in an environmental chamber, with $S_H$ = 0.1 – 1.2 nC $\%^{-1}$ below the LCST and $S_H$ = 0.01 – 0.1 nC $\%^{-1}$ above the LCST, which was measured for 25% cross-linked p(NVCL-co-DEGDVE). Finally yet importantly, the response to temperature was demonstrated with $S_T$ = 0.14 nC $°C^{-1}$ at $RH$ = 95%, with a response to a temperature range close to the LCST and at elevated humidity.

The third and last publication titled 'Enhancement of the sensing performance in multi-stimuli responsive hybrid materials' presented a multi-chamber reactor, which facilitates transferring the sample between the PEALD and iCVD processes with vacuum conditions maintained at 20 µbar, with the aim of reducing surface contaminations during transfer processes. Additionally, the work presented an e-skin based on a hydrogel core with 35% CL, with a lower swelling magnitude and therefore response magnitude to humidity and temperature (a maximum sensitivity of 34 pC $\%^{-1}$ to humidity and 200 pC $°C^{-1}$ to temperature), compared to the e-skin presented in the second publication. The influence of the cross-linker percentage on the e-skin performance was tested experimentally and compared to data obtained from a FEM model. The work additionally explored the influence of the template material's mechanical properties (hard vs soft) on the e-skin performance, with the sensitivity to force increasing to 8.85 µC $m^{-2}$ for a soft template vs 2.7 µC $m^{-2}$ for a hard template at $F$ = 20 N.

# Appendices

# A. FEM simulations for device optimization

## A.1 Influence of pitch

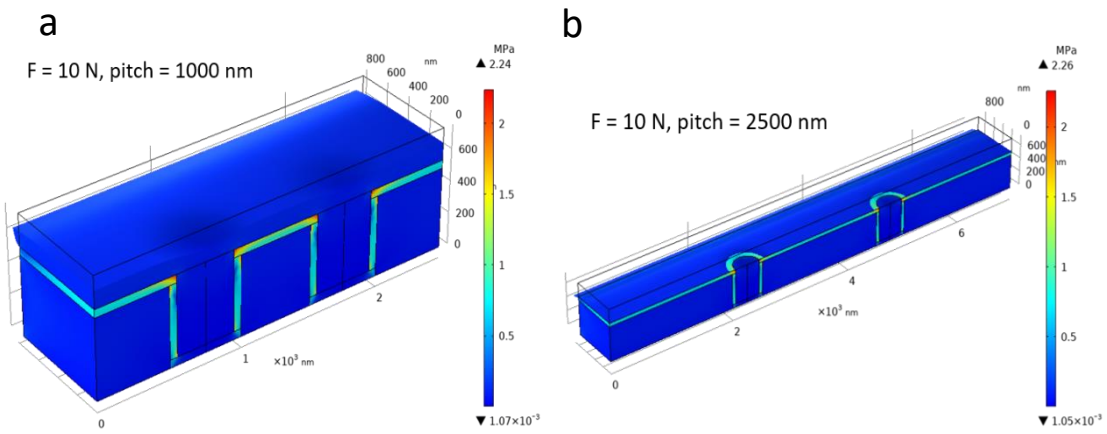


Figure 36. FEM 3D stress distribution map showing the influence of the nanorod pitch a) 1000 nm b) 2500 nm at *F* = 10 N. The maximum stress on the ZnO shell is independent of the pitch

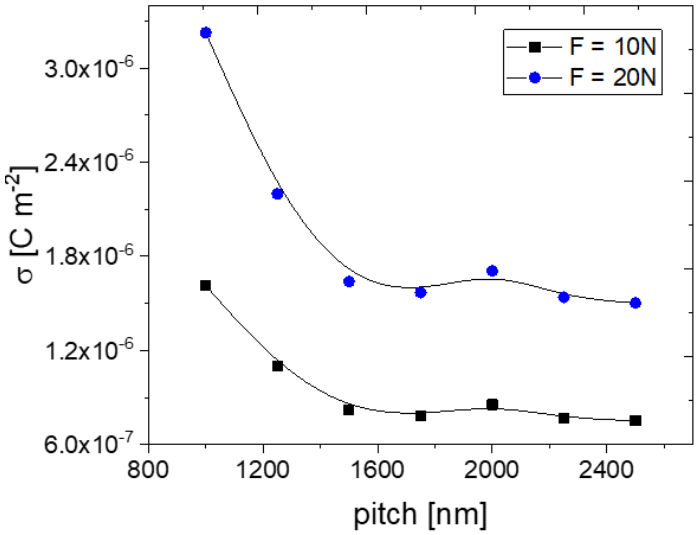


Figure 37. Surface charge density $\sigma$ as a function of the pitch at *F* = 10 and 20 N, data based on FEM model. The surface charge density remains almost constant for a pitch higher than 1500 nm

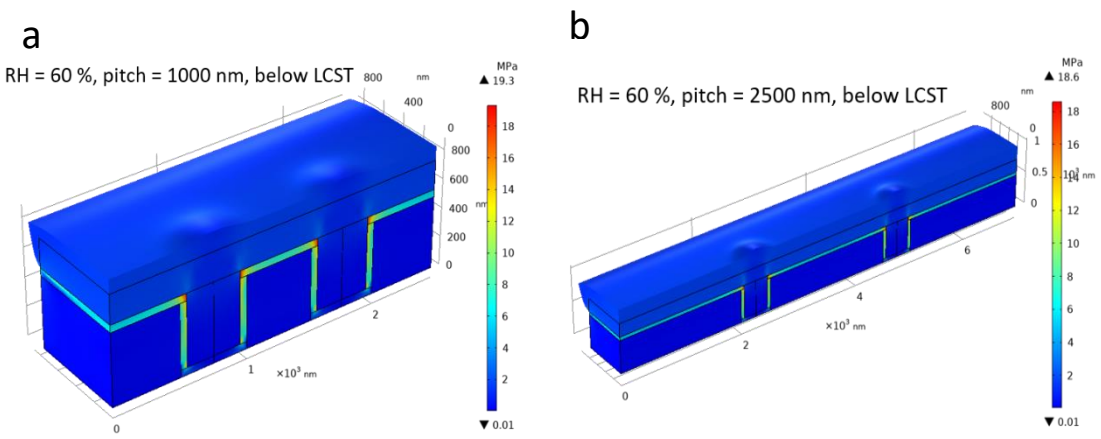


Figure 38. FEM 3D stress distribution map showing the influence of the nanorod pitch a) 1000 nm b) 2500 nm at *RH* = 60% and *T* = 25°C (below LCST). A slight increase in the maximum stress applied on the ZnO shell occurs with higher pitch

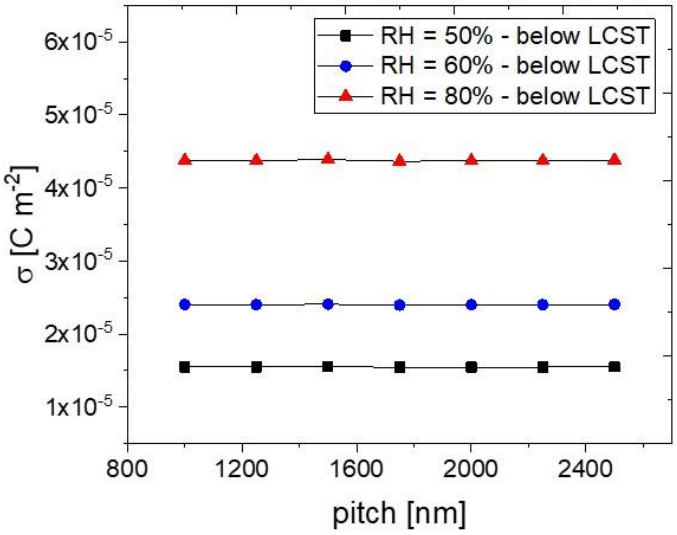


Figure 39. Surface charge density *σ* as a function of pitch at *RH* = 50, 60 and 80%, data based on FEM model. The pitch does not influence the surface charge density

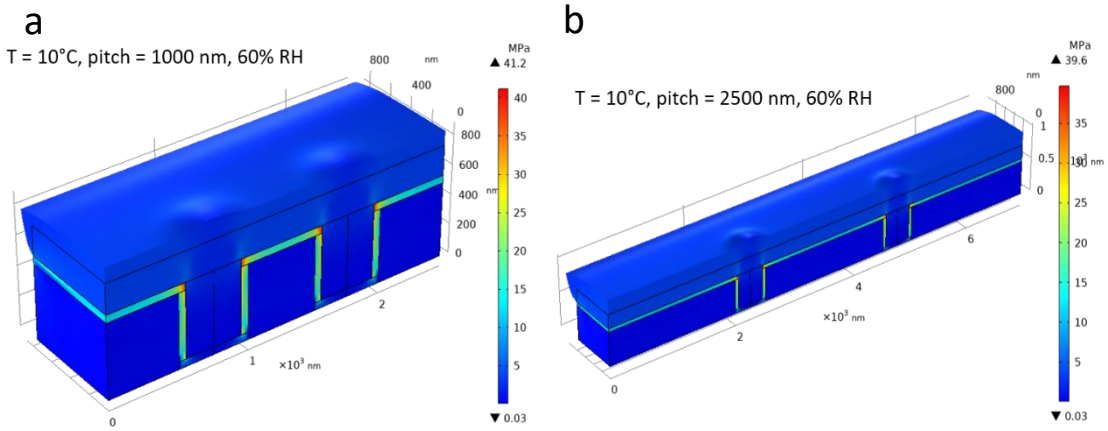


Figure 40. FEM 3D stress distribution map showing the influence of the nanorod pitch a) 1000 nm b) 2500 nm at *T* = 10°C and *RH* = 60%. A slight increase in the maximum stress applied on the ZnO shell occurs with higher pitch

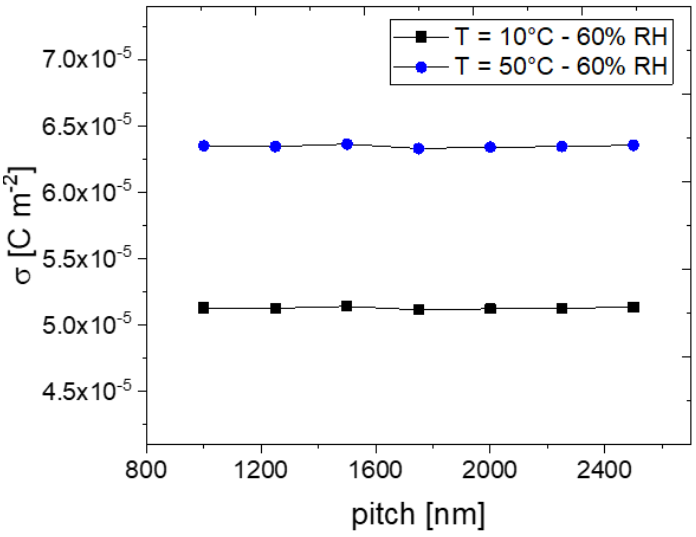


Figure 41. Surface charge density *σ* as a function of pitch at *T* = 10 and 50°C, data based on FEM model. Similar to data shown in Figure 37, the surface charge density is not influenced by the nanorod pitch

## A.2 Influence of aspect ratio

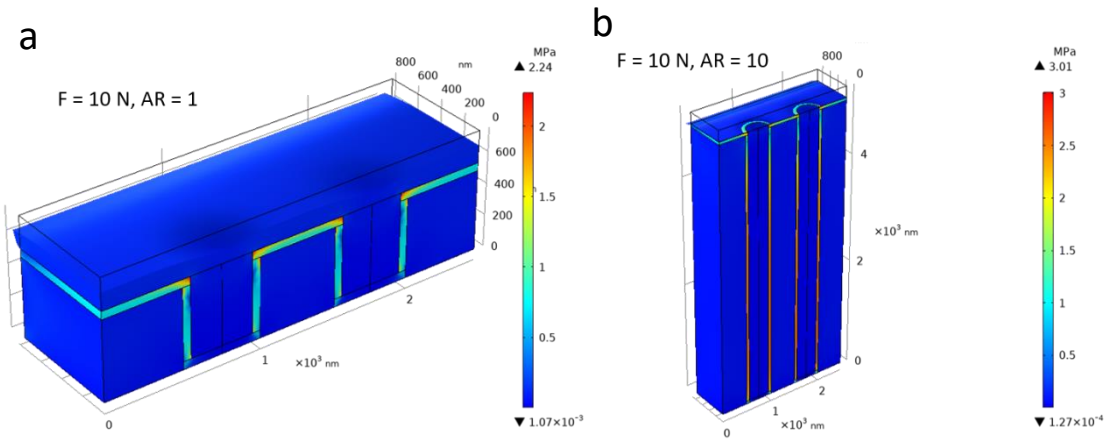


Figure 42. FEM 3D stress distribution map showing the influence of the nanorod aspect ratio (AR) a) 1 b) 10 at *F* = 10 N. The maximum stress increases from 2.24 MPa, for an aspect ratio of 1, to 3 MPa for an aspect ratio of 10

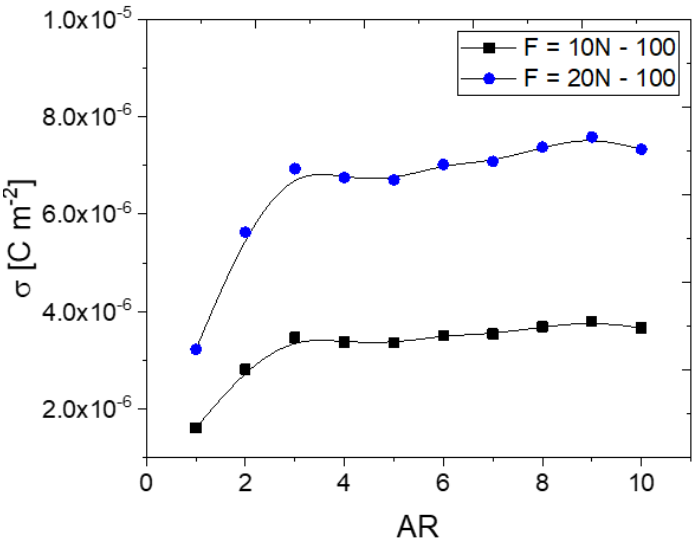


Figure 43. Surface charge density $\sigma$ as a function of AR at *F* = 10 and 20 N, data based on FEM model. An increase in the surface charge density up to an aspect ratio of 3 is observed

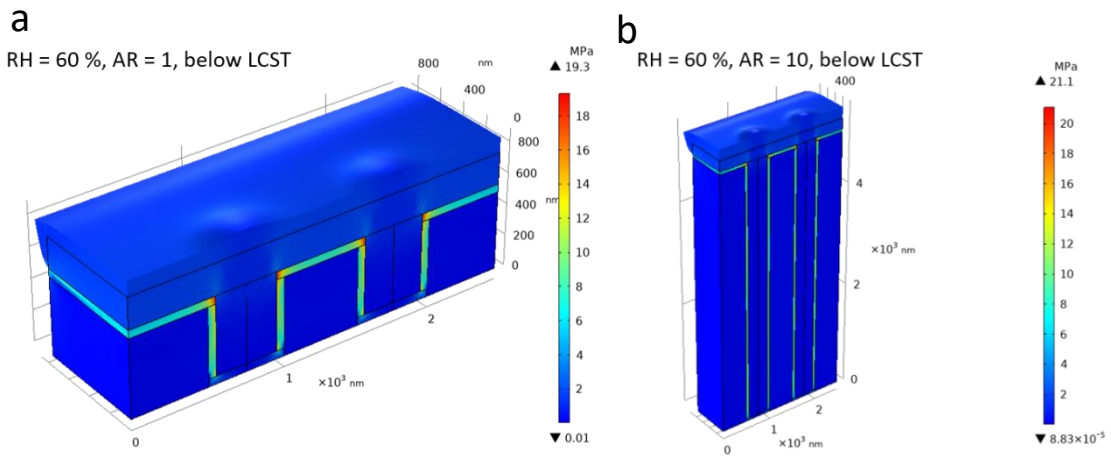


Figure 44. FEM 3D stress distribution map showing the influence of the AR a) 1 b) 10 at *RH* = 60% and *T* = 25°C (below LCST). A slight increase in the maximum stress applied on the ZnO shell occurs with higher aspect ratio

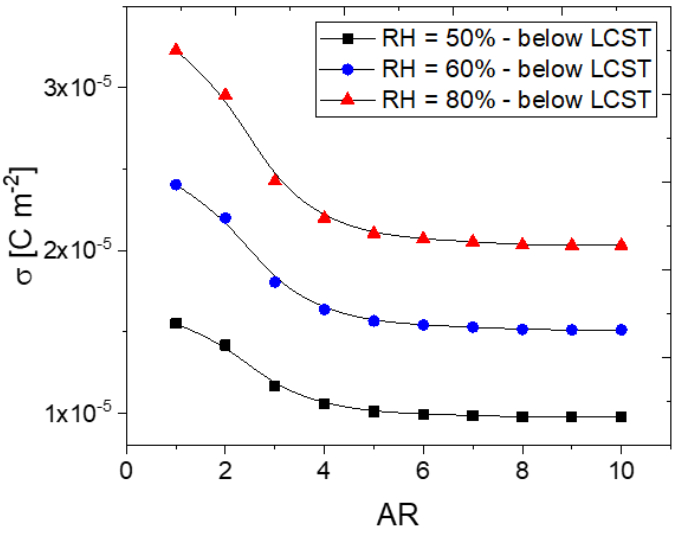


Figure 45. Surface charge density $\sigma$ as a function of AR at *RH* = 50, 60 and 80%, data based on FEM model. A decrease in the surface charge density up to an aspect ratio of 6 is observed

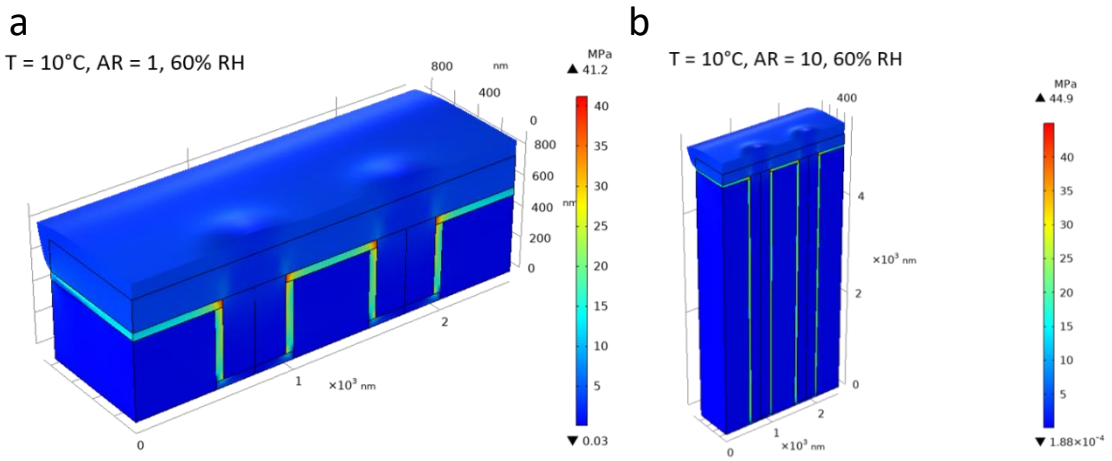


Figure 46. FEM 3D stress distribution map showing the influence of the AR a) 1 b) 10 at *T* = 10°C and *RH* = 60% (below LCST). The maximum stress increases from 41.2 MPa, for an aspect ratio of 1, to 44.9 MPa for an aspect ratio of 10

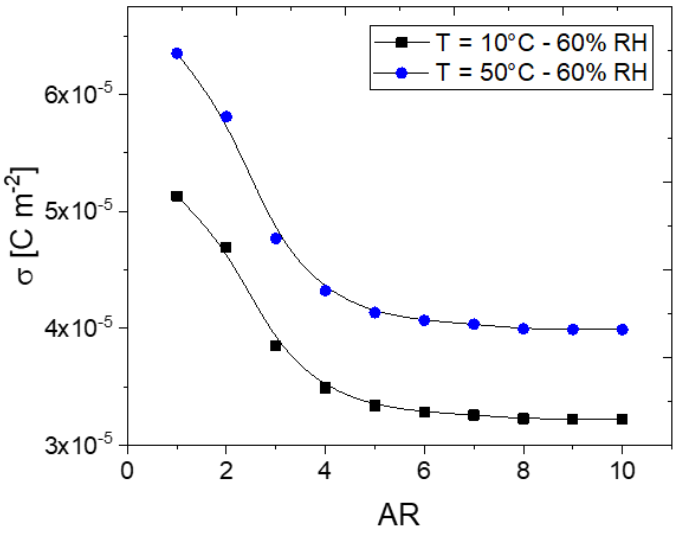


Figure 47. Surface charge density $\sigma$ as a function of AR at *T* = 10 and 50°C, data based on FEM model. A decrease in the surface charge density up to an aspect ratio of 6 is observed

## B. Initial device stability tests

### B.1 Force (soft template, Al-PET substrate)

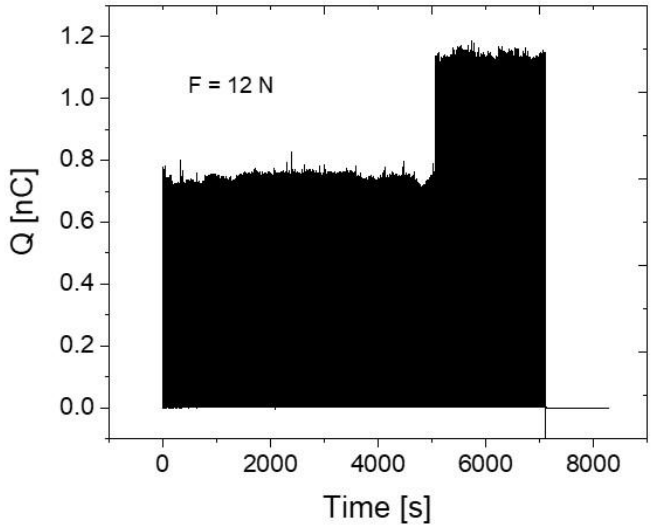


Figure 48. Force stability test performed on a device with a soft polymeric template at *F* = 12 N and *f* = 2 Hz. The device broke down after 7600 s.

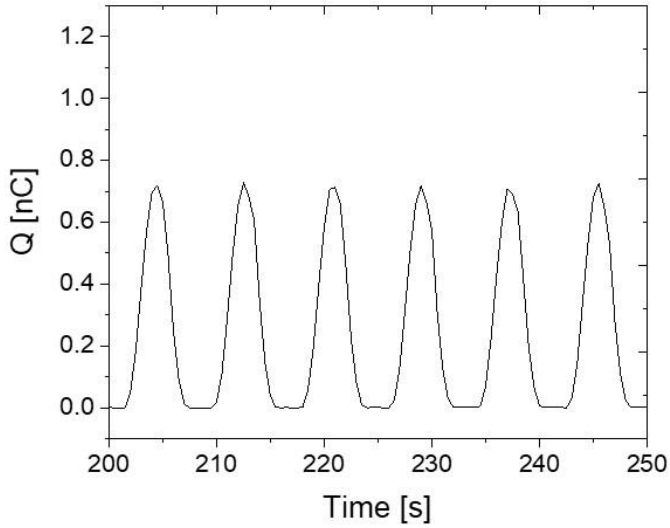


Figure 49. A zoom-in of figure 46 depicting six cycles of response to force, with maximum Q = 700 pC

## B.2 Humidity

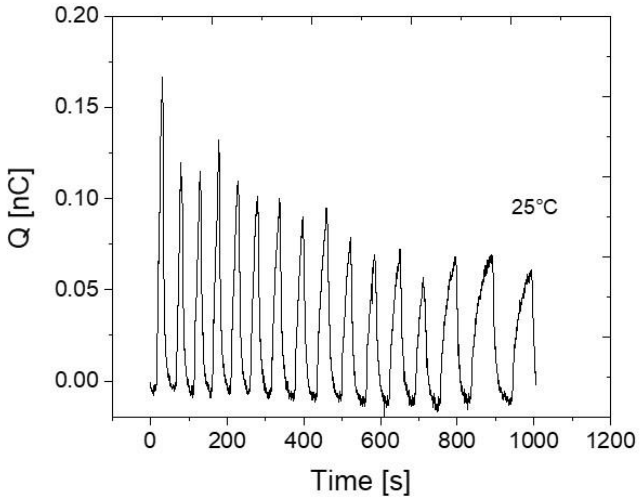


Figure 50. Humidity stability test (15 cycles) performed on a device with a soft polymeric template at *RH* = 5 – 70%. A decrease in the response magnitude is attributed to the corrosion of the top electrode as shown in Figure 49

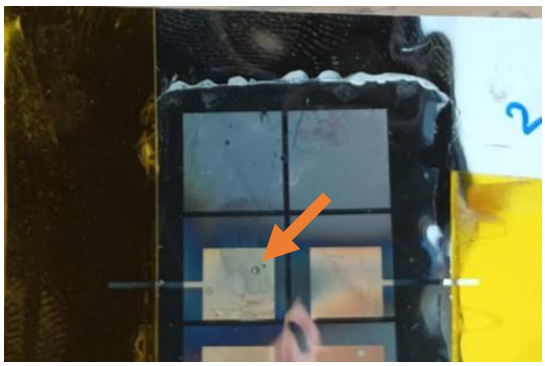

Figure 51. Image of device tested in figure 48, showing electrode corrosion after multiple cycles of humidity exposure

# C. Scientific contributions

## C.1 Publications

1) Abu Ali, T., Groten, J., Clade, J., Collin, D., Schaffner, P., Zirkl, M., Coclite, A. M., Domann, G., & Stadlober, B. (2020). Screen-Printed Ferroelectric P(VDF-TrFE)- co-PbTiO3and P(VDF-TrFE)- co-NaBiTi2O6Nanocomposites for Selective Temperature and Pressure Sensing. *ACS Applied Materials and Interfaces*, *12*(34), 38614–38625. https://doi.org/10.1021/acsami.0c08469

2) Abu Ali, T., Pilz, J., Schäffner, P., Kratzer, M., Teichert, C., Stadlober, B., & Coclite, A. M. (2020). Piezoelectric Properties of Zinc Oxide Thin Films Grown by Plasma-Enhanced Atomic Layer Deposition. *Physica Status Solidi (A) Applications and Materials Science*, *217*(21). https://doi.org/10.1002/pssa.202000319

3) Abu Ali, T., Schäffner, P., Belegratis, M., Schider, G., Stadlober, B., & Coclite, A. M. (2022). Smart Core-Shell Nanostructures for Force, Humidity, and Temperature Multi-Stimuli Responsiveness. *Advanced Materials Technologies*, 2200246. https://doi.org/10.1002/admt.202200246

## C.2 Oral presentations

1) Multi-stimuli responsive nanorods for artificial skin applications. Advanced Materials Day, June 2021, Graz, Austria

2) Multi-stimuli Responsive Nanorod Array. EuroMAT, September 2021, Graz, Austria

3) Multi-stimuli responsive nanorod array. AVS 67 Virtual Symposium, October 2021

4) Modelling Force-, Temperature- and Humidity-Responsive Core-Shell Nanorods. COMSOL Day Austria, February 2022, Vienna, Austria

5) Smart Core-Shell Nanostructures for Force, Humidity and Temperature Sensing. IC-MPPE, May 2022, Leoben, Austria

6) Smart Core-Shell Nanostructures for Force, Humidity and Temperature Sensing. EMRS Virtual Spring Meeting, June 2022

## C.3 Poster presentations

1) FEM simulations of multi-responsive hybrid nanorods. EMRS Spring meeting, May 2019, Nice, France

2) Development of site-specific arrays of pressure, temperature and humidity multi-responsive nanorods. Advanced Materials Day, September 2019, Graz, Austria

3) Multi-stimuli responsive core-shell nanorods for artificial skin applications. EuroEAP virtual, June 2021

D. Journal cover/frontispiece